Multiscale Modelling of Gas Hydrate Mechanical and Thermal Properties

Zeina Mustafa Jendi

Doctor of Philosophy

Department of Chemical Engineering

McGill University

Montreal, Quebec

December 2015

A thesis submitted to McGill University in partial fulfillment of the requirements of the degree of Doctor of Philosophy

© Zeina Mustafa Jendi 2015

Dedication

To my parents…

The ones who have enabled me to make it this far and still aim higher

The ones from whom I derived my confidence to shine brighter

This is just as much yours as it is mine, so to you I dedicate this moment in my lifetime

Contributions of the Author

The author chooses the manuscript-based thesis option following the guidelines stipulated by the Faculty of Graduate and Postdoctoral Studies: https://www.mcgill.ca/gps/thesis/guidelines/preparation

The contents of Chapters 2-5 of the present thesis are adopted from articles published in or to-be submitted to scientific journals under the normal supervision of my research supervisor, Prof. Alejandro D. Rey, and co-supervisor, Prof. Phillip Servio, who are also co-authors. All computations, data analysis, and articles included are the work of the author.

Acknowledgements

"We exalt whoever We please: but above those who have knowledge there is One all knowing." The foremost acknowledgement goes to God, the source of all blessings. His presence at every stage of my PhD was the reason for this accomplishment today. All I can say is *"If you tried to count God's blessings, you would never be able to number them."*

I would like to sincerely thank my supervisors for their support throughout this PhD. Prof. Alejandro D. Rey, my research supervisor, has been a great support with his patience, kindness, great enthusiasm for this work, and innovative ideas. He is definitely a role model in research from which I had the honor to learn first-hand. I would also like to thank my co-supervisor, Prof. Phillip Servio, for his encouraging words and interest in my work. His welcoming and friendly demeanour was invaluable to my PhD experience. Both of my supervisors were kind and patient enough to review my work.

I am also thankful to my sources of funding including: the American Chemical Society Petroleum Research Fund for a new direction grant, the William H. Gauvin Fellowship in Chemical Engineering, the McGill Engineering Doctoral Award, and the Society of Petroleum Engineers for the Star Fellowship. I would also like to acknowledge Calcul Québec for the parallel computing facilities.

I would like to express my gratitude to all my friends who made my time as a graduate student much easier with their company and the smiles we shared. The priceless time I spent with Fatou and Zainab was the best bit of every week. The long hours of laughter with Zeina helped me get through the times of stress, and Serene's serenity was essential especially during our encounters with the French language. The moments I spent with my caring friend Zulikha and her lovely family charged me with tranquillity despite my hectic schedule. Also, my colleagues in my research group were of great support: Pardis with her encouragement and exceptional sense of humor, the Oscars and the friendly atmosphere and interesting conversations they brought in, and Hang who helped me with installing software. Thanks are also due to François for translating the thesis abstract.

A huge thank-you is due to the ones who have prepared me to venture this academic path in the first place. Whether knowingly or not, Prof. Naif Darwish and Prof. Rachid Chebbi have given me invaluable insight on what it takes to become a great, influential professor with their high ethics, exceptional knowledge and wisdom, and caring nature. They were and will always be my primary role models in academia.

Lastly and most importantly, the deepest acknowledgement goes to my family, grandparents, and relatives who made this possible and followed me throughout the process. Words cannot express how grateful I am to be part of such a loving family which supported me on all levels, and I cannot help but thank each one of them: my Mom, Reem, for her endless love and confidence in me; my Dad, Mustafa, for his relentless interest in my work to know exactly what the numbers I am crunching are; my siblings, Abdul Razak, Roua, Abdul Rahman, and Shaza, for their admiration and genuine care. They all did not let me quit when I thought this PhD was an impossible-to-complete endeavor after my first year. Thank you all.

Abstract

This thesis involves multiscale modelling of the mechanical and thermal properties of gas hydrates using atomistic simulations. Elastic and plastic deformation of gas hydrates has been modelled, and key thermophysical properties have been determined. Most of the work has been done using *ab initio* simulations, and classical force fields have been used when necessary. Specifically, density functional theory has been used for the determination of structural and mechanical properties of methane and carbon dioxide hydrates and for the quantification of the ideal strength of methane hydrate and ice at the nanoscale. Molecular dynamics coupled with density functional theory has been used for the calculation of heat capacity, compressibility, and thermal expansion coefficient of methane hydrate over a wide temperature and pressure range at the nanoscale. Finally, plastic deformation of methane hydrate involving linear defects has been modelled as a function of pressure and gas composition using a classical force field at the microscale. The results presented in this work provide valuable insights on the elastic properties of gas hydrates, the structural evolution of perfect gas hydrate crystals during elastic deformation, the variation of some thermophysical properties with temperature and pressure and the range over which ice properties can be extrapolated to gas hydrates, and the core structure and mobility of edge and screw dislocations during plastic deformation of gas hydrates. In terms of computational modelling, appropriate parameters for density functional theory specific to gas hydrates have been determined, the importance of hydrogen bonding and structural stability during deformation is highlighted, the significance of multi-body interactions in gas hydrates is quantified, and a coarse-grained potential has been applied to model plastic deformation. The work presented in this thesis partially fills a gap in the much needed, yet less researched, field of mechanical deformation and thermophysical properties of gas hydrates which is essential for countless applications, including energy recovery, carbon dioxide sequestration, gas transportation, and climate change, among many others.

Résumé

Cette thèse implique la modélisation multi-échelle des propriétés mécaniques et thermiques des hydrates de gaz à l'aide de simulations atomiques. Les déformations élastique et plastique des hydrates de gaz ont été modélisées, et les propriétés thermophysiques importantes ont été déterminées. La plupart des travaux ont été réalisés en utilisant des simulations *ab initio*, et des champs de force classiques ont été utilisés lorsque cela fut nécessaire. Plus précisément, la théorie fonctionnelle de la densité a été utilisée pour la détermination des propriétés mécaniques et structurelles des hydrates de méthane et du dioxyde de carbone ainsi que pour la quantification de la résistance idéale des hydrates de méthane et de la glace à l'échelle nanométrique. La dynamique moléculaire couplée avec la théorie fonctionnelle de la densité a été utilisée pour le calcul de la capacité thermique, la compressibilité et le coefficient de dilatation thermique des hydrates de méthane sur une large plage de température et de pression à l'échelle nanométrique. Enfin, la déformation plastique des hydrates de méthane impliquant des défauts linéaires a été modélisée comme une fonction de la composition du gaz et de la pression en utilisant un champ de force classique à l'échelle microscopique. Les résultats présentés dans ce travail fournissent de précieuses informations sur les propriétés élastiques des hydrates de gaz, l'évolution structurelle de parfaits cristaux d'hydrates de gaz lors de la déformation élastique, la variation de certaines propriétés thermophysiques avec la température et la pression et la plage sur laquelle les propriétés de la glace peuvent être extrapolés pour les hydrates de gaz, ainsi que la structure de base et la mobilité des arrêtes et des dislocations vis au cours de la déformation plastique des hydrates de gaz. En termes de modélisation informatique, les paramètres appropriés pour la théorie fonctionnelle de la densité spécifique aux hydrates de gaz ont été déterminés, l'importance de la liaison hydrogène et la stabilité structurelle pendant la déformation est mise en évidence, l'importance des interactions multi-corps dans les hydrates de gaz est quantifiée, et un grossier grains potentiel a été appliqué pour modéliser la déformation plastique. Le travail présenté dans cette thèse remplit partiellement une lacune dans le, très nécessaire, mais encore peu recherché, domaine de déformation mécanique et des propriétés thermophysiques des hydrates de gaz qui est nécessaire pour de nombreuses applications, y compris la récupération d'énergie, la séquestration du dioxyde de carbone, le transport de gaz et le changement climatique, parmi beaucoup d'autres.

Table of Contents

List of Figures

List of Tables

1 General Introduction

1.1 Thesis Motivation

Gas hydrates have recently been the center of much research due to their emerging applications in different fields ranging from energy resource extraction and gas transport to climate change. Although they can be synthesized, they also exist naturally almost all over the world[1], as Figure 1-1 shows.

Natural gas hydrates, mainly methane hydrates, are considered an alternative energy resource since some conservative assessments suggest that they incorporate an energy content that is twice the energy stored in all other fossil fuel deposits.[2] Several countries, like the United States, Canada, Japan, China, India, and Taiwan, are currently conducting intensive research on developing gas hydrates as an energy resource with Japan planning to start commercial mass production by 2018.[3] One method to produce natural methane hydrate is to replace the stored methane gas with carbon dioxide for sequestration purposes due to the thermodynamic favourability of the process.[4] Some studies were able to achieve an 85% recovery rate of methane using a mixture of carbon dioxide and nitrogen.[5]

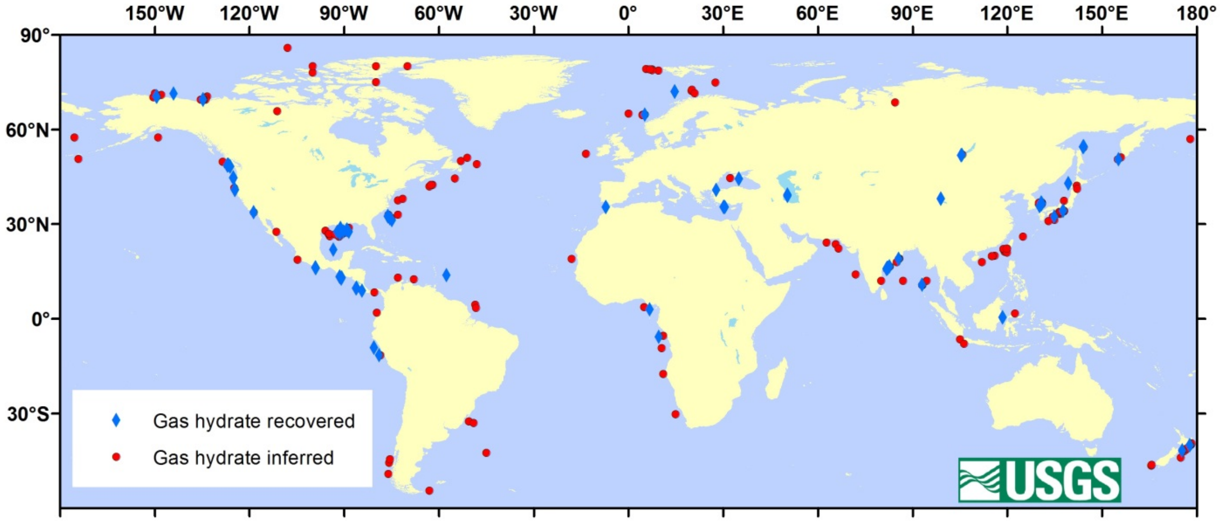

Figure 1-1. Distribution of inferred and recovered gas hydrate deposits around the world. (Map courtesy of US Geological Survey (USGS), updated December 2013)

Additionally, gas hydrates can constitute potential gas storage and transportation media. The gas density of methane in hydrates is comparable to that of compressed methane yet less than that of liquefied natural gas (LNG).[6] However, gas hydrates are still considered potential storage media since they require milder conditions to form and remain stable compared to LNG. It has been demonstrated experimentally[7] that natural gas hydrates can be stored up to -20^{o}C at atmospheric pressure, compared to -160^{o}C at the same pressure for LNG storage and transportation.

Finally, gas hydrates have critical implications when it comes to flow assurance in pipelines and climate change factors. In oil and gas flowlines, water is always produced with hydrocarbons, and if conditions are suitable hydrates can form and create plugs. This is such a serious issue that US $220 million is spent annually worldwide on methanol for hydrate inhibition purposes.[6] As for climate change, there seems to be much dispute on the effect of hydrates in this regard. However, it is well documented that the disruption of gas hydrates can lead to dangerous landslides that can affect sub-sea structures and release entrapped gas. Sloan[6] cites such a case that happened 15,000 years ago off the Carolina Coast and raised the methane content of the atmosphere by 4%.

In most of the above-mentioned applications, the mechanical and thermal properties of gas hydrates are very important. Firstly, the speed of sound waves is often employed in the detection of gas hydrate strata in the earth.[8] This speed depends on the elastic moduli and density of gas hydrates, among other factors. Acoustics are also used for the detection of plugs in flowlines. Secondly, when considering hydrates for carbon dioxide sequestration, it is important for risk assessment to know how this change in composition changes the mechanical parameters, in terms of strength and elasticity, of the earth strata that host these gas hydrates. Furthermore, the possibility of failure of the earth strata that contain gas hydrates upon the decomposition of hydrates is related to their strength; higher strength is associated with higher energy release.[9] As for thermal properties, these are equally important. The heat capacity comes into play when modelling controlled natural gas production from hydrate-bearing sediments[10], and the thermal expansion coefficient is an important parameter in risk assessment studies of the mechanical stability of earth strata hosting gas hydrates[11]. On a larger scale, thermal properties are needed in studies of climate change related to methane release from natural hydrates.[10]

After establishing the motivation of this work, the rest of this introductory chapter is organized as follows. Section 1.2 gives some background information on the structure and properties of gas hydrates; section 1.3 highlights the need for computational modelling of gas hydrates, section 1.4 explains the scope of this work; section 1.5 provides some theoretical and computational background on the adopted modelling approaches; section 1.6 describes the validation of the computational methodology that has been done in this work; section 1.7 summarizes the thesis organization.

1.2 Background

1.2.1 Gas Hydrate Crystal Structure

Gas hydrates or clathrates are crystalline solids with a basic structure of water cages that encapsulate compressed gas molecules. These cages are not all necessarily occupied by gas, which makes these solids non-stoichiometric. The gas molecules that form clathrates are relatively small ones, less than 0.9 nm, like methane, carbon dioxide, or butane.[6,11] Gas hydrates can form different structures, of which three are the most prominent and common: sI, sII, and sH. Both sI and sII have cubic structures, while sH is hexagonal. In terms of occurrence and guest size, sI prevails in nature and hosts small guests in the range of 0.4 to 0.55 nm; sII prevails in artificial environments with guests ranging from 0.6 to 0.7 nm; and sH can occur in both types of environments, but it should incorporate both small and large, 0.8-0.9 nm, guests.[6]

The common cage in all structures is the 5^{12}, called pentagonal dodecahedra since it consists of 12 pentagonal faces of water molecules. The guest molecules have restricted translational motion within the cavity compared to their much greater rotational and vibrational motion.[6,12] In addition to the 5^{12} cage, the structure includes other types of cavities that fill the space in between the 5^{12}s; otherwise, the hydrogen bonds will be strained and some will be broken.[6] These other types can host larger guests and have hexagonal faces, namely the $5^{12}6^{2}$ with 12 pentagonal and 2 hexagonal faces and the $5^{12}6^{4}$ with 12 pentagonal and 4 hexagonal faces. Each crystal lattice of gas hydrates has a specific ratio of cages which is, for example, $2 \cdot 5^{12} + 6 \cdot 5^{12}6^{2}$ for sI. The specific lattice parameters and details for each structure are summarized in Table 1-1 at average, typical conditions. A visualization of the sI structure is shown in Figure 1-2.

For all three crystal structures, a minimum water composition of 85 mol% results if all cages are occupied with single guests. Usually, just one guest molecule occupies each cage, but at very high pressures and with small guest molecules, like hydrogen, a cage can be occupied by more than one molecule at a time.[14]

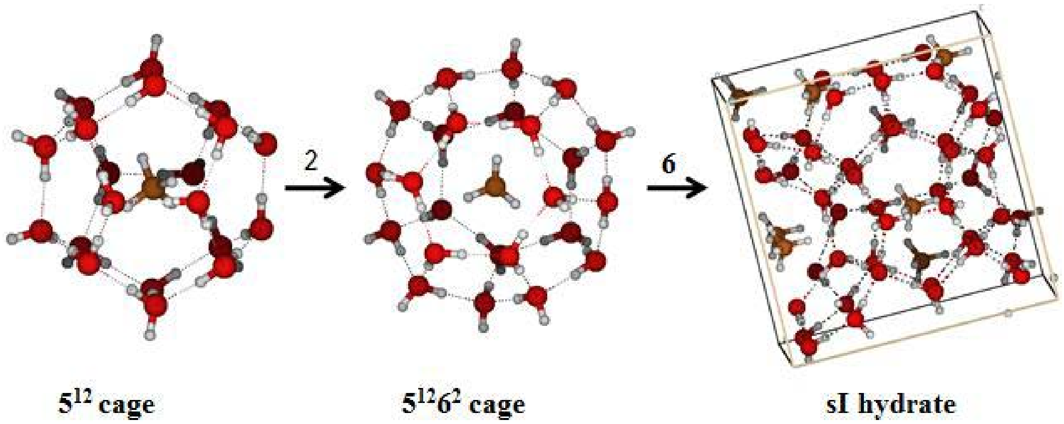

Figure 1-2. Cages and single lattice unit in sI methane hydrate. (Visualization done using Molden[13], where red, grey, and yellow spheres represent oxygen, hydrogen, and carbon atoms, respectively)

Table 1-1. Structural properties of sI, sII, and sH hydrates.[7]

	Crystal Structures						
	sI		**sII**		**sH**		
Cavity	5^{12}	$5^{12}6^{2}$	5^{12}	$5^{12}6^{4}$	5^{12}	$4^{3}5^{6}6^{3}$	$5^{12}6^{4}$
Cavities per unit cell	2	6	16	8	3	2	1
Average cavity radius (nm)	0.395	0.433	0.391	0.473	0.394	0.404	0.579
Water molecules per cavity	20	24	20	28	20	20	36
Crystal system	Cubic		Cubic		Hexagonal		
Lattice parameters	a=1.2 nm $\alpha=\beta=\gamma=90^{o}$		a=1.73 nm $\alpha=\beta=\gamma=90^{o}$		a=1.21 nm, c=1.01 nm $\alpha=\beta=90^{o}$, $\gamma=120^{o}$		
Guest molecule examples	Methane, ethane, carbon dioxide		Propane, iso-butane		Methane + neohexane		

1.2.2 Gas Hydrate and Ice I_h

Since gas hydrates are solids composed mostly of water, it is reasonable to compare them with solid water or ice. The most common ice structure, called I_h, consists of non-planar, hexagonal rings in which each water molecule is hydrogen-bonded to four others in a tetrahedral arrangement shown in Figure 1-3.[15] In terms of bonding, the hydrogen bond length is 1% longer in hydrates, and the oxygen bond angles are 3.5° larger for hydrates.[11] The differences in bonding are not considerable between hydrates and ice I_h; however, gas hydrates are much more capable of filling space with cages of nearly isotropic interaction.[16] To better compare the differences, it is suitable to consider their physical properties. Table 1-2 includes the most important physical properties of ice, sI, and sII (most at 260 K and 30 MPa). For most properties in the table, all three structures have values close to each other. However, for thermal conductivity the values for hydrates are much lower than those of ice. This peculiar behavior is not yet fully understood, but it may be attributed to the vibrational coupling of the guest gas and host water molecules in gas hydrates.[17]

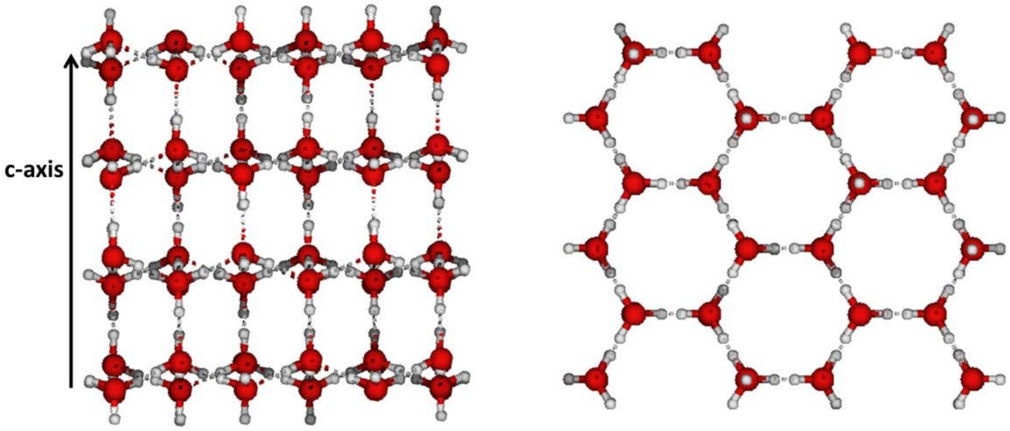

Figure 1-3. Atomic structure of ice I_h. Left: Stacking of non-planar rings, Right: Cross-section along the c-axis. (Visualization done using Molden[13], where red and grey spheres represent oxygen and hydrogen atoms, respectively)

Therefore, in terms of mechanical and many thermal properties, ice may appear to be a suitable model for gas hydrates due to the similarity in many properties and bond structure. However, a more careful review of their properties reveals some important differences.

In terms of mechanical properties, recent studies have found key differences in terms of elastic isotropy, structure, and strength. For elastic properties, the single lattice units of methane hydrate are believed to be elastically isotropic as opposed to ice and most other cubic solids. This isotropy could be due to the void-rich network and departure from the ideal tetrahedral arrangement of water molecules.[18] Apart from this, gas hydrates undergo structural changes, at pressures greater than 1 GPa, to some ice phases[19,20]; this reflects the disparity between the different structures that necessitates such transitions. Moreover, a key difference lies in the mechanical strength. Experimental studies have revealed that methane hydrate can be more than 20 times stronger than ice as shown in Figure 1-4.[9,21,22] One explanation for this peculiar behaviour is the fact that the water diffusion time is much greater (almost two orders of magnitude) in hydrates compared to ice[23]; thus, the flow rate of defects, which govern deformation, is much lower in hydrates. The difference can also be related to the unit lattice dimensions. A unit lattice of sI hydrate has a linear dimension almost twice that of ice I_h. This can hinder deformation by making diffusion of water molecules and certain motions of dislocations more difficult. The discrepancy in strength increases as temperature decreases below the ice melting point, and the compressive strength of gas hydrates is close to that of ice only at conditions near the hydrate stability boundary.[11] This significant difference in strength can have important implications for strata containing hydrates. The loss of mechanical strength as hydrates partly decompose amplifies the movement of hydrate-bearing sediments.[9]

Table 1-2. Physical properties of ice, sI, and sII structures.[7,11]

		Structure	
	Ice (I_h)	**sI**	**sII**
Compressional wave speed ($m \cdot s^{-1}$)	3870.1	3778	3821.8
Shear wave speed ($m \cdot s^{-1}$)	1949.3	1963.6	2001.14
Poisson ratio	0.3301	0.317	0.3119
Shear modulus (GPa)	3.483	3.541	3.6764
Bulk modulus (GPa)	9.097	8.762	8.482
Density ($g \cdot cm^{-3}$)	0.917	0.91	0.94
Heat capacity ($J \cdot kg^{-1} \cdot K^{-1}$)	1700	2080	2130
Thermal conductivity ($W \cdot m^{-1} \cdot K^{-1}$)	2.23	0.49	0.51
Linear thermal expansion at 200 K (K^{-1})	56×10^{-6}	77×10^{-6}	52×10^{-6}

Furthermore, the atomistic mechanism of plastic deformation varies significantly between hydrates and ice. Ice I_h is known to have high plastic anisotropy owing to its dominant basal slip mechanism of deformation.[24,25] The stacks of planes in ice have hexagonal symmetry and lie perpendicular to the crystallographic c-axis. Thus, plastic deformation involves the slip of these planes over each other through dislocations in what is referred to as basal slip.[15] The significant anisotropy is reflected upon the application of stress in certain directions.[24] With no resolved shear stress on the basal plane, like when the c-axis is parallel to the applied stress, the deformation is extremely small. A slight deviation in alignment induces basal slip. Since gas hydrates do not form as stacks of planes, it is important to identify their main slip mechanism.

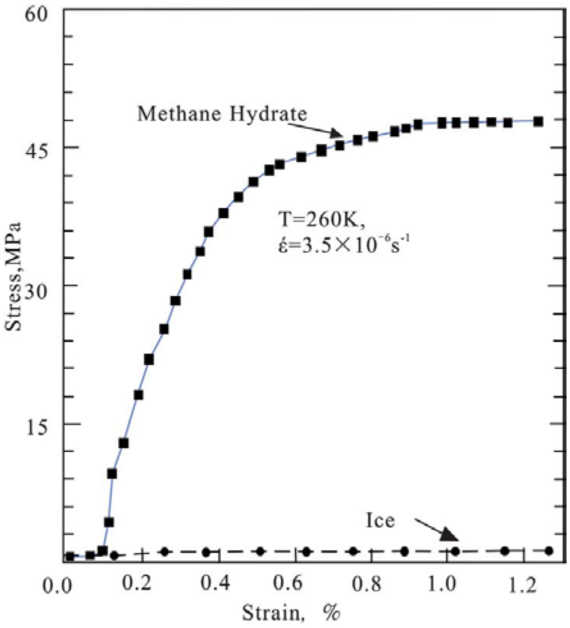

Figure 1-4. Stress vs. strain curves for methane hydrate and ice (at 260 K, confining pressure of 100 MPa, and strain rate of 3.5×10^{-6} s^{-1}).[21]

Finally, although Table 1-2 shows that the heat conductivity displays the greatest difference between hydrate and ice in terms of thermal properties, the heat capacity and thermal expansion coefficient also show significant differences. Both are higher in hydrate compared to ice. The higher heat capacity in hydrate has been attributed to the added vibrational and restricted translational modes of motion of the guest molecules in cages and the distortion of hydrogen bonds from linearity and perfect tetrahedral arrangement.[26] As for the thermal expansion coefficient, its higher value in gas hydrates has been related to anharmonic effects of the dominant guest-host interactions in hydrate crystals[27-30], which may not be highly dependent on the type of guest molecule over a relatively wide range[31], and structural variations[32]. To sum up, while gas hydrates and ice have many similar structural and physical properties, there are many key differences that are still under investigation.

1.3 Need for Computational Modelling

Although considerable research has been published in the past few years on the topic of gas hydrates, the literature is yet lacking in terms of essential computational modelling of their thermal and mechanical properties. In general, data for the elastic properties of gas hydrates are inconsistent and scarce. For example, the percentage difference in the adiabatic modulus between two experimental results[33,34], at the same temperature and pressure, could be 15%. Also, most experimental studies consider narrow ranges of conditions, probably due to the complexity of the set-up, and fail to accurately characterize the composition of the hydrates they form, due to technical difficulties and hydrate stability issues.[11,35] While experimental results are usually reported for pure gas hydrates, it is very challenging to synthesize pure gas hydrate samples with no residual water or gas and zero porosity, and no study has yet eliminated the significant effect of micropores. Additionally, even if the initial produced sample achieved high purity, ice may be produced later in the system during the experiment upon partial hydrate decomposition. In fact, sample impurity has been the reason why it was initially believed that the strength of gas hydrates and ice is almost the same, which later was proven untrue and that hydrates can be more than 20 times stronger.[11] Therefore, computational modelling of gas hydrates becomes essential to circumvent the shortcomings of experimental work, which is often costly, time-consuming, and subject to inaccuracies due to poor sample characterization.

While there are some computational studies on the mechanical and thermal properties of gas hydrates, they are few and there is still a need for the work presented here. There are very few studies that use *ab initio* simulations which use first-principles with no experimentally-fitted parameters. Specifically, there are only two *ab initio* studies[36,37] of the full elastic constant tensor of methane hydrate. Also, there are no computational studies, at any level, that quantify the strength of pure gas hydrates and relate that to the evolution of the atomic structure to better understand the exact deformation mechanism. This is also true for microscale plastic deformation in which there are only experimental studies that quantify the strength and lump the effects of different defects into a single dislocation flow model[9,21]. Apart from this, no studies have been done to determine the dominant slip mechanism in gas hydrates. Thus, there is a need for simulations that rely on first-principles, given the shortcomings of experiments, decipher the exact deformation mechanism on different scales, and model the effect of individual defects.

Lastly, a more accurate characterization of the properties of gas hydrates fills in the gap where ice properties are usually extrapolated to gas hydrates. Due to similarities in structure and composition, ice properties are usually used for gas hydrates when better data is not available. However, as explained in Section 1.2.2, there are some significant differences between gas hydrates and ice, and there is no accurate quantification of the range in which properties of both materials are interchangeable. In fact, some properties, such as thermal expansion coefficient, are significantly different even between ice and empty hydrate structures, with no guest molecules.[27,32]

Chapters 2-5 further emphasize the need, with greater detail, for the work presented in each of the chapters.

1.4 Scope of Work

With a topic as broad as gas hydrates, specifying the scope of work is essential. This thesis focuses on the multiscale modelling of key mechanical and thermal properties of bulk methane hydrates that can exist naturally or be synthesized. A wide range of temperatures, pressures, and compositions is considered, and some properties of other systems, namely carbon dioxide hydrate and ice I_h, are modelled for comparison. The four main objectives that are explained in the next chapters are: the calculation of elastic moduli and constants using *ab initio* methods at the nanoscale, the quantification of strength and strength-related properties at the nano- and micro-scales using *ab initio* and classical methods, the determination of key thermal properties using *ab initio* methods at the nanoscale, and clarification of the core structure and motion of linear defects at the microscale using classical methods. This scope covers multiscale elastic and plastic deformation of gas hydrates. A schematic of the multiscale modelling done in this thesis is shown in Figure 1-5.

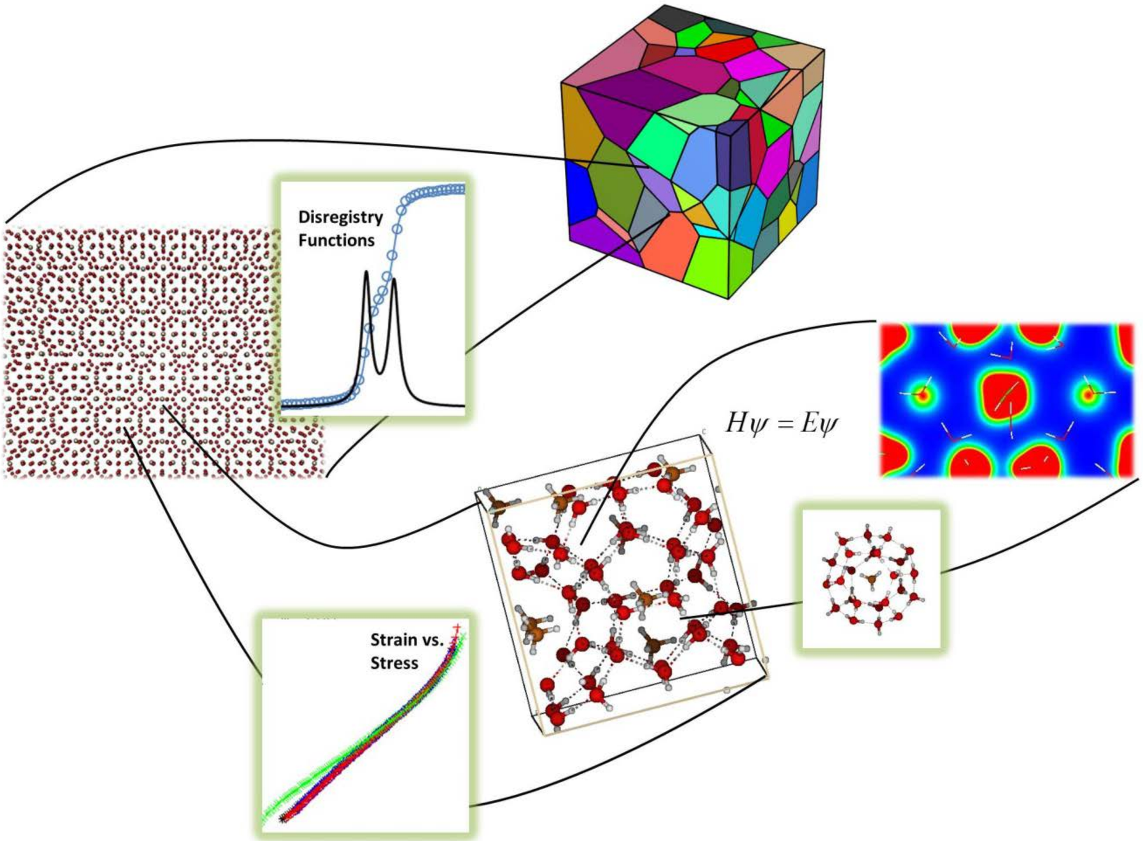

Figure 1-5. Multiscale modelling done in this thesis. Plastic deformation of single crystals, of the polycrystalline material, with defects is modeled at the microscale; elastic deformation of single lattices, of single crystals, is modeled at the nanoscale; atomic interactions, of single lattices, are modeled at the electron scale using *ab initio* methods.

1.5 Theoretical and Computational Background on Modelling

With the general background information for gas hydrates, the need for computational modelling, and scope of this work described in the previous sections, it is helpful to briefly describe the theoretical and computational background of the modelling approaches adopted in this work.

1.5.1 Theoretical Background

For the theoretical background, a brief description of elastic and plastic modelling along with the relevant equations is provided. For thermal properties, standard thermodynamic equations have been used for this, so they are not explained in this chapter but only summarized in the relevant chapter, Chapter 4.

Elastic Deformation

In simple terms, elasticity is the tendency of a material to retain its original shape following the application of a stress. This retaining of shape is possible as long as the stress is below the material's elastic limit. For small stresses in three-dimensional applications, the stress, σ, and strain (or deformation), ε, follow Hooke's Law:[38]

$$\sigma_{ij} = \sum_{k=1}^{3}\sum_{l=1}^{3} C_{ijkl}\varepsilon_{kl} \tag{1.1}$$

where the proportionality constant C_{ijkl} is defined as the elastic stiffness constant, and σ_{ij} is the force per unit area exerted in the positive i direction on the face that is normal to the j direction. For practical reasons, Voigt matrix notation $\left(\sigma_{ij} = \sum_{j=1}^{6} C_{ij}\varepsilon_{j}\right)$ is usually used instead of the above tensor notation. Many lattices possess some symmetry in their structures. This symmetry reduces the number of independent second-order components of the elastic stiffness constant, C. The C matrix has two, three, and five independent components for isotropic, cubic (like sI and sII hydrates), and hexagonal (like sH hydrates) lattices, respectively.

In order to calculate the elastic constant matrix, a stress-strain analysis, according to eqn (1.1), or an energy-strain analysis, as described next, can be used. Considering a crystal under an initial isotropic pressure, P, with a density, ρ_1, a small homogeneous deformation transforms the primitive lattice vectors a to $a' = a\left(I + \varepsilon\right)$ with I being the identity matrix and ε the applied strain tensor. The internal energy per unit mass, E, of the lattice can be expanded in terms of the Lagrangian strain tensor $\left(\eta_{ij} = \varepsilon_{ij} + \frac{1}{2}\sum_{k}\varepsilon_{ik}\varepsilon_{kj}\right)$ as follows:[39]

$$E\left(\rho_1, \{\eta_{mn}\}\right) = E\left(\rho_1\right) + \frac{1}{\rho_1}\left(\sum_{ij} T_{ij}\eta_{ij} + \frac{1}{2}\sum_{ijkl} C_{ijkl}\eta_{ij}\eta_{kl} + \dots\right) \tag{1.2}$$

where T_{ij} is a component of the stress tensor before any deformation and C_{ijkl} is a component of the elastic constant tensor at the initial pressure. For an initially isotropic pressure $\left(T_{ij} = -P\delta_{ij}\right)$ and expansion of the strain as $\varepsilon_{ij} = s_{ij}\gamma + e_{ij}\gamma^2 + \ldots$, the following relation can be easily derived from eqn (1.2):

$$\sum_{ijkl} C_{ijkl} s_{ij} s_{kl} = 2P \sum_{ik} \left(e_{ik}\delta_{ik} + \frac{s_{ik}^2}{2} \right) + \rho_1 \left. \frac{\partial^2 E(\rho_1, \gamma)}{\partial \gamma^2} \right|_{\gamma=0} \tag{1.3}$$

Therefore, a set of independent strains can be applied to the system, and the curvature of the energy-strain curve can be used to determine the elastic constants based on eqn (1.3).

The elastic stability of crystals can be assessed using different measures, the most common of which is Born stability criteria[40]. The basis of the Born theory is that the stability of a crystal upon melting can be characterized by the difference in shear properties between the solid and liquid phases. While solids resist shear, liquids have no shear resistance; therefore, mechanical stability with respect to shear deformation can be used for this purpose. While in Born's original paper the stability relations do not apply for an initially stressed solid, or a solid under pressure, the criteria presented below extend Born's analysis for a solid under an initially isotropic pressure as derived in Ref. 39. For a cubic crystal, the relevant relations are:

$$C_{44} - P > 0, \quad C_{11} - P > \left| C_{12} + P \right|, \quad C_{11} + 2C_{12} + P > 0 \tag{1.4}$$

The violation of the above inequalities reflects certain phase transitions. Since liquids have no shear resistance, melting is characterized by the first criterion. In some cases, it is possible that one of the other stability criteria is violated first. If the second inequality is violated first, Born describes it as a transition to a gel phase in which shear resistance persists, but the stress is hydrostatic, similar to that in a liquid. Finally, if the last criterion is satisfied first, Born describes the transition as sublimation since the crystal becomes completely unstable and loses its cohesion.

Based on this theory of elastic deformation, several properties can be calculated in this regime. These include elastic constants, elastic moduli, compressional and shear wave speeds, and ideal strength, among many others. These properties are further explained in Chapters 2 and 3.

Plastic Deformation

The plastic regime is characterized by a large, permanent deformation of a material. This is typically studied experimentally using tensile/compressive tests. In a single crystal, plastic deformation involves the sliding of planes of atoms; however, the final structure is still the same crystal structure since the atoms end up in equilibrium crystalline positions, but the deformation is irreversible.[41,42] These planes are commonly referred to as slip planes and are densely packed which allows them to slide at lower shear stresses. The direction in which the plane slides is usually the one that involves the least resistance and is called a slip direction.

A critical parameter in plastic deformation of single crystals is the behavior of dislocations.[42] Without dislocations, the theoretical shear strength is in the order of $G/3 - G/30$, where G is the crystal's shear modulus. Dislocations can lower the shear strength by up to five orders of magnitude. They can be of edge, screw, or mixed type, but for ease of visualization only edge dislocations are considered in this description. An edge dislocation involves an extra half plane of atoms inserted between two planes. The process by which such a dislocation assists plastic deformation is clarified in Figure 1-6. The dislocation plane originally consists of the atoms in the same vertical plane as atom A. Due to shear stress, τ, atom A moves slightly to the right, and atom 2 moves slightly to the left by which the dislocation moves. Screw dislocations, on the other hand, involve partial shearing of a perfect crystal. Dislocations greatly help plastic deformation by allowing the slip to happen one atom at a time instead of rigidly moving all atoms on one side of the slip plane. A convenient method to characterize a dislocation is using a Burgers vector that defines the magnitude and direction of slip. The Burgers vector is perpendicular to the dislocation line for edge dislocations and parallel for screw dislocations.

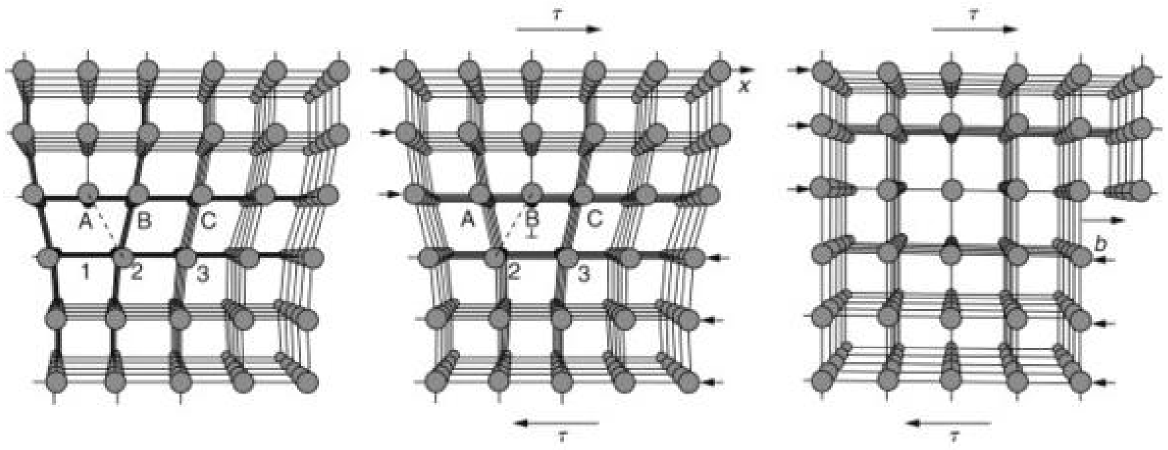

Figure 1-6. Edge dislocation movement during plastic deformation.[41]

The lattice distortions due to dislocations have been described by several theories, and one of the most commonly cited models is that of Peierls[43] and Nabarro[44], despite its significant limitations. The Peierls-Nabarro model treats the displacement of atoms above and below the slip plane using continuum theory but treats displacements across the slip plane, with their associated discontinuity, atomistically with a periodicity equal to that of the lattice.[42,45-47] The original model balances stresses across the slip plane in one dimension. Using a sinusoidal function for the shear stress across the slip plane, the displacement solution, $u(x)$, is

$$u(x)=\frac{b}{\pi}\tan^{-1}\frac{x}{w}+\frac{b}{2} \tag{1.5}$$

where b is the magnitude of the Burgers vector and w is a measure of the dislocation width defined in terms of the interplanar distance, h, and Poisson ratio, ν, as $h/\left[2(1-\nu)\right]$ and $h/2$ for edge and screw dislocations, respectively. This definition of dislocation width is set by the requirement of minimizing the total energy and is the resultant of the competitive influences of the elastic energy in spreading the displacement and the atomic interactions in narrowing it. While analytically simple, the Peierls-Nabarro model has serious limitations such that the real displacement solution is expected to deviate from that proposed above for many materials. Specifically, the model applies only to pure edge or screw dislocations while real materials usually have dislocations with both components. Also, the Peierls model involves unrealistic smoothing out of the lattice discreteness near the dislocation core which has severe effects especially for narrow dislocations. Additionally, it implicitly assumes that the displacement profile undergoes a rigid shift when the dislocation moves which is untrue since the displacement profile usually changes in this process. Despite these shortcomings, the behavior of real dislocations is commonly compared to that predicted by the Peierls-Nabarro model to assess the suitability of one of the earliest dislocation models, and any deviations reflect the violation of its assumptions for a specific material. Nevertheless, there have been several attempts to improve this model in various ways like introducing phenomenological force laws instead of the sinusoidal shear stress one, correcting for two-dimensional displacements, and introducing nonlinear corrections for the core region, among others.

1.5.2 Computational Background

For the computational background, the two main computational approaches used in this work are described: density functional theory and *ab initio* molecular dynamics. These approaches have been used in the work presented in Chapters 2-4. Classical force fields for atomic interactions have been used for the work in Chapter 5 and do not require a lengthy discussion here, but the specific force field that was adopted is described in detail in Chapter 5.

Density Functional Theory

Essentially, all macroscopic properties can be rooted back to the molecular structure and potential interactions between molecules. This is well characterized using density functional theory (DFT). For a system of atoms, a central aspect is the atomic interaction and its associated total system energy. This is basically what can be obtained from DFT through quantum mechanics applied to the interactions of individual electrons. One of the key assumptions in atomic structure analysis using quantum mechanics is the Born-Oppenheimer approximation.[48] This approximation involves separating the atomic nuclei and electrons into separate mathematical problems based on the fact that nuclei are much heavier than electrons; thus, electrons respond much faster to external effects than nuclei. This greatly simplifies the solution to quantum equations.

While in classical mechanics Newton's second law describes motion, Schrödinger's equation, formulated in 1925, is its equivalent in quantum mechanics. This is the central equation to any DFT calculation:

$$H\psi = E\psi \qquad (1.6)$$

where H is the Hamiltonian operator for all forms of energy, ψ is the wave function or the sought set of eigenstate solutions of the Hamiltonian that defines the quantum state of the system components, and E the system energy is the set of eigenvalues corresponding to the eigenstates. In the above form, Schrödinger's equation is almost of no practical use for computational work due to its complexity. It is a 3N-dimensional equation, where N is the number of electrons in the system. Apart from this, the wave function is not the entity that can be directly measured in experiments. In fact, what is more physically significant is the density of electrons at a certain spatial location.[48]

The breakthrough in DFT came with Kohn and Sham equations in the 1960s which allowed for an efficient and physically meaningful approach to solving Schrödinger's equation.[48] The equations are based on two fundamental theorems by Kohn and Hohenberg. The first theorem states that Schrödinger's ground-state energy can be determined from a functional of the electron density only, which lends DFT its name. The advantage of considering the density functional lies beyond its physical significance mentioned above. While the complete wave function is 3N-dimensional, the density functional is only three-dimensional while capturing the physical significance of the wave function. The second Kohn-Hohenberg theorem states that the true electron density is the one that minimizes the total energy of the functional.

Mathematically, each Kohn and Sham (K-S) equation is three-dimensional and corresponds to a single electron:[49]

$$\left[-\frac{\hbar^2}{2m}\nabla^2 + U_{ext} + U_H + U_{XC}\right]\phi_i(\boldsymbol{r}) = \varepsilon_i \phi_i(\boldsymbol{r}) \tag{1.7}$$

where $\phi_i(\boldsymbol{r})$ is K-S's one-electron wave orbital or function and is the eigenstate, ε_i is the corresponding eigenvalue, $\hbar$ is the reduced Planck's constant, and m is the electron mass. Thus, a set of three-dimensional equations are solved simultaneously. The terms in brackets account for all forms of energy in the system. The first term is the kinetic energy of an electron assuming no interaction between the electrons; the interaction component is accounted for in U_{XC}. The second term is the interaction potential between an electron and the atomic nuclei combined. As for U_H, this is the Hartree potential for the electrostatic repulsion between an electron and the full electron density defined by all of the system electrons. The self-interaction going into the Hartree potential is corrected for in U_{XC}. The last term, U_{XC}, accounts for all quantum effects, namely the exchange and correlation potentials for the interaction between same-spin and opposite-spin electrons, respectively. Although the exchange-correlation energy usually constitutes less than 10% of the total system energy, it is critical in determining properties and behavior, like bonding.[49] It is also the main source of inaccuracy in DFT since its exact form is unknown for real systems, and approximations are needed. Only for the hypothetical case of a uniform electron gas in which the electron density does not vary in space can this functional be exactly defined. In the local density approximation, U_{XC} at each position is set equal to that of the uniform electron gas but at the electron density specific to that position. There are other approximations like the generalized gradient approximation (GGA) which incorporates information about the density gradient in different ways. Each of the terms in eqn (1.7) and the total energy can be expressed in terms of the electron density; therefore, the solution is iterative. An initial electron density is assumed, and then the K-S equations are solved simultaneously for the individual electron wave functions. Using the calculated wave function, the electron density is calculated as $\rho(\boldsymbol{r}) = \sum_i |\phi_i(\boldsymbol{r})|^2$ and compared with the initial assumed density and updated accordingly until convergence is achieved to reach a self-consistent solution.

The most attractive feature of DFT is that it is based on first-principles, so there are no experimentally fitted parameters in most cases. However, DFT calculations are computationally intensive which limits the system size, and approximations are often done to decrease the computation time which can affect accuracy. Also, the exchange-correlation functional should be properly chosen since it constitutes the main inaccuracy in the method.

Ab Initio Molecular Dynamics

A brief description of classical molecular dynamics (MD) is given first. This technique involves simulations that track the evolution of a system in time. An interaction potential is specified for the system atoms and Newton’s equations of motion are solved to follow the evolution of the system by calculating the atoms’ positions and velocities. The property values of interest are computed using time averages. It is important to choose a suitable potential and to run the simulation for a long enough time.[50] Since the potential specifies the interaction between atoms, it is a critical determinant of the accuracy of a simulation. Also, long simulation times are important to ensure that the results are independent of the initial configuration and to construct more representative time averages. MD simulations are run under different constraints, or ensembles, and one of the most useful for the calculation of thermophysical properties is the NVT ensemble which is run at constant number of atoms, volume, and temperature. The temperature is typically fixed using a thermostat that is coupled to the system and represents a heat bath with which heat transfer occurs.

DFT can be combined with classical molecular dynamics in *ab initio* molecular dynamics (AIMD). In MD, the accuracy of the interaction potential remains problematic especially for complex systems with many-body interactions. Typically, these potentials are either obtained from experimentally-fitted data or from electronic structure calculations, and the parameterization process is exhaustive especially if it should be repeated whenever the system changes slightly. Also, one should be cautious when extrapolating the model to conditions beyond those at which it was parameterized. In AIMD, on the other hand, forces on the nuclei are computed during the simulation from electronic structure calculations as can be done in DFT. Thus, the interatomic potential continually evolves with time instead of being fixed beforehand. The accuracy of this method is specified by the degree of approximations made in solving Schrödinger's equation. In general, AIMD has advantages and disadvantages.[51] Certainly, a constantly evolving potential is one of the biggest advantages. Apart from this, AIMD allows one to account for interactions that could have not been considered before the simulation. However, AIMD is limited in terms of system size and simulation times due to the high computational requirements. Also, the effect of certain interactions cannot be isolated and studied individually as could be done in classical MD. Nevertheless, the fact that AIMD is based on first-principles makes the approach very appealing.

1.6 Validation of Modelling Approach

For the work presented in every chapter of this thesis, exhaustive validation has been done on the computational methodology. Whenever possible, published results for similar systems have been reproduced or calculated values have been compared to published experimental and theoretical values for gas hydrates. Specifically, Chapter 2 involves comparison of the elastic constants of methane hydrate with experimental and theoretical data values; the computational methodology in Chapter 3 has been successful in reproducing published strength values for a similar system, carbon clathrates, and the calculated elastic constants for ice compared very well with experimental and theoretical values; most of the calculated thermophysical properties in Chapter 4 compared well with experimental and theoretical values at temperature and pressure conditions at which methane hydrate data is available; and the classical force field used in Chapter 5 has been assessed for suitability by reproducing experimental elastic constants of methane hydrate. Many reported properties in this work have been calculated for the first time, so a direct comparison is not possible neither with theoretical or experimental results. A detailed description of what each chapter entails is presented in the next section.

1.7 Thesis Organisation

The thesis organisation is shown in Figure 1-7 and is described in the following pages.

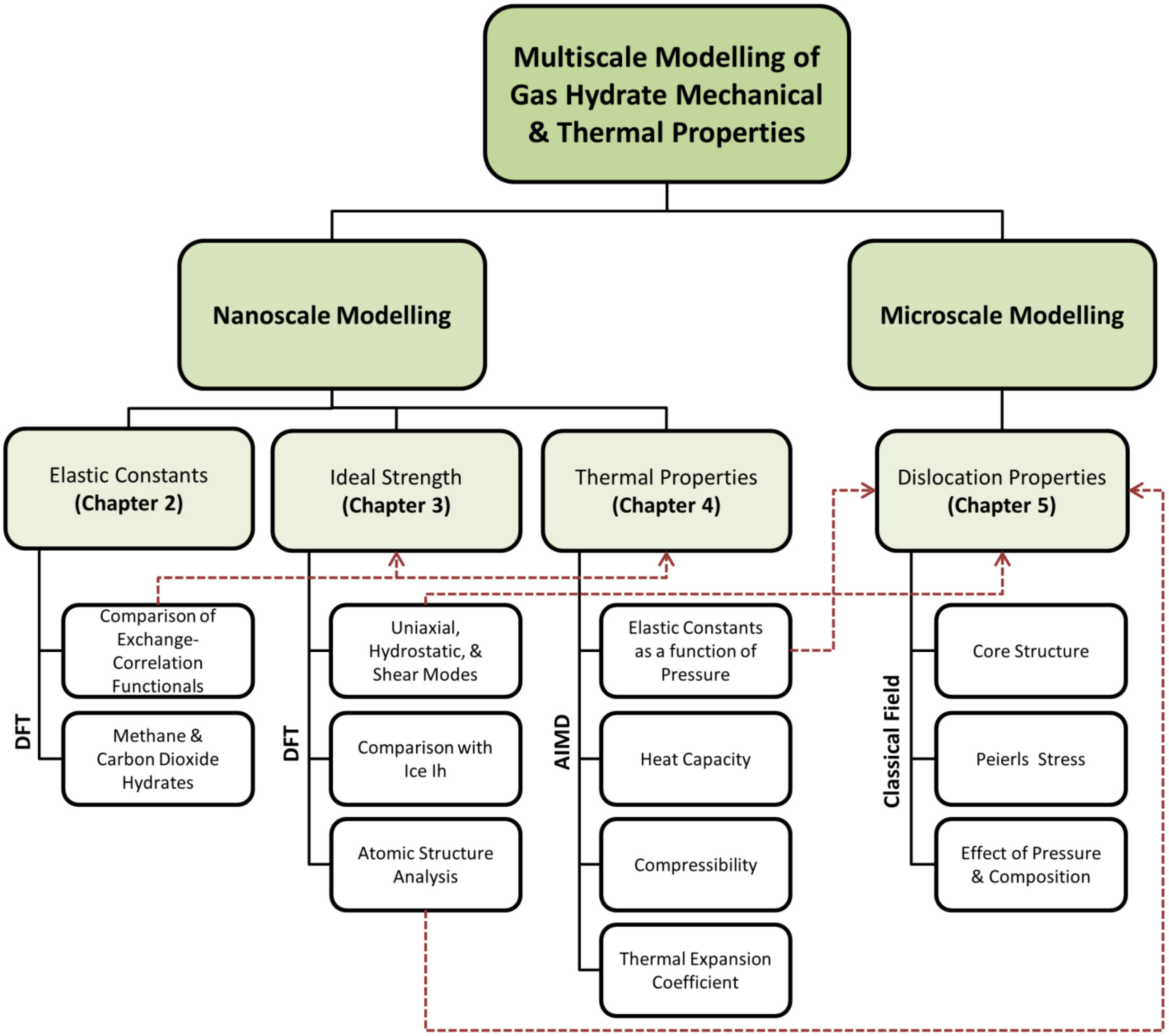

Figure 1-7. Thesis organisation with topics and chapters.

Chapter 2: *Ab Initio* DFT Study of Structural and Mechanical Properties of Methane and Carbon Dioxide Hydrates

This chapter sets the foundation for applying DFT to gas hydrates. The structural and mechanical properties are investigated using this method at the nanoscale for methane and carbon dioxide hydrates. Different exchange-correlation functionals are compared, and the most appropriate was used for the computation of the second-order elastic constants. The polycrystalline properties are estimated form the single lattice results, the elastic isotropy of the compounds is quantified, and the elastic constants of methane and carbon dioxide hydrates are compared. The finding of the most appropriate exchange-correlation functional has been used as input for Chapters 3 and 4.

Chapter 3: Ideal Strength of Methane Hydrate and Ice I_h from First-Principles

Based on the foundational DFT work of Chapter 2, the strength of perfect crystals, also called ideal strength, is investigated in this chapter using DFT for methane hydrate, and ice I_h is considered for comparison. Three different deformation modes at the nanoscale are considered: uniaxial, triaxial, and shear modes. The evolution of the atomic structure with deformation is followed under uniaxial deformation and key features such as bond lengths, bond angles, elastic moduli, and Poisson ratio are analyzed. The differences and similarities in slip systems, strength values, tetrahedral arrangement of water molecules, transverse isotropy, and hydrogen bond lengths are highlighted for methane hydrate and ice. The important slip system in methane hydrate has been used in setting up the simulation system in Chapter 5, and the difference in atomic structure evolution under tension and compression has been used to analyze the results of Chapter 5.

Chapter 4: *Ab Initio* Modelling of Methane Hydrate Thermophysical Properties

While the previous two chapters focus on mechanical properties, this chapter extends the analysis to key thermophysical properties of methane hydrate determined using DFT and AIMD at the nanoscale. Specifically, the pressure dependence of the second-order elastic constants and the temperature and pressure dependence of the heat capacity, compressibility, and thermal expansion coefficient are calculated. A wide range of temperatures and pressures is considered, and the results are compared with those published for ice I_h. Elastic isotropy and the importance of multi-body interactions are elucidated from the DFT results, and some AIMD results are analyzed in light of the findings of Chapter 3. Stability in AIMD is confirmed using the mean square displacement and radial distribution functions. The importance of many-body interactions has been used in choosing a suitable force field in Chapter 5.

Chapter 5: Core Structure and Peierls Stress of Linear Defects in Methane Hydrate

In this chapter, the modelling approach is shifted to plastic deformation at the microscale with classical force fields. It builds on the elastic deformation properties studied in the previous chapters. The core structure and Peierls stress, or the shear stress required to move a dislocation one lattice unit at zero temperature, are studied for edge and screw dislocations. Different cage occupancies and hydrostatic pressures are considered to determine the influence of these variables on the motion of dislocations. Also, the results from the atomistic simulations are compared with the continuum Peierls-Nabarro model.

Chapter 6: Conclusions and Contributions to Original Knowledge

Finally, the key findings of this work are presented in this chapter along with a list of contributions to original knowledge.

2 *Ab Initio* DFT Study of Structural and Mechanical Properties of Methane and Carbon Dioxide Hydrates

Reprinted with permission. This is the authors accepted manuscript of an article published as the version of record in Molecular Simulation © 10 Apr 2014 http://www.tandfonline.com/doi/full/10.1080/08927022.2014.899698

2.1 Preface

Ab initio modelling is essential to enhance the understanding of the structural and mechanical properties of gas hydrates. Methane and carbon dioxide hydrates constitute an interesting class of hydrates due to their applications in energy recovery, gas transportation, and sequestration applications, among others. This chapter sets the foundation for applying DFT to gas hydrates at the nanoscale and uses results obtained using this method to estimate polycrystalline properties. Mechanical properties, such as elastic isotropy, bulk and shear moduli, and density, are important parameters in modelling gas hydrates in their natural settings. The DFT simulation details determined for these properties are needed for studies on other mechanical and thermal properties.

2.2 Summary

The structural and mechanical properties of methane and carbon dioxide hydrates were investigated using density functional theory simulations. Well-established equations of state of solids and exchange-correlation functionals were used for fitting the unit lattice total energy as a function of volume, and the full second-order elastic constants of these two gas hydrates were determined by energy–strain analyses. The polycrystalline elastic properties were also calculated from the unit lattice results. The final results for methane hydrate agree well with available experimental data and with other theoretical results. The two gas hydrates were found to be highly elastically isotropic, but they differed significantly in shear properties. The presented

results for carbon dioxide hydrates are the first complete set reported so far. The results are a significant contribution to the *ab initio* material characterisation of gas hydrates required for ongoing fundamental studies and technological applications.

2.3 Introduction

Clathrate hydrates or gas hydrates are crystalline compounds in which cages of hydrogen-bonded water molecules entrap guest gas molecules.[6] The cages are not all necessarily occupied which makes gas hydrates non-stoichiometric. Different structural forms are possible depending on the guest molecules, temperature and pressure conditions, but the most common types are sI, sII and sH.[11] Natural gas hydrates, found mostly in the permafrost region and deep ocean sites, are believed to be a potential energy resource and a marine geohazard that can lead to landslides.[11] In addition, gas hydrates are being investigated for usage in carbon dioxide sequestration, due to the thermodynamic favourability of the process[4], and in flow assurance, as they are capable of plugging hydrocarbon flow-lines[6].

One of the hindrances in the exploitation of natural methane hydrates is the inadequacy of exploration.[11] Seismic detection methods that utilise bottom-simulating reflectors have commonly been used in the past years.[8,52] The presence of gas hydrates in sedimentary layers is reflected in an increase in seismic speed, among other factors.[8] Therefore, an accurate characterisation of the mechanical properties, which determine seismic speeds, of gas hydrates is essential. This is also important for risk assessment in carbon dioxide sequestration applications.

An overview of the available mechanical properties data for gas hydrates, required also to establish thermodynamic stability, nucleation and growth processes, grain size and grain mechanics, reveals significant inconsistencies which can be partly attributed to differences in samples' quality, cage occupancy and experimental accuracy. For example, the percentage difference in the adiabatic bulk modulus between two experimental results, at the same temperature and pressure, could be 15%.[33,34] One study reports even more divergent results.[53] Though there are other experimental studies[11], there are only two sets of *ab initio* results for the elastic properties of methane hydrates using the Quantum-Espresso package.[36,37] For carbon dioxide hydrates, only one molecular dynamics study reports a single elastic parameter.[54] The available data for the full set of elastic constants are even scarcer.

Since the available mechanical property data are inconsistent and scarce, this article addresses this need and presents a rigorous simulation study of the full second-order elastic constant tensor of methane and carbon dioxide hydrates from a density functional theory (DFT) perspective. DFT is a modelling approach for the determination of the ground-state electronic structure through functionals of the electron density. The calculations in this article are *ab initio* since they are based on first-principles without any experimental input, except for the trial simulation that accounts for dispersion interactions since the method involves some empiricism in its parameters. The results seek to shed light on the main elastic differences between these two hydrates, to present the first full set of second-order elastic constants for carbon dioxide hydrates, to show the effect of some functionals on the bulk modulus, to compare results using different *ab initio* codes, and to provide a reliable reference in the current hydrates' database.

The organisation of this article is as follows. Section 2.4 presents the computational and theoretical methodology including the structure generation, equations of state (EOS) approach to calculate bulk elasticity, energy–strain relations used to calculate elastic constants and details of the DFT methods. Section 2.5 presents a critical analysis of the results along with comparisons with some previous studies.

2.4 Methodology

2.4.1 Structure Generation

Methane and carbon dioxide are sufficiently small molecules to form hydrates in the sI structure under certain pressure–temperature conditions.[6] The primitive lattice unit consists of two 5^{12} cages, of 12 pentagonal faces, and six $5^{12}6^{2}$ cages, of 12 pentagonal and 2 hexagonal faces, with a total of 46 water molecules.[6] The initial structure for both hydrates was based on experimental, high-resolution, neutron diffraction data for deuterated methane hydrates.[55] The hydrogen atoms are disordered just like in the ice I_h structure, and their positions were assigned randomly but in accordance with the Bernal–Fowler ice rules. The cage occupancy was assumed to be 100% with a guest gas molecule at the centre of every cage, in the initial structure.

2.4.2 Full Elasticity Tensor Determination

The sI hydrate structure is cubic; thus, three independent, second-order, elastic constants (c_{11}, c_{12}, c_{44}) are required to describe its elastic properties.[38] The unit lattice bulk modulus (B) can be calculated from:

$$B = \frac{c_{11} + 2c_{12}}{3} \tag{2.1}$$

Alternatively, the bulk modulus (B) can be determined from its thermodynamic definition at constant temperature:

$$B = -\frac{\mathrm{d}P}{\mathrm{d}lnV} = V\frac{\mathrm{d}^2E}{\mathrm{d}V^2} \tag{2.2}$$

where P is the pressure, V is the volume and E is the system's energy. Energy–volume data points can be fitted to an isothermal EOS. The relevant fitting parameters are the bulk modulus at zero pressure (B_0), the pressure derivative of the bulk modulus at zero pressure ($B_0^{'}$) and the equilibrium volume (V_o). In this article, both approaches eqns (2.1) and (2.2) for calculating the bulk modulus (B) are used, and the results are compared.

The second-order elastic constants were calculated from energy analyses of the strained system, initially at the equilibrium volume. While a stress–strain analysis could have been applied, an energy–strain analysis is believed to be preferable.[56] The total energy variation of the system can be expanded as a Taylor series in the elastic strain.[57–59] For a system at zero pressure,

$$\Delta E = \frac{V}{2}\sum_{i=1}^{6}\sum_{j=1}^{6}c_{ij}e_ie_j + O\left(e_i^3\right) \tag{2.3}$$

where ΔE is the energy change resulting from the strain vector $e = \left(e_1, e_2, e_3, e_4, e_5, e_6\right)$ in Voigt notation and V is the volume of the unstrained solid.

Three different sets of small strains were used. A volume-conserving tetragonal strain $e = \left(\delta, -\delta, \delta^2 \big/ \left(1-\delta^2\right), 0, 0, 0\right)$ was applied which according to eqn (2.3) yields:

$$\Delta E = V\left(c_{11} - c_{12}\right)\delta^2 + O\left(\delta^4\right) \tag{2.4}$$

Also, the $\left[100\right]$ and $\left[010\right]$ strain $e = \left(\delta, \delta, 0, 0, 0, 0\right)$ was applied which gives:

$$\Delta E = V\left(c_{11} + c_{12}\right)\delta^2 + O\left(\delta^2\right) \tag{2.5}$$

Last, c_{44} was calculated from the $\left[111\right]$ shear strain $e = \left(0, 0, 0, \delta, \delta, \delta\right)$:

$$\Delta E = \frac{3V}{2} c_{44} \delta^2 + O\left(\delta^2\right) \tag{2.6}$$

To obtain the c_{11}, c_{12}, and c_{44} elastic constants, data from eqn (2.4) were fitted to a polynomial in δ^2 and averaged over negative and positive strains, or equivalently fitted to a polynomial in δ over the entire strain range. Data for eqns (2.5) and (2.6) were expanded as polynomials in δ.

For polycrystalline hydrates and for comparison with experimental data, the Voigt–Reuss–Hill approximation[38] was used for the calculation of the bulk and shear moduli. Young's modulus, Poisson's ratio and compressional and shear wave speeds were then calculated using elastic relations for isotropic solids. For the cubic hydrates under study, the single-lattice bulk modulus is equal to that of the polycrystalline. All equations that were used are listed in the Appendix.

2.4.3 Computational Method

All calculations were performed using the Spanish Initiative for Electronic Simulations with Thousands of Atoms (SIESTA) code[60], which carries out electronic structure and energy calculations using Kohn–Sham DFT. Previous studies have been successful in studying gas hydrates using SIESTA.[61–63] SIESTA uses numerical, atomic orbitals for the basis set. Double ζ plus polarisation basis set was implemented in this work. Different generalised-gradient approximation (GGA) exchange-correlation (XC) functionals were used: Perdew–Burke–Ernzerhof (PBE), revised Perdew–Burke–Ernzerhof (revPBE), and Becke– Lee–Yang–Parr (BLYP). Norm-conserving Troullier– Martins pseudopotentials were used which were obtained from Ref. 64 for the PBE simulations and were generated using the ATOM program[65] with the same cut-off radii as in Ref. 64 for the revPBE and BLYP simulations. In all simulations and based on one unit cell, SIESTA generated a supercell of eight unit cells with periodic boundary conditions. Thorough convergence tests were carried out on the basis set pseudo-atomic orbitals confining cut-off radii, mesh cut-off and k-points. Results are converged with respect to the selected parameters (within 1% of the bulk modulus), and our convergence tests involved simulations with up to 32 k-points although only 4 k-points were found sufficient.

In order to study the effect of the long-range, dispersion van der Waals (vdW) interactions on the elastic properties, the DFT-D2 method was applied since GGA functionals are not sufficient for this purpose. Common approaches are the vdW-DF[66] functional with a nonlocal correlation functional and the DFT-D2 method by Grimme[67]. Each of these methods has its strengths and weaknesses[67]; we used DFT-D2 since it can be directly implemented with the existing XC functionals and is numerically efficient. In the DFT-D2 method, the dispersion energy component involves pairwise-additive, damped potentials that are added to the Kohn–Sham energy. It was applied with the revPBE functional and a distance cut-off of 30 Å for the dispersion interactions. The s_6 scaling parameter in the method was 1.25.[68]

All simulations involved the structural relaxation of all atomic positions with an atomic force tolerance of 5 meV/Å. For the EOS fitting, the system was relaxed at different lattice parameters, and the resulting total energy was used for the fitting. For the second-order elastic constants, the relaxed system starting at the equilibrium volume was strained and allowed to relax, and the resulting total energy was fitted to a polynomial in strain. Relaxation after straining was essential since the deformation can result in force imbalance and an internal strain that leads to highly overestimated elastic constants.[59]

2.5 Results and Discussion

2.5.1 Equations of State

The fitting parameters using three different EOS and three different XC functionals are summarised in Table 2-1, and one fitting curve is shown in Figure 2-1. All equations give bulk moduli that are reasonably close; the absolute difference is 0.13–0.2 GPa. For modelling, the choice of equation depends on the objectives. Murnaghan's equation, which expands the bulk modulus as a linear function of pressure, is valid for low compressions $\left(0 < P < B_0/2\right)$ since it assumes $B_0^{'}$ to be constant.[69] While Birch–Murnaghan equation is based on an expansion of the free energy in terms of the Eulerian strain, the Vinet equation is based on an empirical potential.[70] This gives it better accuracy at high compressions. However, for the pressure, or volume, range considered in this work, both Birch–Murnaghan and Vinet equations give almost the same result.

For the XC functionals, revPBE performs better than the others reported in Table 2-1. The results are analysed based on comparison of the bulk modulus with the most recent, reproducible experimental value of 8.39 GPa at 0 °C and 0 MPa for methane hydrates.[34] Among revPBE, PBE and BLYP, PBE yields the smallest lattice constant and hence the largest bulk modulus, followed by BLYP. This is compatible with previous studies that found PBE overestimates water interactions in hydrogen sulphide clathrates.[62] Also, a study on ice I_h found that both PBE and BLYP overestimate the melting temperature, which implies overestimated water–water interactions, with PBE's overestimation slightly higher.[71] Moreover, accounting for dispersion interactions using DFT-D2 + revPBE results in atomic interactions that are significantly stronger as reflected in the much lower lattice constant and higher bulk modulus. While stronger interactions are expected with the inclusion of dispersion forces, they are highly overestimated. Since DFT-D2 does not incorporate the effect of dispersion interactions into the electron density as vdW-DF does, it would be useful to compare vdW-DF results with the ones presented here to better describe the effect of dispersion interactions on elasticity. Since the bulk modulus from revPBE for methane hydrates is closest to the experimental value, revPBE was used for carbon dioxide hydrate and for the calculation of the elastic constants.

Table 2-1. Equations of state fitting parameters[a]: equilibrium lattice parameter (a_o) and volume (V_o), bulk modulus at zero pressure (B_0), and bulk modulus pressure derivative at zero pressure ($B_0^{'}$).

	CH_4 hydrate: revPBE, $a_o = 11.90$ Å ($V_o = 1684$ Å^3)		CH_4 hydrate: PBE, $a_o = 11.50$ Å ($V_o = 1520$ Å^3)		CH_4 hydrate: BLYP, $a_o = 11.80$ Å ($V_o = 1643$ Å^3)		CH_4 hydrate: revPBE + DFT-D2, $a_o = 11.39$ Å ($V_o = 1477$ Å^3)		CO_2 hydrate: revPBE, $a_o = 11.90$ Å ($V_o = 1687$ Å^3)	
	B_0 (GPa)	$B_0^{'}$	B_0 (GPa)	$B_0^{'}$	B_0 (GPa)	$B_0^{'}$	B_0 (GPa)	$B_0^{'}$	B_0 (GPa)	$B_0^{'}$
Murnaghan[69]	9.82	6.24	15.69	5.43	12.35	6.44	16.71	5.86	10.40	6.27
Birch-Murnaghan[70]	9.97	6.36	15.82	5.39	12.54	6.20	16.82	5.77	10.57	6.35
Vinet[70]	9.98	6.37	15.86	5.37	12.55	6.22	16.84	5.75	10.58	6.37

Note: [a]These were compared with the experimental value of Helgerud et al.[34]:
$B = 8.39 \pm 0.01\ GPa$ ($\pm 6\%$ uncertainty) at 0°C and extrapolated to 0 MPa from 30.5-97.7 MPa.

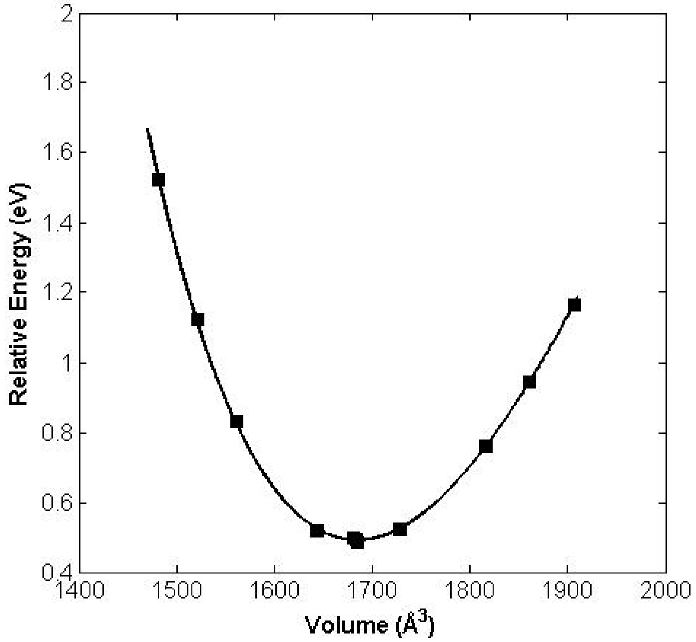

Figure 2-1. Energy vs. volume curve for methane hydrate using revPBE XC functional and fitted using Murnaghan equation.

Carbon dioxide hydrate was found to have a slightly higher bulk modulus than methane hydrate as Table 2-1 shows. Unlike methane, carbon dioxide has a quadrupole moment that adds to the intermolecular interactions with the water molecules that also have a quadrupole moment. Also, the higher bulk modulus is consistent with the higher binding energy of carbon dioxide compared with methane in sI hydrates.[54] From a geometrical perspective, the ratio of molecular diameter to cage diameter is larger for carbon dioxide hydrate compared with methane hydrate.[6] This ratio is even 1.00 for carbon dioxide in the 5^{12} cage. It is interesting to further study the relation between this proximity and the bulk modulus in terms of the attractive and repulsive interatomic interactions and the type of occupied cage.

2.5.2 Elastic Properties

The calculated single-crystal, second-order elastic constants are given in Table 2-2 along with experimental and other theoretical results, and three energy–strain curves are shown in Figures 2-2 and 2-3. The error ranges reported in Table 2-2 correspond to different fitting orders of eqn (2.4) (first- and second-order fits in δ^2); eqns (2.5) and (2.6) fitting results were invariant with second- and third-order fits in δ. All results in Table 2-2 are for 100% cage occupancy. The constant for axial compression c_{11} is 17–52% higher than that found in previous methane hydrate studies shown in Table 2-2. Although Huo et al.[36] have also used the revPBE XC functional, there are some differences in the elastic constants between our work and theirs in addition to their larger equilibrium lattice parameter (optimised at 12.13 Å). Any difference with their work could be because we have used norm-conserving pseudopotentials while they have used ultrasoft ones; indeed, structural differences with different pseudopotentials have been reported in another study.[72] In this work, it appears that c_{11} is the most sensitive parameter to the pseudopotential type. There is a significant difference with the values of Miranda and Matsuoka[37] where the BLYP XC functional was used but with only two sets of strains. The discrepancy with the experimental results can be due to the temperature effect as the elastic constants decrease significantly with temperature, as shown for c_{11} and c_{44} in Shpakov et al.[30].

Table 2-2. Single-crystal elastic constants and Zener anisotropy factor (A_Z), at average values of the elastic constants, with experimental (exp.) and other theoretical (theo.) results.

	CH_4 hydrate				CO_2 hydrate			
	c_{11} (GPa)	c_{12} (GPa)	c_{44} (GPa)	A_Z	c_{11} (GPa)	c_{12} (GPa)	c_{44} (GPa)	A_Z
This work[a]	18.1 ± 0.2	5.7 ∓ 0.2	6.2	0.99	17.0 ± 0.4	8.4 ∓ 0.4	3.8	0.88
Ref. 37, theo.[a]	15.1	4.9	3.8	0.75	-	-	-	
Ref. 36, theo.[a]	14.2	6.0	7.9	1.90	-	-	-	
Ref. 30, theo.[a]	15.5	-	2.9	-	-	-	-	
Ref. 18, exp.[b]	11.9	6.3	3.4	1.21	-	-	-	

Note: [a]Results for 0 K and 0 GPa; [b]results for 296 K and 0.02 GPa.

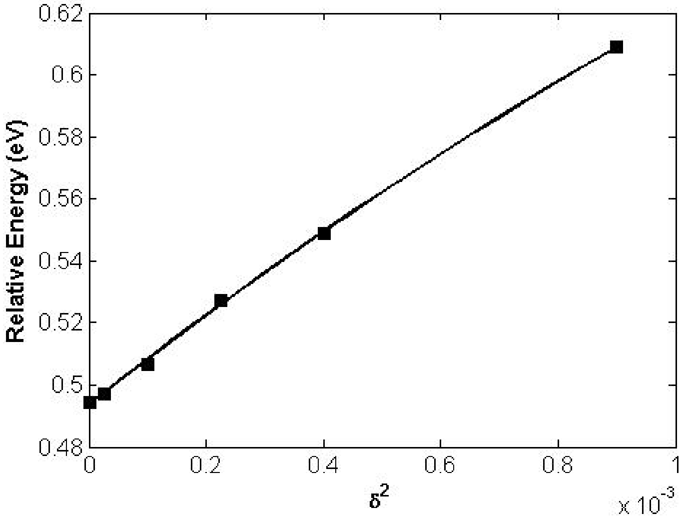

Figure 2-2. Tetragonal strain results for methane hydrate.

As for carbon dioxide hydrate, its second-order constants differ in some respects from those of methane hydrates. The shear constant, c_{44}, displays the greatest difference. Indeed, the value for carbon dioxide hydrate is almost identical with the experimental value of methane hydrate. This difference affects the shear modulus as discussed in more detail later. Both hydrates are almost isotropic as reflected in the Zener anisotropy factor A_Z. A similar observation of isotropy was made in the experimental work of Shimizu et al.[18] using Brillouin spectroscopy on single methane hydrate crystals. They attributed this isotropy to the void-rich network and departure from the ideal tetrahedral arrangement of oxygen atoms in methane hydrates. In addition to these reasons, we believe that the randomness of the hydrogen positions in the cubic lattice may contribute to this isotropy. The slightly lower isotropy of carbon dioxide hydrates in this work may be due to the geometry or bond orientation in carbon dioxide molecules. Also, the bulk moduli calculated from the average elastic constants using eqn (2.1) (9.82 GPa for CH_4 hydrate and 11.3 GPa for CO_2 hydrate) are close to the values in Table 2-1, especially for methane hydrate, which shows consistency between the two methods to calculate the bulk modulus.

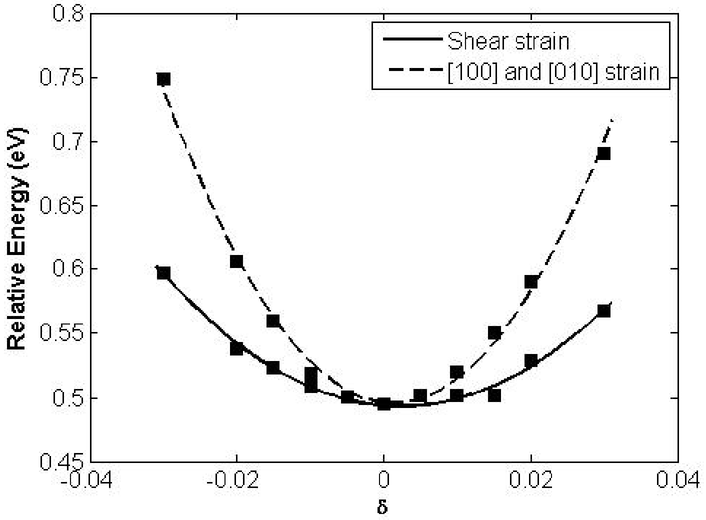

Figure 2-3. Shear and $[100]$ and $[010]$ strain results for methane hydrate.

The polycrystalline elastic parameters of methane hydrate, calculated using the average values of the second-order elastic constants, are given in Table 2-3. The lattice constant calculated in this work agrees much better with the experimental value of Klapproth et al.[33] (within < 0.5%) compared with the other theoretical results. The bulk modulus and speeds of compressional and shear waves in this work agree very well with those of Huo et al.[36]. However, Young and shear moduli are highly overestimated in this work compared with the other results summarised in Table 2-3 because of our much larger c_{11}. However, discrepancies with the experimental data of Helgerud et al.[34] can be partly due to the effect of temperature and different cage occupancies. While our cage occupancy is 100% as explained in Section 2.4, Helgerud et al.[34] assume a 97.6% cage occupancy since they utilise a highly reproducible approach in which this composition is specified based on measurements of gas released from fully reacted hydrates. As expected, most properties are similar to those of ice I_h.[11] However, caution should be taken when extrapolating ice data to hydrates due to some differences in mechanical strength and isotropy, for example.[11] An accurate comparison can only be made after using the same methodology to model ice instead of relying only on available data obtained using different methods.

Table 2-3. Polycrystalline elastic parameters of methane hydrates: density, ρ, bulk modulus, B, shear modulus, G, Poisson's ratio, v, Young's modulus, E, compressional wave speed, V_p, and shear wave speed, V_s, with experimental (exp.) and other theoretical (theo.) results.

	This work[a]	Ref. 37, theo.[a]	Ref. 36, theo.[a]	Ref. 34, exp.[b]	Ref. 33, exp.[c]
a_o (Å)	11.90	12.11	12.13	-	11.955
ρ (g·cm^{-3})	0.943	0.89	0.91	0.92435	-
B (GPa)	9.82	8.3	9.98	8.39±0.01	9.11
G (GPa)	6.23	4.3	4.62	3.541±0.0008	-
v	0.238	0.2776	0.299	0.3151±0.0002	-
E (GPa)	15.4	11.07	12.01	-	-
V_p (km·s^{-1})	4.386	3.981	4.205	3.766±0.002	-
V_S (km·s^{-1})	2.571	1.964	2.250	1.957±0.0002	-

Note: [a]Results for 0 K and 0 GPa; [b]results for 0°C and extrapolated to 0 MPa from 30.5-97.7 MPa with 3%, ±6%, ±4%, ±3%, ±1.5%, and ±1.5% uncertainty in ρ, B, G, v, V_p, and V_s, respectively; [c]results for 271 K, 0 bar for a_o, and 600 bar for B.

For carbon dioxide hydrate, the polycrystalline elastic properties are given in Table 2-4. The compressional wave speed agrees, within 8%, with previous theoretical results reported in the table. Also, the shear modulus differs significantly in this work between methane and carbon dioxide hydrates. The linear shape of the carbon dioxide molecule and its interaction with the host water molecules might explain this. While a shear strain distorts the equilibrium bonding, carbon dioxide hydrates may be easier to shear because the highly electronegative oxygen can attractively interact with the water hydrogen atoms as the alignment of the carbon dioxide molecule adjusts to the strain. Another reason is that part of the applied shear strain in this study appeared to go into resolving the initial residual shear stresses, which were higher in the carbon dioxide hydrate. In fact, the low shear strain values that were used for methane hydrate energy–strain analysis were avoided for the carbon dioxide hydrate because they were observed to mainly resolve these internal stresses. Using the same range for shear strain in the carbon dioxide hydrate case as that in the methane hydrate gives a lower c_{44} of 1.5 GPa which is worth further investigation. These higher internal shear stresses were confirmed with simulations that allowed the lattice to relax freely without maintaining the cubic symmetry. The resulting maximum deviation from the 90^{o} cubic angle was 0.2% and 0.9% for the methane and carbon dioxide hydrates, respectively. This higher deviation reflects higher residual shear stresses that could be caused by the higher guest-to-cage diameter ratio in the carbon dioxide hydrate.

Table 2-4. Polycrystalline elastic parameters of carbon dioxide hydrates with experimental (exp.) and other theoretical (theo.) results.

	This work	Ref. 54, theo.[a]	Ref. 73, exp.[b]
a_o (Å)	11.90	11.60	11.970
ρ (g·cm^{-3})	1.16	-	1.12
B (GPa)	11.3	-	-
G (GPa)	3.98	-	-
v	0.342	-	-
E (GPa)	10.7	-	-
V_p (km·s^{-1})	3.778	3.5	-
V_S (km·s^{-1})	1.852	-	-

Note: [a]Results for 30 K and 1 atm; [b]results for 277 K and 38 atm.

Finally, a check on the applicability of the above-mentioned energy–strain analysis for stress–strain applications was done. For the applied strains, the deviation of the stress results using SIESTA was compared with that predicted using Hooke's law and the average second-order elastic constants in Table 2-2, with the addition of any residual stresses in the unstrained system. The deviation is defined as the absolute difference between the predicted and SIESTA results as a percentage of the maximum stress (for each Voigt strain). The stress results generally displayed the symmetry properties for cubic crystals. For methane hydrate, the average deviations for the tetragonal, $[100]$ and $[010]$ strain and shear strain are 3%, 6% and 8%, respectively. As for carbon dioxide hydrate, the average deviations for the same strains are 10%, 7% and 24%, respectively. The deviations are expected since the linear stress–strain relation was not used for averaging the elastic constants. Also, the residual stresses in the unstrained system could partially cause this deviation because stress–strain relations can only be used to define elastic constants for initial stresses that are exactly isotropic.[57] For the energy–strain analysis in this work, however, residual stresses had no effect.

2.6 Conclusions

In summary, the main contributions of this article are the rigorous determination of the full second-order elastic parameters for methane hydrate and, for the first time, for carbon dioxide hydrate using DFT simulations. Results for different XC functionals and different isothermal EOS were carefully compared and evaluated. The revPBE functional was found to perform best. Although both hydrates are sI formers and exhibited high elastic isotropy, they were found in this work to differ significantly in their shear moduli which should be further investigated and considered in carbon dioxide sequestration applications. The agreement of the results of this work with previous theoretical and experimental results for methane hydrates is generally good considering the mentioned computational differences and the difference with experimental conditions. DFT as implemented in SIESTA was found to be a useful approach within our selected basis set for modelling the elastic properties of hydrates using first-principles if proper functionals and simulation parameters are selected. Thus, it could be considered for predicting the temperature and pressure dependencies of the parameters. However, there is need for more experimental results to build more confidence in the method. The results are a significant contribution to the *ab initio* material characterisation of gas hydrates required for on-going fundamental studies and technological applications.

2.7 Appendix A. Equations of State

This appendix presents all the equations of state used in the paper.

Murnaghan

$$\Delta E(V) = B_0 V_0 \left[\frac{1}{B_0^{'}\left(B_0^{'}-1\right)} \left(\frac{V}{V_0} \right)^{1-B_0^{'}} + \frac{V}{B_0^{'} V_0} - \frac{1}{B_0^{'}-1} \right] \tag{A.1}$$

Birch-Murnaghan:

$$\Delta E(V)=\frac{9B_0V_0}{16}\left\{\left[\left(\frac{V_0}{V}\right)^{2/3}-1\right]^3 B_0' + \left[\left(\frac{V_0}{V}\right)^{2/3}-1\right]^2\left[6-4\left(\frac{V_0}{V}\right)^{2/3}\right]\right\} \tag{A.2}$$

Vinet:

$$\Delta E(V)=\frac{4B_0V_0}{\left(B_0'-1\right)^2}-\frac{2B_0V_0}{\left(B_0'-1\right)^2}\left\{5+3B_0'\left[\left(\frac{V}{V_0}\right)^{1/3}-1\right]-3\left(\frac{V}{V_0}\right)^{1/3}\right\}\exp\left\{-\frac{3}{2}\left(B_0'-1\right)\left[\left(\frac{V}{V_0}\right)^{1/3}-1\right]\right\} \tag{A.3}$$

2.8 Appendix B. Definitions of Elastic Properties

This appendix presents all the definitions of elastic properties used in the paper.

Shear moduli:

$$G_{\mathrm{Re}uss}=\frac{5(c_{11}-c_{12})\,\mathrm{c}_{44}}{4c_{44}+3(c_{11}-c_{12})} \tag{B.1}$$

$$G_{Voigt}=\frac{(c_{11}-c_{12}+3c_{44})}{5} \tag{B.2}$$

$$G=\frac{G_{Voigt}+G_{\mathrm{Re}uss}}{2} \tag{B.3}$$

Bulk moduli:

$$B=B_{Voigt}=B_{\mathrm{Re}uss}=\frac{(c_{11}+2c_{12})}{3} \tag{B.4}$$

Poisson's ratio:

$$v=\frac{\frac{3}{2}B-G}{G+3B} \tag{B.5}$$

Young's modulus:

$$E=2G(1+v) \tag{B.6}$$

Longitudinal wave speed:

$$V_p = \left(\frac{B + \frac{4}{3}G}{\rho} \right)^{1/2} \tag{B.7}$$

Transverse wave speed:

$$V_s = \left(\frac{G}{\rho} \right)^{1/2} \tag{B.8}$$

Zener anisotropy ratio:

$$A_z = \frac{2c_{44}}{c_{11} - c_{12}} \tag{B.9}$$

3 Ideal Strength of Methane Hydrate and Ice I_h from First-principles

Reprinted with permission from Crystal Growth & Design, 15, 5301–5309: http://pubs.acs.org/doi/abs/10.1021/acs.cgd.5b00829

Copyright 2015 American Chemical Society

3.1 Preface

Based on the foundational DFT work of Chapter 2, the strength of perfect crystals, also called ideal strength, is investigated in this chapter using DFT for methane hydrate, and ice I_h is considered for comparison. The ideal strength and the corresponding evolution of atomic structure are essential for numerous applications of natural and synthetic gas hydrates in terms of elastic and plastic deformation. Some of the relevant properties that should be compared for gas hydrates and ice include slip systems, strength values, tetrahedral arrangement of water molecules, transverse isotropy, and hydrogen bond lengths. The finding of the dominant slip system and structural evolution are important for setting up and analyzing large-scale simulations of plastic deformation in gas hydrates.

3.2 Summary

The ideal strength of methane hydrate and ice I_h was investigated and quantified from first-principles calculations. Using Density Functional Theory, methane hydrate was studied under uniaxial, triaxial, and shear deformation modes, and the uniaxial deformation of ice I_h was considered for comparison. The resulting ideal strength was found, and the structural evolution in terms of bond lengths, bond angles, elastic moduli, and Poisson ratio were analyzed throughout the deformation. It was found that methane hydrate displays brittle behavior in terms of its strength and has no dominant slip system. Ice I_h exhibited a higher ideal uniaxial strength compared to the hydrate by deviating from the perfect tetrahedral arrangement of its water molecules. Under uniaxial tension, both structures maintain their transverse isotropy and fail at a critical hydrogen bond length despite the difference in their strength values. Under uniaxial compression, however, the hydrate loses its transverse isotropy unlike ice I_h which maintains it. While ice I_h and hydrates are similar in many of their physical properties, their ideal strength and structural deformation were found to be different. The presented new mono-crystal mechanical properties and insights are a guide to future research in natural and synthetic polycrystalline gas hydrates.

3.3 Introduction

Methane hydrates or clathrates are crystalline compounds in which hydrogen-bonded water molecule cages entrap methane. These guest-host compounds are important mainly because they store significant amounts of methane in the permafrost region and deep ocean sites; however, they also constitute a marine geohazard that can lead to landslides.[11] As constituents of the earth strata, their mechanical properties, including their ideal strength, are of paramount importance. Ideal strength is defined as the stress at the elastic instability of a perfect crystal. While the ideal strength is difficult to observe experimentally, it sets an upper limit for possible strength values since a perfect crystal is the strongest form of a solid.[74]

Calculation of the ideal strength from first-principles is important for understanding the structural evolution of methane hydrates under different loadings. Specifically, the ideal tensile strength achieved as planes separate can be approached near crack tips.[75] This strength can be contrasted with the one under compression. Moreover, the ideal shear strength is an important parameter in plastic deformation since it is related to the width of dislocations and, in perfect crystals, to the resolved shear stress at dislocation nucleation sites.[74,76] As for the ideal hydrostatic strength, this is considered to be the highest of all ideal strengths, and its tensile value is also relevant in crack stability analysis.[77] Finally, understanding the ideal strength and its source allows for the identification of the role of atomic structure in mechanical strength and can reveal the easiest deformation path. Insight gained from the ideal strength of methane hydrates is essential in different fields including gas hydrate production, risk assessment during production, and development of hydrates for gas storage and transportation.

For pure methane hydrates and ice, all strength-related studies we are aware of are experimental and focused on polycrystalline aggregates. While experimental studies[9,21] have revealed that polycrystalline methane hydrate can be more than twenty times stronger than polycrystalline ice and attributed the disparity to dislocation movement and molecular diffusion, it is still essential to consider the strength difference from an atomic structure perspective without dislocations, to better understand the nature of structural distortions under high stress conditions. Additionally, any disparity would reveal important structural differences despite the fact that water molecules take on a tetrahedral arrangement in both gas hydrate, which consists of cages, and ice I_h, which consists of nonplanar hexagonal rings. Apart from this, an atomic analysis allows for prediction of the strength of other hydrates, like carbon dioxide hydrates.

Due to the lack of theoretical studies, this paper mainly explores the ideal strength of methane hydrates from an *ab initio* Density Functional Theory (DFT) perspective and as mentioned above considers ice I_h for comparison purposes. DFT is a modeling approach for the determination of the ground state electronic structure through functionals of the electron density. Specifically, this work aims to quantify the ideal strength of methane hydrates under uniaxial and triaxial tension and compression, to identify the shear strength in different characteristic directions and whether any slip direction is preferred, to compare the results with those of ice I_h, and finally to follow the development of the atomic structure and bonding as the ideal strength is approached.

The organization of this paper is as follows. Section 3.4 presents the computational methodology; section 3.5 presents the results of different deformation modes of methane hydrate; section 3.6 compares the uniaxial strength of methane hydrate with that of ice I_h; section 3.7 reveals the change in atomic structure and elastic stability during deformation.

3.4 Methodology

3.4.1 Atomic Structures

Methane hydrate takes on the sI structure under certain pressure-temperature conditions. The primitive lattice unit consists of two 5^{12} cages, of 12 pentagonal faces, and six $5^{12}6^{2}$ cages, of 12 pentagonal and 2 hexagonal faces, with a total of 46 water molecules.[6] The adopted initial structure was based on experimental, high-resolution, neutron diffraction data for deuterated methane hydrates.[55] The hydrogen atoms are disordered just like in the ice I_h structure, and their positions were assigned randomly but in accordance with the Bernal-Fowler ice rules. The cage occupancy was assumed 100% with a guest gas molecule at the center of every cage, in the initial structure.

For ice I_h, two lattices were considered: the Bernal-Fowler hexagonal lattice[78] and the Hayward-Reimers orthorhombic lattice[79]. The Bernal-Fowler lattice is the simplest hexagonal lattice of 12 water molecules with an ordered arrangement of hydrogen atoms. This order renders the structure polar, with associated piezo- and pyro-electric properties, which is unreasonable.[80,81] Nevertheless, this model has been used in some recent work[82,83], and it is interesting to explore the performance of one of the earliest ice models. The implemented Hayward-Reimers orthorhombic lattice is labelled 3×2×2 in their original work with 96 water molecules. The hydrogen atoms have a random arrangement, and the overall structure has a zero net dipole moment and a minimal net quadrupole moment.

3.4.2 Computational Method

All calculations were performed using the Spanish Initiative for Electronic Simulations with Thousands of Atoms (SIESTA) code[60], which carries out electronic structure and energy calculations using Kohn-Sham DFT. SIESTA uses numerical, atomic orbitals for the basis set. Double zeta plus polarization basis set was implemented. The energy and k-grid cutoff values were chosen high enough to ensure energy convergence, and the uniaxial strength of methane hydrate was found invariant with higher values. The revised Perdew-Burke-Ernzerhof (revPBE) exchange-correlation functional was used based on our previous work[84] that explored different functionals for the elastic properties of methane hydrates. Norm-conserving Troullier-Martins pseudopotentials were used which were generated using the ATOM program[65] with core radii of 1 bohr for carbon, 1 bohr for oxygen, and 0.49 bohr for hydrogen. Periodic boundary conditions were applied in all cases.

All simulations started with the relaxation of atomic positions and lattice vectors to achieve a zero stress state with an atomic force tolerance of 5 meV/Å and a stress tolerance of 0.01 GPa. Next, stresses in characteristic lattice directions were applied incrementally followed by structural relaxation at each increment with the same force and stress tolerance as described above. A conjugate-gradient algorithm was used to make the stress tensor components which do not correspond to the applied stress zero. The ideal strength was determined as the maximum stress value before the lattice loses stability and the forces diverge. Methane hydrate lattices with specific directions along the orthogonal axes were generated using the ASE code[85]. While the primitive structure consisted of 178 atoms, the structure with the $[110]$ direction involved 356 atoms, and the structure with the $[111]$ direction involved 1068 atoms. The stress tensor is calculated in SIESTA as the positive derivative of the total energy with respect to the strain tensor. The strain tensor, $\varepsilon_{\alpha\beta}$, can be calculated from the relation between the strain-free lattice vectors, r_{μ}, and the strained lattice vectors, $\breve{r}_{\mu}$, as follows, where the superscripts below denote Cartesian components:[86]

$$\breve{r}_{\mu}^{\alpha} = r_{\mu}^{\alpha} + \sum_{\beta=1}^{3} \varepsilon_{\alpha\beta} r_{\mu}^{\beta} \tag{3.1}$$

3.5 Deformation Modes of Methane Hydrate

3.5.1 Uniaxial Deformation

Uniaxial tensile and compressive stresses were applied along the $[100]$, $[010]$, $[001]$, $[110]$, and $[111]$ directions for methane hydrate. Although the first three directions are equivalent, they were all considered to determine the computational variation within the same family of directions which helps in determining the acceptable variation in strength for different directions to be considered equivalent. Due to the high computational cost to generate the full stress-strain curve up to the ideal strength in the $[111]$ direction with the larger lattice, a few stresses were considered around the zero stress state only to calculate Young's modulus. A stress was applied incrementally along each of these directions as described in the Methodology section. This is equivalent to applying specific positive (or negative) strains in the considered direction and negative (or positive) strains in the two orthogonal directions until the orthogonal stresses become zero; indeed, this was confirmed since the same strength and Young's modulus were obtained in a tensile deformation along the $[100]$ direction in both approaches. Elastic deformation up to the stability limit was confirmed by decreasing the stress in the $[100]$ direction from its maximum value to the zero stress state which gave an identical deformation path to that in the reverse process. Throughout the deformation, the structure maintained tetragonal symmetry, on average, with a maximum tilt component of 0.34% of the lattice vectors which was essential due to the highly strained nature of fully occupied hydrates. Figure 3-1 shows the resulting strain-stress curves under tensile, positive stress, and compressive, negative stress, deformations in each direction. The ideal strength, or the maximum stress reached in each test, along with Young's modulus, calculated as the reciprocal of the slope of the curves at zero stress, are summarized in Table 3-1.

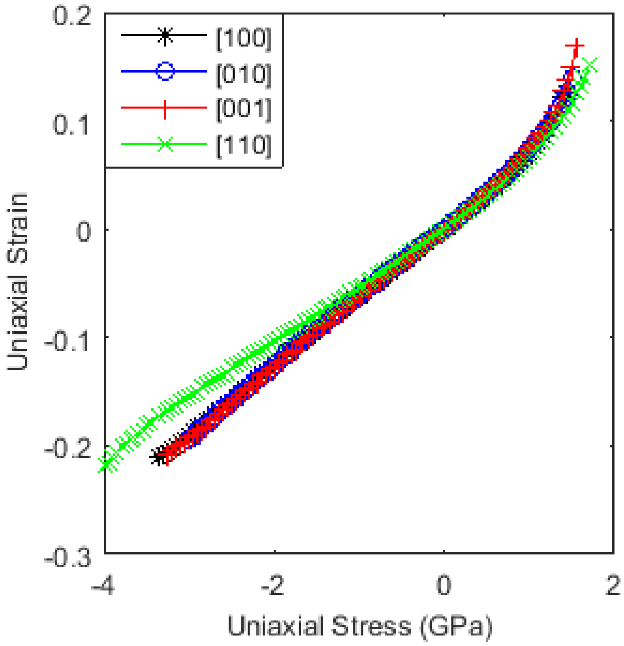

Figure 3-1. Strain as a function of stress in the $[100]$, $[010]$, $[001]$, and $[110]$ directions in methane hydrate.

Table 3-1. The ideal uniaxial strength in tension, σ_{mt}, and compression, σ_{mc}, and corresponding strain, ε_{mt} and ε_{mc}, and Young's modulus, E, for different directions in methane hydrate.

Direction	σ_{mt} (GPa)	ε_{mt}	σ_{mc} (GPa)	ε_{mc}	E (GPa)
$[100]$	1.41 ± 0.05	0.122	-3.35 ± 0.05	-0.211	16.3
$[010]$	1.50 ± 0.05	0.139	-3.01 ± 0.05	-0.195	16.1
$[001]$	1.55 ± 0.05	0.169	-3.25 ± 0.05	-0.208	16.0
$[110]$	1.70 ± 0.05	0.151	-4.00 ± 0.05	-0.218	17.8
$[111]$	-	-	-	-	17.8

As Figure 3-1 and Table 3-1 show, the strain-stress behavior is not significantly different among the four considered directions. In all directions, the compressive region follows an almost linear behavior up to the ideal strength, and the ideal strength and strain values are close to each other. Specifically, the standard deviations in the ideal tensile strength, compressive strength, and Young's modulus in the $\langle 100 \rangle$ family of directions are only 0.058 GPa, 0.14 GPa, and 0.12 GPa, respectively. Such a relatively small variation is expected for a highly strained hydrate system with full cage occupancy and because of computational inaccuracies. Also, methane hydrate can resist stresses under compression more than under tension since the compressive strength is at least twice the tensile strength. Along the $[110]$ direction, methane hydrate appears to be slightly stiffer, with a higher Young's modulus and ideal strength, than other considered directions. Young's modulus along the $[111]$ direction was close to that in the other directions with a value of 17.8 GPa. However, in general, it appears that there is isotropy in terms of the strength in different directions.

3.5.2 Hydrostatic Deformation

Triaxial tensile and compressive stresses were applied for methane hydrate. The resulting volumetric strain, defined as the change in volume divided by the initial volume, as a function of hydrostatic stress is shown in Figure 3-2. It should be noted that the endpoint (-90 GPa) for compressive stresses is only a lower limit for the ideal compressive strength because the hydrate was still stable at such a high stress, but the simulation was discontinued due to its computational cost, time-intractability, and because the significant features of the curve have already been found at this stress. One characteristic feature of hydrostatic deformation is the significantly greater compressive strength (at least -90 GPa) compared to tensile strength (1.10 ± 0.05 GPa). Such a difference, and the greater uniaxial compressive strength compared to tensile strength described earlier, reflects the brittle nature of methane hydrates. This agrees with experimental studies[87] on hydrate-bearing sediments which exhibited a greater tendency for brittleness as the hydrate saturation increased.

Also, the bulk modulus was calculated throughout the deformation as shown in Figure 3-3. This was calculated as the inverse of the volumetric strain vs. hydrostatic stress at each point. At each stress state, a few points were selected nearby, the strain relative to that state was calculated, and a linear fitting was used to calculate the bulk modulus from the slope. Under zero stress, the bulk modulus was found to be 10.5 GPa. As Figure 3-3 shows, as the hydrate approaches its ideal tensile strength, it becomes completely compressible since the bulk modulus becomes almost zero. On the other hand, the bulk modulus becomes very large signifying complete incompressibility as the ideal compressive strength is approached. The sharp dips in Figure 3-3 are reflections of the discontinuities in the strain-stress curve of Figure 3-2 in which the strain does not vary smoothly with stress. This occurs because of sudden changes in the lattice angles. While the lattice is initially cubic, it becomes triclinic under compression with angles that vary throughout the deformation between 86^{o} and 95^{o}. Under tension, the lattice remains cubic, on average, but under compression it loses its symmetry which helps it withstand much higher stresses. Neglecting the sharp dips, the bulk modulus appears to vary linearly with hydrostatic stress, with an absolute value of the slope over the entire range equal to 3.7. Such a linearity validates usage of Murnaghan's equation of state, which assumes a linear relation between the bulk modulus and pressure[69], over a very wide pressure range for hydrates.

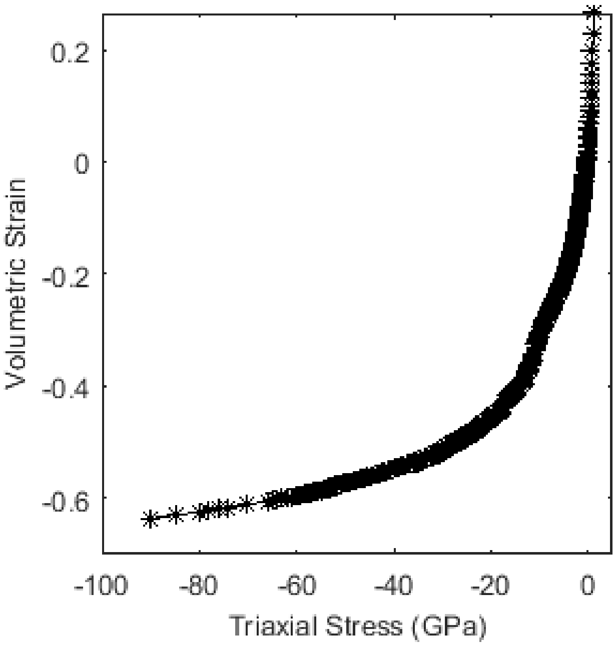

Figure 3-2. Volumetric strain as a function of hydrostatic stress in methane hydrate.

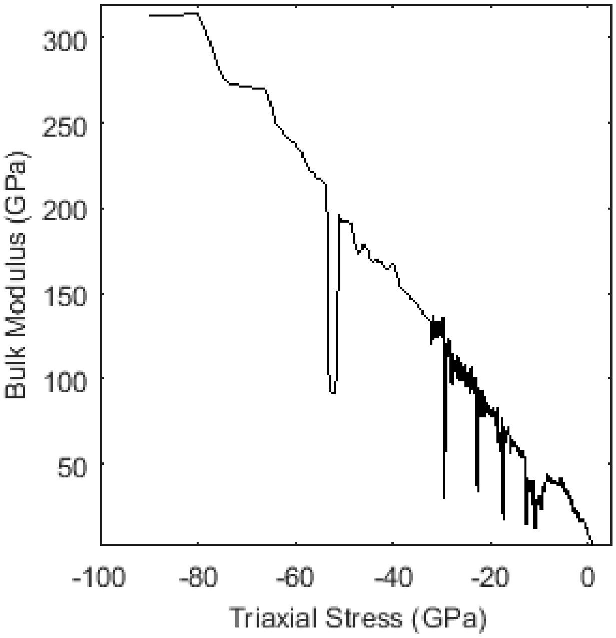

Figure 3-3. Bulk modulus as a function of hydrostatic stress in methane hydrate under hydrostatic deformation.

3.5.3 Shear Deformation

Shear stresses in characteristic lattice directions were applied for methane hydrate. For the lattice with $[100]$, $[010]$, and $[001]$ directions along the x-,y-, and z-axes, respectively, shear stresses on the (100) plane in the $[010]$ and $[001]$ directions were applied. While these are equivalent slip systems, both were considered to provide a measure of acceptable variation among different systems to be considered equivalent. For the lattice with $[110]$, $[1\bar{1}0]$, and $[001]$ directions along the x-,y-, and z-axes, respectively, shear stresses on the (110) plane in the $[1\bar{1}0]$ and $[001]$ directions were applied. For the lattice with $[111]$, $[\bar{1}\bar{1}2]$, and $[\bar{1}10]$ directions along the x-,y-, and z-axes, respectively, a few shear stresses below the ideal strength on the (111) plane in the $[\bar{1}10]$ direction were applied only for the determination of the shear modulus because of the high computation cost required to reach the ideal shear strength. The resulting data are shown in Figure 3-4, and the shear strength, corresponding strain, and shear modulus are summarized in Table 3-2. For the crystallographically equivalent slip systems, the shear strength differs only by 0.25 GPa, and this variation is again due to the strained nature of the system and computational inaccuracies. For shear, isotropy can be observed through the slight variation in strength values among different systems. Thus, it can be concluded that no specific slip system dominates in shear deformation due to the radial arrangement of bonds, as shown in Figure 3-5. This finding is similar to that found earlier for carbon clathrates.[88] The shear modulus was calculated as the reciprocal of the slope of the initial linear portion of the curves. Again, the shear modulus shows little variation in the different systems.

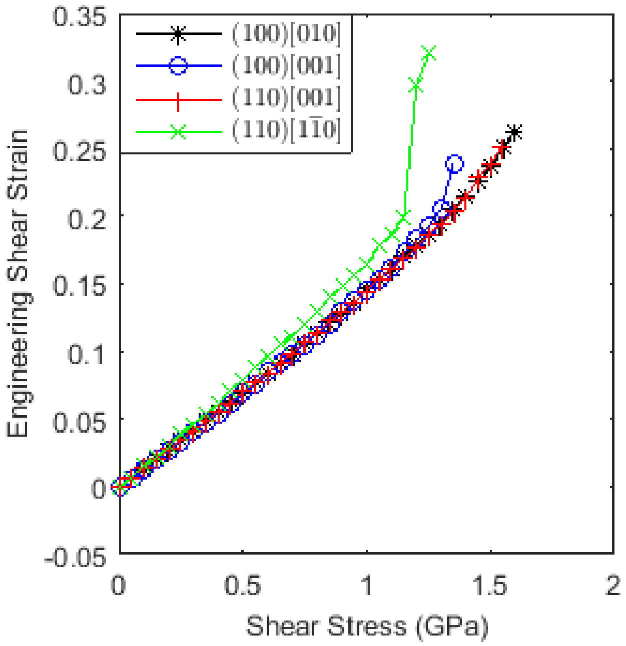

Figure 3-4. Engineering shear strain as a function of corresponding shear stress in methane hydrate.

Table 3-2. The ideal shear strength, σ_{ms}, and corresponding engineering strain, ε_{ms}, and shear modulus, G, for different slip systems in methane hydrate.

Slip system	σ_{ms} (GPa)	ε_{ms}	G (GPa)
$(100)[010]$	1.60 ± 0.05	0.263	7.1
$(100)[001]$	1.35 ± 0.05	0.239	7.3
$(110)[001]$	1.55 ± 0.05	0.252	7.2
$(110)[1\bar{1}0]$	1.25 ± 0.05	0.320	6.4
$(111)[\bar{1}10]$	-	-	6.5

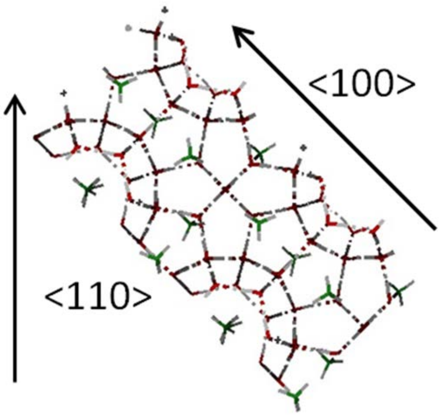

Figure 3-5. Bonding arrangement in methane hydrate lattice, where oxygen, hydrogen, and carbon atoms are colored in red, grey, and green, respectively.

3.6 Comparative Studies of Ice I_h and Hydrate

3.6.1 Elastic Properties

The elastic moduli of ice I_h and methane hydrate do not differ significantly.[11] Since the Bernal-Fowler model of ice is polar, the model was checked initially by evaluation of the second-order elastic constants and bulk modulus. The hexagonal lattice was first allowed to relax fully, and the optimum c/a ratio was found to be 1.622 ±0.011 which compares very well with the temperature-independent, experimental[81] value of 1.62806 ±0.00009.

Next, an energy-strain analysis[89] was performed to calculate the elastic constants. The change in the total energy of the lattice, ΔE, upon the application of a strain, ε, is related to the elastic constants, C_{ij}, and the initial lattice volume, V_o. Using Voigt notation, this translates to $\Delta E = \frac{V_o}{2}\sum_{i,j} C_{ij}\varepsilon_i\varepsilon_j$. The calculation details are outlined in the Appendix, and the results are summarized in Table 3-3.

Table 3-3. Second-order elastic constants, C_{11}, C_{12}, C_{13}, C_{33}, C_{55}, and bulk modulus, B, of ice I_h compared to other experimental (exp.) and theoretical (theo.) results.

	This work	Other work, exp.[90] (0 °C)	Other work, exp.[91] (-16 °C)	Other work, exp.[92]	Other work, theo.[93] (-193 °C)
C_{11} (GPa)	13.28	$13.68 \pm 0.2\%$	13.929 ± 0.041	13.33 ± 1.98	13.7
C_{12} (GPa)	5.61	$6.94 \pm 0.2\%$	7.082 ± 0.039	6.03 ± 0.72	11.1
C_{13} (GPa)	4.61	$5.63 \pm 0.2\%$	5.765 ± 0.023	5.08 ± 0.72	10.5
C_{33} (GPa)	14.06	$14.76 \pm 0.2\%$	15.010 ± 0.046	14.28 ± 0.54	16.7
C_{55} (GPa)	3.26	$2.97 \pm 0.2\%$	3.014 ± 0.011	3.26 ± 0.08	1.9
B (GPa)	7.81	$8.48 \pm 0.2\%$	8.899[a]	8.15[a]	12.03[a]

[a]The bulk modulus was calculated from the above elastic constants.

For a model as simple as Bernal-Fowler's with its known deficiencies in terms of a non-zero dipole moment, the agreement between our DFT results for the elastic constants and the experimental results is very good. Thus, this model was further used for the calculation of the ideal strength of ice I_h along with the Hayward-Reimers model.

3.6.2 Ideal Strength

Uniaxial stresses were applied along the c-axis of ice I_h. This direction also exhibited the maximum strength in an experimental study of the strength of single ice crystals with the c-axis oriented 3^o-70^o to the loading direction.[94] However, our results cannot be compared quantitatively with the experimental results primarily due to the significant role of dislocations in deformations.

The results for compressive and tensile deformation using the Bernal-Fowler and Hayward-Reimers lattices are shown in Figure 3-6, and the results are summarized in Table 3-4. The case of an empty hydrate was also considered to observe the effect of structural differences without including methane which introduces compositional differences as well. For the Bernal-Fowler lattice, only the case with compressive stresses was considered due to computational convergence issues under tension which are expected to be due to the polar nature of the hexagonal lattice. The compressive strength of the Bernal-Fowler lattice is 1.5 times greater than that of the Hayward-Reimers lattice; however, both lattices have almost identical curves in the common stress region. This higher strength can be explained by the fact that after -6 GPa the Bernal-Fowler lattice loses its hexagonal symmetry, as reflected by the sharp drop in strain at that point. Also, for both lattice models, a step-wise strain-stress behavior can be observed near zero stress. The empty hydrate displays a lower strength, especially under compression. This may be related to the empty hydrate's lower Young's modulus and its more open structure since the atomic packing factor of ice is 1.13-1.14 times greater than that of the empty hydrate. Additionally, the simulation on the empty hydrate revealed the significant role of methane in hydrates. Under zero stress, the lattice constants of the methane hydrate and empty hydrate were 11.88 Å and 11.71 Å, respectively. This difference can be explained by the repulsive interaction between the methane molecules and the cages leading to a larger lattice. Also, the empty hydrate has a larger tensile strength (1.35 times) and a smaller compressive strength (0.76 times) compared to the methane hydrate. The initially smaller size of the empty hydrate lattice allows it to sustain larger tensile stresses until the atomic separations reach a critical value, and the repulsive contribution of methane allows methane hydrates to resist higher compressive stresses before collapsing compared to the empty hydrate. As for ice I_h with its stacking of non-planar hexagonal rings, it can display an ideal uniaxial strength of more than 1.5 times greater, in both tension and compression, than that of methane hydrate that takes on a cage-like structure. This disparity in strength is further explained in the next section on atomic structure analysis. This finding is quite significant in that it is opposite to the behavior of the same materials but in a polycrystalline form with defects. While polycrystalline hydrate can be more than 20 times stronger than polycrystalline ice[9,21], perfect ice crystals can be stronger than perfect hydrate crystals. This is important in crack analysis since the perfect crystal strength values, not the polycrystalline ones, are the observed stresses near crack tips.

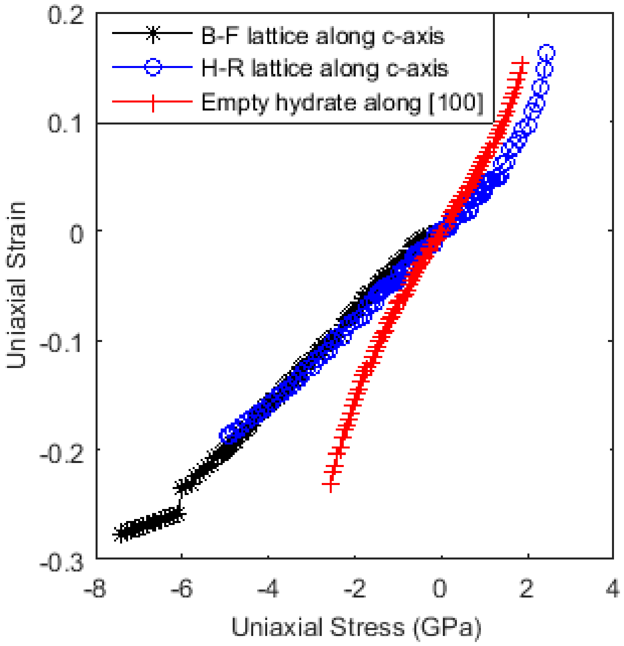

Figure 3-6. Strain as a function of stress along the c-direction in Bernal-Fowler (B-F) and Hayward-Reimers (H-R) ice I_h lattices and along the $[100]$ direction in the empty hydrate.

Table 3-4. The ideal uniaxial strength in tension, σ_{mt}, and compression, σ_{mc}, and corresponding strain, ε_{mt} and ε_{mc}, and Young's modulus, E, along the c-axis in ice I_h and along $[100]$ for the empty hydrate.

	Bernal-Fowler lattice	Hayward-Reimers lattice	Empty sI hydrate lattice
σ_{mt} (GPa)	-	2.45 ± 0.05	1.90 ± 0.05
ε_{mt}	-	0.162	0.153
σ_{mc} (GPa)	-7.40 ± 0.10	-4.95 ± 0.05	-2.55 ± 0.05
ε_{mc}	-0.277	-0.187	-0.232
E (GPa)	23.8	25.1	15.7

3.7 Atomic Structure

In this section, the uniaxial deformation results along the $[100]$ direction were selected in order to compare the structural evolution with that of ice I_h under the same deformation along the c-axis. Due to the elastic isotropy of methane hydrate, the structural evolution is not expected to differ significantly along different directions under uniaxial deformation. For ice I_h, the Hayward-Reimers lattice was used since results are available under both tension and compression.

3.7.1 Bond Lengths and Angles

The O--H hydrogen bond length, the O-H covalent bond length, the nearest neighbor O-O distance, and the O-O-O angle were calculated under tension and compression. The average values of these parameters along with their standard deviations at each point are shown in Figures 3-7 to 3-10. For hydrogen bonding, the hydrogen bond angles throughout the deformation for both the hydrate and ice were in the range of 151°-180° which is within the acceptable range for hydrogen bonding[95].

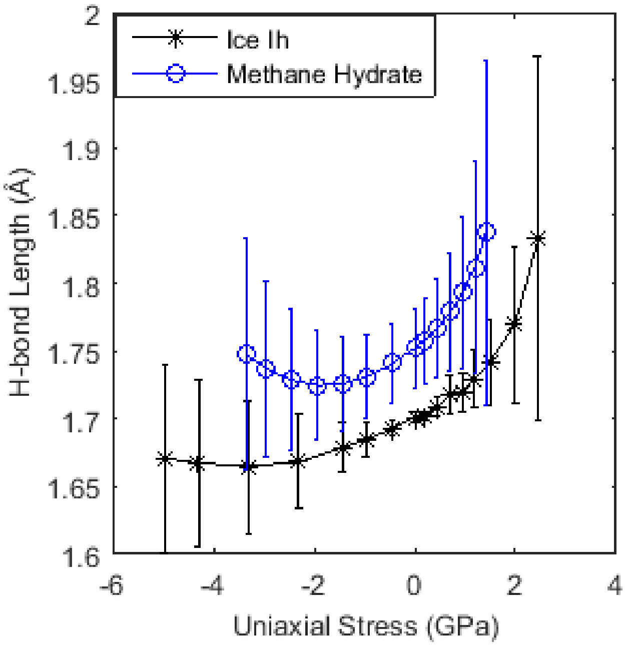

Figure 3-7. Average hydrogen bond length and standard deviation under uniaxial stress for methane hydrate, along the $[100]$ direction, and ice I_h, along the c-axis.

In general, the hydrogen bond length, O--H, and the covalent bond length, O-H, display opposite trends. This is a reflection of the fact that as the hydrogen bond strength decreases, the covalent bond strength increases, and the nearest neighbor O-O distance increases. Such a behavior has been observed in studies on hydrogen bonding.[96]

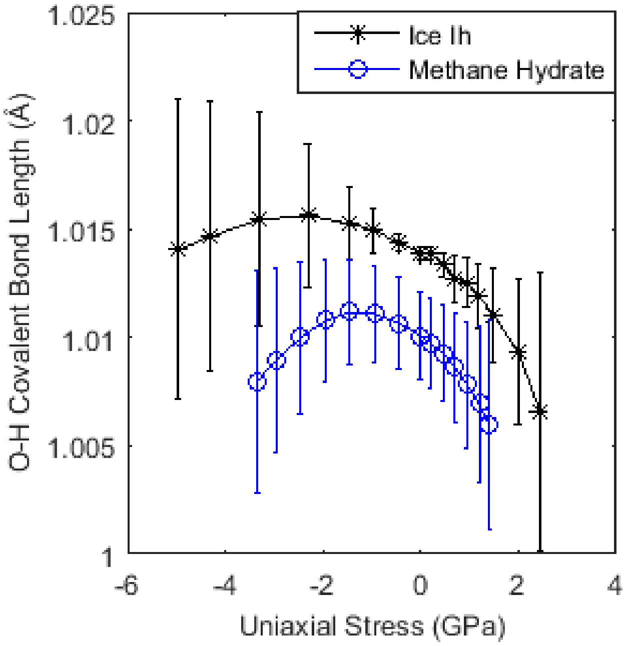

Figure 3-8. O-H covalent bond length and standard deviation under uniaxial stress for methane hydrate, along the $\left[100\right]$ direction, and ice I_h, along the c-axis.

Under tension for both the hydrate and ice, the average hydrogen bond length increases with stress, but the average O-H covalent bond length decreases to counteract the effect of tension. Initially, the hydrate exhibits a larger hydrogen bond length and a smaller O-H covalent bond length than ice I_h. This can be attributed to the repulsive interaction between the methane molecules and the cages in the hydrate which leads to a weakening of the hydrogen bond strength. Also, the hydrate exhibits a larger variation in the bond lengths initially, as reflected by the larger standard deviation range under zero stress, which is due to the greater structural variation in hydrates. Specifically, the methane hydrate has two types of cages with pentagonal and hexagonal faces and different connections between the cages. Ice I_h, on the other hand, includes only sheets of nonplanar hexagonal rings which makes the hydrogen bond connectivity more uniform. However, at the ideal strength, it can be seen that the average hydrogen bond length, covalent bond length, and nearest neighbor O-O distances are around 1.83 Å, 1.006 Å, and 2.84 Å, respectively, for both the hydrate and ice I_h despite their structural differences. Thus, at this point, it seems that the repulsive contribution due to the methane no longer plays a role in stability, and the hydrate loses stability due to the weakening of the hydrogen bonds until the structure can no longer be sustained. It is interesting to note that the empty hydrate under uniaxial deformation also approaches this critical hydrogen bond length; specifically, its average hydrogen bond length, covalent bond length, and O-O distance at the ideal tensile strength are 1.81 Å, 1.007 Å, and 2.81 Å, respectively.

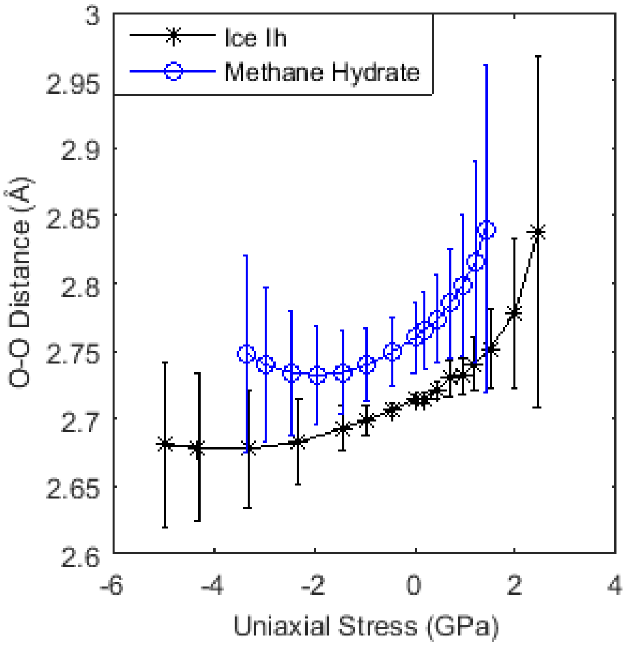

Figure 3-9. Nearest neighbor O-O distance and standard deviation under uniaxial stress for methane hydrate, along the $[100]$ direction, and ice I_h, along the c-axis.

Under compression, the hydrate and ice display a parabolic length-stress behavior. Initially, there is a decrease in the average hydrogen bond length and an increase in the covalent bond length to counteract the effect of compression, but as the ideal compressive strength is approached, the hydrogen bond length begins to increase and the covalent bond length begins to decrease. This reflects the limit of nearest atomic distances as repulsive interactions increase with compressive stress. This is evident as the nearest neighbor O-O distance also increases close to the ideal compressive strength. For a visualization of the difference in electron densities, the Appendix shows the electron density contours under tensile and compressive stresses where there is a clear separation and merging, respectively, of electron densities around the oxygen atoms.

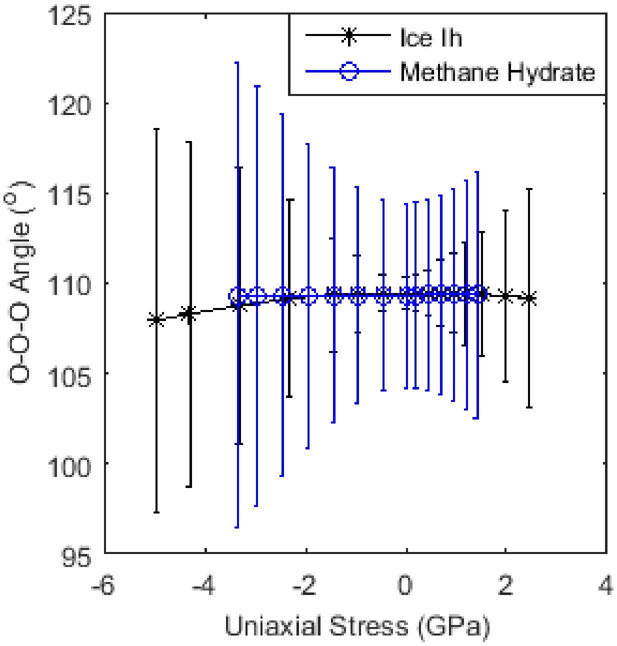

Figure 3-10. O-O-O angle and standard deviation under uniaxial stress for methane hydrate, along the $[100]$ direction, and ice I_h, along the c-axis.

As for the O-O-O angle, this can give insight on the larger ideal strength of ice I_h compared to methane hydrate. Under zero stress, both the hydrate and ice I_h exhibit a tetrahedral arrangement of water molecules with an average O-O-O angle of 109.34^o and 109.47^o, respectively. The greater standard deviation of the hydrate, as shown in Figure 3-10, is due to the greater structural variation of the hydrate that involves cages of hexagons and pentagons as explained previously. Under both compression and tension, the hydrate maintains the tetrahedral arrangement with a maximum variation from its initial average bond angle of 0.03%. Ice I_h, on the other hand, deviates 0.25% and 1.38% from its initial average bond angle under tension and compression, respectively. This greater variation allows ice to maintain higher stresses by adjusting its internal structure slightly without changing its overall orthorhombic lattice symmetry. The hydrate, on the other hand, has a more rigid internal structure which fails when it can no longer maintain its almost perfect tetrahedral arrangement.

Under tensile deformation where there is no limitation on the nearest O-O distance, the relationship between the O-O-O angle and the O-O distance follows a linear relationship. Using the measures of distortion developed by Robinson et al. for coordination polyhedra[97], the angle variance and quadratic elongation parameters for the oxygen atoms of the tetrahedral complexes of ice and hydrate are defined as follows, where l_i is the O-O distance, l_o is the O-O distance at the zero stress state, and θ_i is the O-O-O angle:

$$\text{Quadratic Elongation} = \sum_{i=1}^{4} \left(l_i / l_o \right)^2 \Big/ 4 \tag{3.2}$$

$$\text{Angle Variance} = \sum_{i=1}^{6} \left(\theta_i - 109.47^o \right)^2 \Big/ 5 \tag{3.3}$$

As Figure 3-11 shows, these two parameters are linearly dependent for both the hydrate and ice. Each point is an average of the calculated parameters for all oxygen atoms, and the coefficient of determination for the linear fit was 0.99 and 0.98 for the hydrate and ice, respectively. The larger angle variance and quadratic elongation for the hydrate is compatible with the larger standard deviation of the O-O-O angle and O-O distance in hydrates as explained previously. This linearity reflects that the quadratic elongation and angle variance are equally valid parameters when quantifying the distortion of the tetrahedral arrangement of water molecules in hydrates and ice.

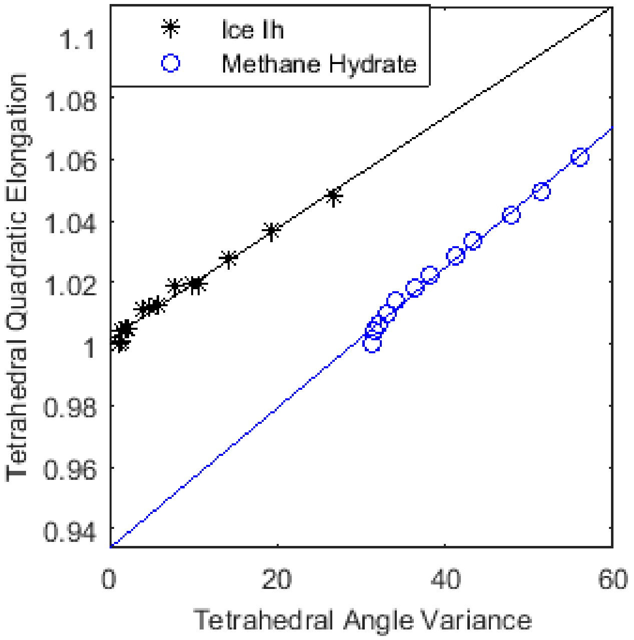

Figure 3-11. Quadratic elongation as a function of angle variance under uniaxial stress for methane hydrate, along the $[100]$ direction, and ice I_h, along the c-axis.

3.7.2 Guest-to-cage Radius Ratio

The ratio of the radius of the entrapped methane molecules to the radius of the water cages was computed throughout the deformation. Molecular radii were computed using three-dimensional trapezoidal integration of the electron density assuming[98] the molecule occupies a spherical volume, centered at the heavy nucleus, which includes 98% of the total, electron density of the molecule. The cage radius was calculated as the distance from the carbon atom of the guest molecule to an oxygen atom of the water molecule in the cage minus the water molecule radius. The guest-to-cage ratio was averaged over all water molecules in cages of the same type, and the standard deviation was computed. Under zero stress, the average ratios for the large and small cages deviate only 4% and 3%, respectively, from literature values for methane hydrate[6].

As Figure 3-12 shows, the average guest-to-cage radius ratio does not vary significantly under compression and tension for both types of cages: the two 5^{12}, of 20 water molecules each, and the six $5^{12}6^{2}$ cages, of 24 water molecules each. Nevertheless, the standard deviation increases significantly as the ideal strength is approached especially under compression. At all points, the standard deviation of the ratio is greater for the larger $5^{12}6^{2}$ cage compared to the smaller 5^{12} cage, and this difference is due to the less spherical shape of the larger cage. Under tension, the standard deviation bars do not exceed unity. Under compression, however, a guest-to-cage radius ratio greater than one can be used to indicate instability. It is known that hydrates do not have a specific guest-to-cage ratio; however, the guest molecule has to be small enough to fit into the cages.[6] While there is no significant change in the average ratio under uniaxial compression, a significant number of radii become greater than unity just before instability, as indicated by the standard deviation. Specifically, this is the case for the 5^{12} cage, while the larger $5^{12}6^2$ guest-to-cage ratio does not exceed unity at all times. A ratio greater than unity indicates size limitations of the cage which can explain instability.

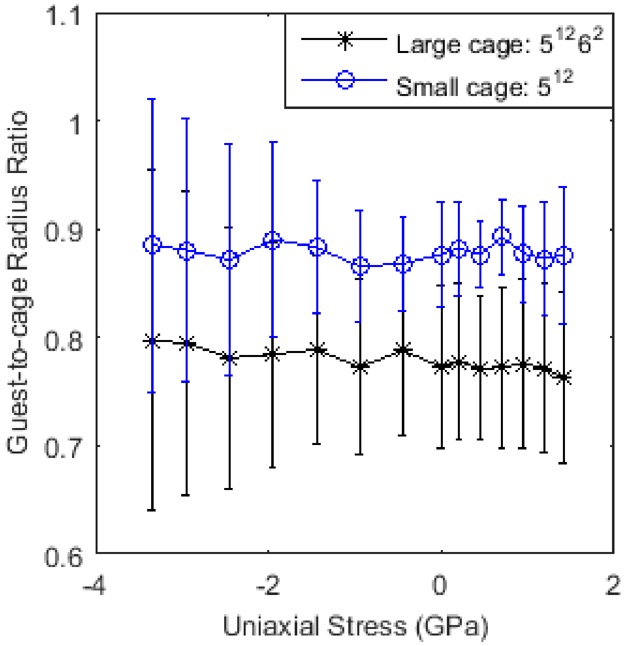

Figure 3-12. Guest-to-cage radius ratio under uniaxial stress for methane hydrate along the $[100]$ direction.

It is worth noting that under high compressive stresses hydrogen bonding between the guest methane molecule and the water cage was observed. The observation was based on the criteria[95] of C-H--O hydrogen bond length less than 2.8 Å and hydrogen bond angle greater than 90°. At a uniaxial, compressive stress of 2.5GPa, 20% of the methane hydrogens form hydrogen bonds, and the percentage increases with applied stress. At the ideal compressive strength, 50% of the hydrogens in the methane molecules satisfied these criteria. Specifically, half of the hydrogens of the methane molecules in the large cages and half of the hydrogens of the methane molecules in the small cages were involved in hydrogen bonding. This signals changes in the intermolecular interactions between the guest molecules and the water cage. Similar to our finding, a diffraction experiment has indicated a shortening of the C-O distances at high pressures to values that are within the upper limit for weak hydrogen bonds.[99]

3.7.3 Poisson Ratio

Poisson ratio was calculated as the negative of the derivative of the transverse strain to the axial strain throughout the uniaxial deformation. At each stressed state, nearby strains were calculated with respect to that stressed state, and the derivative was calculated from a fitted, linear function of the transverse strain as a function of the axial strain. The two curves shown in Figure 3-13 for every structure correspond to Poisson ratio calculated from the two transverse strains. At certain points, Poisson ratio varied abruptly due to the discrete nature of the data points; therefore, the curves have been smoothed out using a moving average filter in order to make them clearer. Near the zero stress state, the hydrate and ice have almost the same Poisson ratio of 0.26. Both the hydrate and ice display transverse isotropy due to the small difference between the two curves for each structure; however, the hydrate loses this isotropy near the ideal compressive strength which reflects the non-uniform deformation of the cage structure in hydrates at high stresses. As Figure 3-13 shows, the ratio is greater for ice compared to the hydrate under tensile stress and smaller under compressive stress. This reveals the greater in-plane interaction for the hydrate under tension and for the ice under compression, and the disparity is more under compressive stresses. It also shows the effect of the dominantly repulsive interaction of the guest molecule with the hydrate cage which increases the in-plane interaction under tensile axial stress to resist the corresponding compressive transverse strain and decreases the in-plane interaction under compressive axial stress to assist tensile transverse strain. As the ideal tensile strength is approached, the ratio approaches zero for both the hydrate and ice.

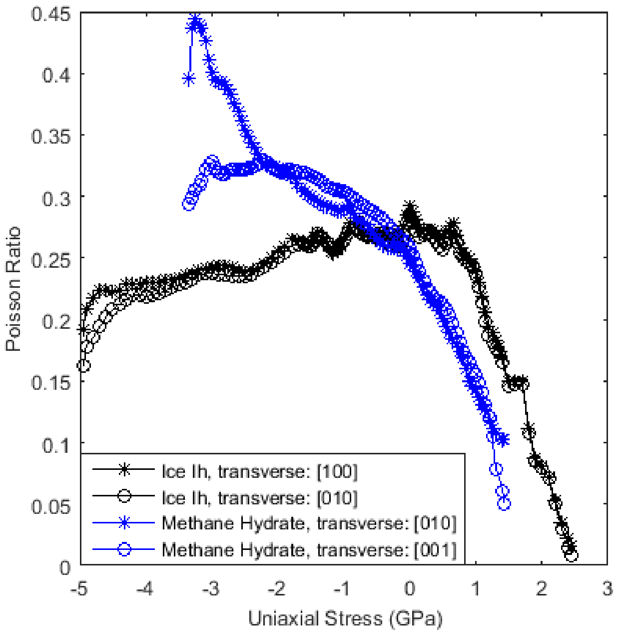

Figure 3-13. Poisson ratio under uniaxial stress for methane hydrate, along the $[100]$ direction, and ice I_h, along the c-axis.

3.7.4 Elastic Constants

In order to ensure the elastic stability of the hydrate structure throughout the deformation, the elastic stability criteria were evaluated. A stress-strain analysis was used by applying a small strain, ε, to the lattice under uniaxial stress, and relating the change in stress, $\delta\tau$, to the applied strain such that $\delta\tau = B\varepsilon$. The stability criterion can be summarized by $\det\left|\overline{B}\right| > 0$, where $\overline{B}$ represents the symmetrized, stress-corrected second-order elastic constants' matrix.[100] The detailed stability criteria and the method used to calculate them are described in the Appendix, but the equivalent stability criteria for the hydrate lattice under uniaxial stress, σ, along the $[100]$ direction can be summarized as, where E_{100} is Young's modulus along $[100]$ and Voigt notation is used:

$$E_{100} > 0\ , C_{22} - C_{23} > 0\ , C_{44} > 0\ , \text{and } C_{55} + \sigma/2 > 0$$

As can be seen in Figure 3-14, the stability criteria are not violated throughout the deformation which ensures that the ideal strength values are not overestimated. The criteria, or at least one of them, are expected to be violated rapidly very near the ideal strength; however, it was not possible to observe this because very small stress increments were needed as the ideal strength is approached and due to the high computational demand of these stress-strain analyses.

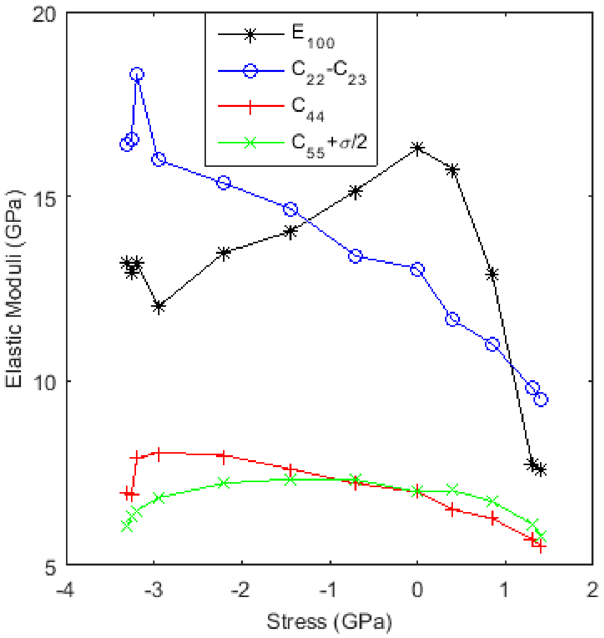

Figure 3-14. Variation of the elastic moduli with uniaxial stress along the $[100]$ direction for methane hydrate.

3.8 Conclusions

The ideal strength of methane hydrate has been determined using first-principles calculations. Uniaxial, triaxial, and shear deformation modes have been performed. Methane hydrate exhibited elastic isotropy in terms of its uniaxial strength, and it reflected brittle behavior in terms of its much higher strength under uniaxial and triaxial compression compared to tension. Over a wide pressure range, its bulk modulus varied linearly with pressure which is important when developing or using equations of state for these materials. The hydrate also seems to have no dominant slip systems which can be traced back to its radial bond arrangement.

As for ice I_h, its ideal uniaxial strength under tension and compression has been determined using first-principles calculations. An early model of ice, the Bernal-Fowler lattice, yielded second-order elastic moduli which agreed very well with experimental data. Unlike the polycrystalline forms of hydrates and ice I_h in which the hydrate is much stronger than ice, perfect ice crystals were found to be more than 1.5 times stronger than perfect hydrate crystals which is important in crack analysis. The ice lattice was able to achieve a higher strength by deviating from the perfect tetrahedral arrangement of water molecules. However, at the ideal uniaxial tensile strength, both the hydrate and ice reached the same critical value of the hydrogen bond length. Finally, the ice was found to maintain its transverse isotropy throughout the uniaxial deformation, but the hydrate lost this isotropy as the ideal compressive strength was approached since its cages deformed non-uniformly. The presented new mono-crystal mechanical properties and insights are a guide to future research in natural and synthetic polycrystalline gas hydrates.

3.9 Appendix A. Calculation of Ice I_h Second-order Elastic Constants

To calculate the second-order elastic constants of the hexagonal ice I_h lattice, an energy-strain analysis was used. The lattice was first relaxed to achieve a zero stress state, and then strains were applied by multiplying the lattice vectors with the strain matrix, e:

$$e = \begin{bmatrix} 1+\varepsilon_1 & \varepsilon_6/2 & \varepsilon_5/2 \\ \varepsilon_6/2 & 1+\varepsilon_2 & \varepsilon_4/2 \\ \varepsilon_5/2 & \varepsilon_4/2 & 1+\varepsilon_3 \end{bmatrix}$$

For a lattice initially under no stress, and using Voigt notation, the energy of the strained lattice can be expressed as:

$$E = E_o + \frac{V_o}{2}\sum_{i,j} C_{ij}\varepsilon_i\varepsilon_j \tag{A.1}$$

where E_o is the energy of the unstrained lattice, and C_{ij} is the second-order elastic constant.

For the hexagonal lattice, there are five independent elastic constants: C_{11}, C_{12}, C_{13}, C_{33}, and C_{55}. Thus, five sets of strains were applied. These are summarized below with the resulting energy of the lattice after distortion.

Case 1: Basal plane size distortion while maintaining hexagonal symmetry.

$$e = \begin{bmatrix} 1+\alpha & 0 & 0 \\ 0 & 1+\alpha & 0 \\ 0 & 0 & 1 \end{bmatrix}$$

$$E = E_o + V_o\left(C_{11} + C_{12}\right)\alpha^2 \tag{A.2}$$

Case 2: Distortion to a monoclinic lattice.

$$e = \begin{bmatrix} 1+\alpha & 0 & 0 \\ 0 & 1-\alpha & 0 \\ 0 & 0 & 1 \end{bmatrix}$$

$$E = E_o + V_o\left(C_{11} - C_{12}\right)\alpha^2 \tag{A.3}$$

Case 3: Changing z-axis length while maintaining hexagonal symmetry.

$$e = \begin{bmatrix} 1 & 0 & 0 \\ 0 & 1 & 0 \\ 0 & 0 & 1+\alpha \end{bmatrix}$$

$$E = E_o + \frac{V_o}{2}C_{33}\alpha^2 \tag{A.4}$$

Case 4: Distortion to a triclinic lattice.

$$e = \begin{bmatrix} 1 & 0 & \alpha \\ 0 & 1 & 0 \\ \alpha & 0 & 1 \end{bmatrix}$$

$$E = E_o + 2V_oC_{55}\alpha^2 \tag{A.5}$$

Case 5: Triaxial size distortion.

$$e = \begin{bmatrix} 1+\alpha & 0 & 0 \\ 0 & 1+\alpha & 0 \\ 0 & 0 & 1+\alpha \end{bmatrix}$$

$$E = E_o + \frac{V_o}{2}\left(2C_{11} + 2C_{12} + 4C_{13} + C_{33}\right)\alpha^2 \tag{A.6}$$

For each case, nine equally-spaced strain values, α, were applied between -0.02 and +0.02, and the elastic constants were obtained from fitting a quadratic equation to the energy-strain data points. The bulk modulus was calculated as $B = \frac{2}{9}\left(C_{11} + C_{12} + 2C_{13} + C_{33}\right)$.

3.10 Appendix B. Electron Density Contours

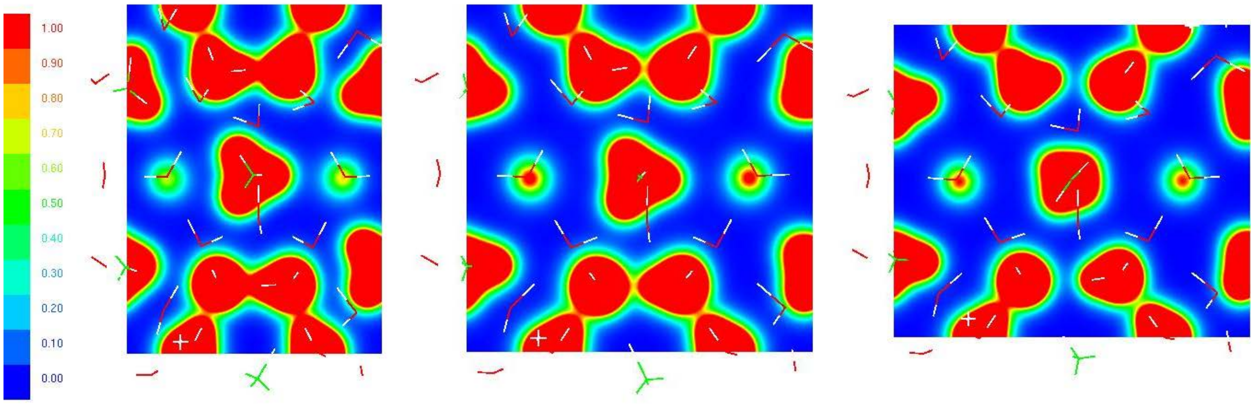

Figure B-1. Electron density contours of methane hydrate under uniaxial deformation along $[100]$ at the ideal compressive strength, left, at the zero stress state, middle, and at the ideal tensile strength, right. The electron density is shown up to 0.045 electron/bohr^3 and perpendicular to a transverse direction along its midpoint.

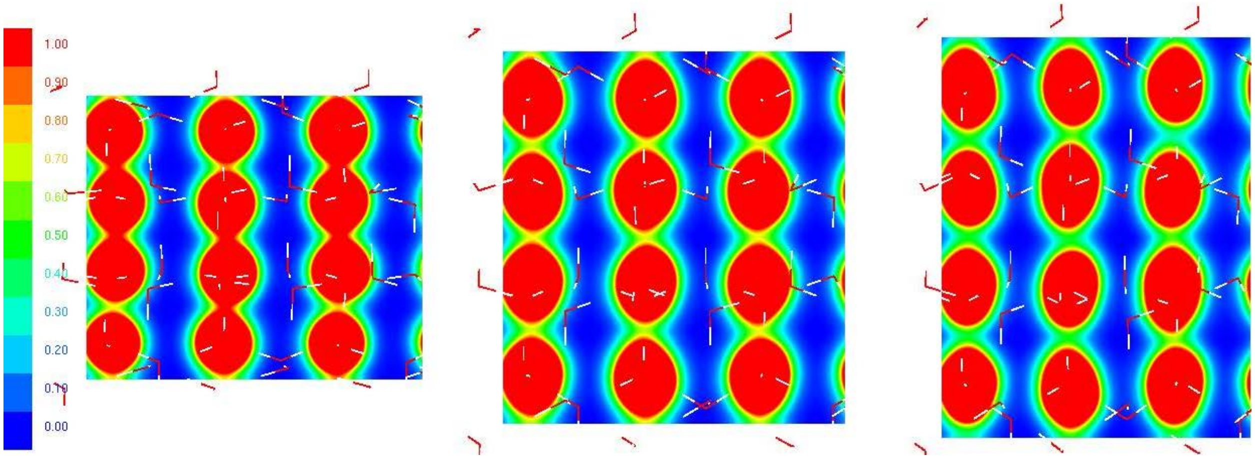

Figure B-2. Electron density contours of the Hayward-Reimers ice I_h lattice under uniaxial deformation along the c-axis at the ideal compressive strength, left, at the zero stress state, middle, and at the ideal tensile strength, right. The electron density is shown up to 0.0035 electron/bohr^3 and perpendicular to a transverse direction along its midpoint.

3.11 Appendix C. Evaluation of Elastic Stability Criteria

The elastic stability criteria were determined using a stress-strain analysis for the lattice throughout the uniaxial deformation. For a system in state X under stress $\tau_{ij}\left(X\right)$ that undergoes a small deformation described by strain ε, the new system state can be denoted by Y, and the relation between the stresses in the different states can be described as:

$$\tau_{ij}(Y)=\tau_{ij}(X)+B_{ijkl}\varepsilon_{kl}+O\left[\varepsilon^2\right] \tag{C.1}$$

where $B_{ijkl}=C_{ijkl}+\frac{1}{2}\left(\delta_{ik}\tau_{jl}+\delta_{jk}\tau_{il}+\delta_{il}\tau_{jk}+\delta_{jl}\tau_{ik}-2\delta_{kl}\tau_{ij}\right)$, C_{ijkl} is the second-order elastic constant of the lattice, and τ_{ij} is the stress value of the lattice before the small strain is applied. The stability criterion is applied to the symmetrized matrix $\overline{B}=1/2\left(B^T+B\right)$ such that $\det\left|\overline{B}\right|>0$. Under uniaxial deformation along $\left[100\right]$, the cubic lattice becomes tetragonal, and the uniaxial stress can be denoted as σ for simplicity, and the non-zero $\overline{B}$ components, using Voigt notation, are:

$\overline{B}_{11}=C_{11}+\sigma$, $\overline{B}_{12}=\overline{B}_{13}=C_{12}-\sigma/2$, $\overline{B}_{22}=\overline{B}_{33}=C_{22}$,

$\overline{B}_{23}=C_{23}$, $\overline{B}_{44}=C_{44}$, $\overline{B}_{55}=\overline{B}_{66}=C_{55}+\sigma/2$

The equivalent stability criteria are:

$\overline{B}_{11}\left(\overline{B}_{22}+\overline{B}_{23}\right)-2\overline{B}_{12}^2>0$

$\overline{B}_{22}-\overline{B}_{23}>0$

$\overline{B}_{44}>0$, $\overline{B}_{55}>0$

The first criterion is equivalent to ensuring that Young's modulus is positive, since $E_{100}=\left[\overline{B}_{11}\left(\overline{B}_{22}+\overline{B}_{23}\right)-2\overline{B}_{12}^2\right]/\left(\overline{B}_{22}+\overline{B}_{23}\right)$. Young's modulus was calculated as the inverse of strain vs. stress at each point of interest. At each stress state X, a few points were selected nearby, and the strain relative to the state X was calculated. A linear fitting was used to calculate Young's modulus from the resulting stress-strain relation at each state of interest. The other stability criteria were tested by application of specific strains and a linear fit to the resulting stress change vs. applied strain, $(\delta\tau)-(\alpha)$, relation. The strains were applied as described in Appendix A.

The second stability criterion was tested by application of the following strain matrix

$$e=\begin{bmatrix}1 & 0 & 0\\ 0 & 1+\alpha & 0\\ 0 & 0 & 1-\alpha\end{bmatrix}$$

$$\delta\tau_2=-\delta\tau_3=\left(\bar{B}_{22}-\bar{B}_{23}\right)\alpha=\left(C_{22}-C_{23}\right)\alpha \tag{C.2}$$

The third stability criterion was tested by application of the following shear strain matrix.

$$e=\begin{bmatrix}1 & 0 & 0\\ 0 & 1 & \alpha\\ 0 & \alpha & 1\end{bmatrix}$$

$$\delta\tau_4=2\bar{B}_{44}\alpha=2C_{44}\alpha \tag{C.3}$$

The fourth stability criterion was tested by application of another shear strain matrix.

$$e=\begin{bmatrix}1 & 0 & \alpha\\ 0 & 1 & 0\\ \alpha & 0 & 1\end{bmatrix}$$

$$\delta\tau_5=2\bar{B}_{55}\alpha=\left(2C_{55}+\sigma\right)\alpha \tag{C.4}$$

The considered α range was between -0.02 to +0.02 in increments of 0.01. It should be noted that for the second stability criterion in the last three points plotted under compression in Figure 3-14, the symmetry requirement of $\delta\tau_2=-\delta\tau_3$ did not apply for all applied strains, and the $\delta\tau_2$ vs. α curve was discontinuous and exhibited two different slopes. This is due to the approaching elastic instability, and the $\delta\tau_3$ vs. α was used for these points since it exhibited a well-defined slope.

4 *Ab Initio* Modelling of Methane Hydrate Thermophysical Properties

Physical Chemistry Chemical Physics, 2016, DOI: 10.1039/C5CP06530E – Reproduced by permission of the PCCP Owner Societies

4.1 Preface

While the previous two chapters focus on mechanical properties, this chapter extends the analysis to key thermophysical properties of methane hydrate determined using DFT and AIMD at the nanoscale. Specifically, the pressure dependence of the second-order elastic constants and the temperature and pressure dependence of the heat capacity, compressibility, and thermal expansion coefficient are calculated. All of these properties are essential for modelling controlled gas hydrate production, risk assessment studies, gas hydrate detection, and studies of climate change. Some of these properties can reveal the importance of many-body interactions which is essential when choosing suitable force fields for microscale simulations.

4.2 Summary

Key thermophysical properties of methane hydrate were determined using *ab initio* modelling. Using density functional theory, the second-order elastic constants, heat capacity, compressibility, and thermal expansion coefficient were calculated. A wide and relevant range of pressure-temperature conditions were considered, and the structures were assessed for stability using the mean square displacement and radial distribution functions. Methane hydrate was found to be elastically isotropic with a linear dependence of bulk modulus on pressure. Equally

significant, multi-body interactions were found to be important in hydrates, and water-water interactions appear to strongly influence compressibility like in ice I_h. While the heat capacity of hydrate was found higher than that of ice, the thermal expansion coefficient was significantly lower, most likely due to the lower rigidity of hydrates. The mean square displacement gave important insight on stability, heat capacity, and elastic moduli, and the radial distribution functions further confirmed stability. The presented results provide a much needed atomistic thermoelastic characterization of methane hydrates and are essential input for the large-scale applications of hydrate detection and production.

4.3 Introduction

Gas hydrates consist of hydrogen-bonded water molecules that form cages in which guest gas molecules are trapped in a crystalline structure. Although these compounds can be synthesized, they also exist naturally mainly as methane hydrates in the permafrost region and deep ocean sites. One of the conservative assessments suggests that hydrates within the earth incorporate an energy content that is twice the energy stored in all other fossil fuel deposits.[2] One method to produce the methane stored in these natural hydrates is to replace it with carbon dioxide due to the thermodynamic favorability of the process.[4] Moreover, methane hydrates can constitute potential storage and transportation media since they require milder conditions to form and remain stable compared to liquefied natural gas (LNG) although their gas density is less.[6] Additionally, gas hydrates are considered for water desalination applications with efficiencies that vary with the guest molecule.[101] In more critical applications, gas hydrates are problematic aspects in flow assurance, and natural hydrates constitute a marine geohazard that can lead to landslides.[11]

In almost all of the previously mentioned applications, the thermophysical properties of gas hydrates are essential. For natural gas hydrate detection in sedimentary layers, seismic waves are usually employed, and their speed is a strong function of the elastic constants and compressibility of the media through which they propagate.[8] Additionally, the heat capacity comes into play when modelling controlled natural gas production from hydrate-bearing sediments.[10] As for the thermal expansion coefficient, this is an important parameter in risk assessment studies of the mechanical stability of the earth strata hosting hydrates.[11] On a larger scale, thermal properties are needed in studies of climate change related to methane release from natural hydrates.[10]

Furthermore, the thermophysical properties of hydrates can give insight on the properties of other hydrogen-bonded compounds like ice. While most properties are very similar, one of the characteristically different thermal properties is thermal conductivity.[102] Methane hydrate, for example, has a much lower thermal conductivity compared to ice I_h due to the vibrational coupling of guest gas and host water molecules.[17] Knowledge of the heat capacity can give reasonable insights on the difference in conductivity since both are related through the Debye equation.[103] Moreover, an accurate calculation of the thermophysical properties of hydrates and ice allows for the determination of the range in which ice properties cannot be extrapolated to hydrates which has not yet been precisely quantified.

Several studies have been done for the investigation of the thermophysical properties of hydrates. Different hydrate structures were considered with different guest molecules, but most studies have been experimental so far. For methane hydrate, experimental values exist for the second-order elastic constants[18], compressibility or bulk modulus[12,33,34,104,105], thermal expansion coefficient[31,106–108], and heat capacity[10,109–111]. These experimental values are available in a very limited and insufficient temperature and pressure range. Additionally, experiments usually involve costly set-ups and are time-consuming, and the results can be strongly influenced by residual gas or water and the existence of micropores which are all factors that are not well quantified or discussed in experimental work.[11,35] There are few studies[36,37,84] that report theoretical values for the elastic constants using *ab initio* simulations of methane hydrate. Other studies[30,35] on methane hydrate use classical molecular dynamics or lattice dynamics to calculate compressibility, thermal expansion coefficient, and heat capacity, but none are based on first-principles.

Due to the above-mentioned shortcomings associated with experimental work and the lack of sufficient theoretical studies, this paper quantifies key thermophysical properties of methane hydrate using *ab initio* Density Functional Theory (DFT). This work uses first-principles to determine the ground state electronic structure using electron density functionals. Specifically, this work aims to quantify the second-order elastic constants, heat capacity, compressibility, and thermal expansion coefficient of methane hydrates over a wide temperature and pressure range and to analyze the structural stability throughout the considered conditions.

The organization of this paper is as follows. Section 4.4 presents the computational methodology; section 4.5 presents the calculated thermophysical properties; section 4.6 analyzes the structural stability under different conditions.

4.4 Methodology

4.4.1 Simulation Method

Methane hydrate was simulated using the sI cubic hydrate lattice. The primitive lattice unit consists of two 5^{12} cages, of 12 pentagonal faces, and six $5^{12}6^{2}$ cages, of 12 pentagonal and 2 hexagonal faces, with a total of 46 water molecules.[12] The structure was generated as described in our earlier work[84] with 100% cage occupancy. A single lattice with periodic boundary conditions was considered. It should be stressed that the system size and composition were limited by the *ab initio* nature of the simulations. These simulations provide accurate results based on first-principles without any experimentally-fitted parameters, but they are very computationally intensive such that only a single lattice with 100% cage occupancy was possible. While larger systems may be more accurate, we compare most of our results with results from other research groups which use larger systems but with same occupancy using classical molecular dynamics. Also, occupancies less than 100% are definitely more realistic, but this case provides an important limiting case, and many experimental studies report such a high occupancy (such as 100%[18,108] and 97.6%[34]).

The Spanish Initiative for Electronic Simulations with Thousands of Atoms (SIESTA) code[60] was used for the DFT simulations. Double zeta plus polarization basis set was implemented, and the energy and k-grid cutoff values were chosen high enough to ensure the convergence of the results. The maximum cut-off radius for the atoms' potential was 3.3 Å, which involved a compromise between simulation speed and potential extent and is within the acceptable range for such a small system size. The revised Perdew-Burke-Ernzerhof (revPBE) exchange-correlation functional was used based on our previous work[84] which analysed the suitability of different functionals. Norm-conserving Troullier-Martins pseudopotentials were used which were generated as described in our previous work[112].

Ab initio molecular statics were used for the determination of the pressure dependence of the second-order elastic constants. At specific, fixed lattice constants, all atoms were first allowed to relax using a conjugate-gradient algorithm with an atomic force tolerance of 5 meV/Å. Next, specific strains were applied, the atoms were allowed to relax to achieve the force tolerance mentioned above, and an energy-strain analysis was used for the determination of the second-order elastic constants.

Ab initio molecular dynamics (AIMD) simulations were used for the calculation of the remaining thermophysical properties. First, a conjugate-gradient relaxation of the atomic positions and lattice vectors at different pressures was done. Next, NVT AIMD simulations that implement the Nosé thermostat were performed at different temperatures and lattice volumes. The thermostat mass was specified as recommended by Nosé[113], and a 1 fs integration time step was used. Since the simulations involved a wide range of conditions, the equilibration time was ensured to be long enough and was in the range of 5-30 ps with a total simulation time in the range of 52-63 ps. The total number of simulated systems was 20 at different temperatures and volumes with 1 system at 210 K, 5 at 250 K, 6 at 273 K, 1 at 283 K, 4 at 293 K, and 3 at 323 K, and 8 different system volumes were considered. Although no barostat was used, pressure equilibrated well enough with a maximum acceptable total drift of 14% of the average pressure value. The evolution of temperature, pressure, and energy in a typical run after equilibration is shown in Figure 4-1, where a linear fit was used to calculate drift.

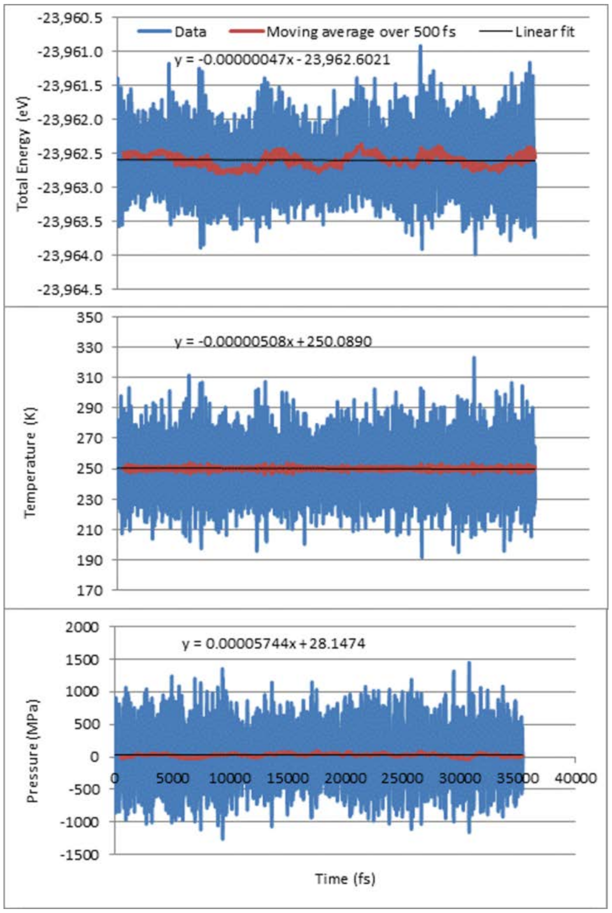

Figure 4-1. Time evolution of system total energy, temperature, and pressure after equilibration at 250 K and 29 MPa.

4.4.2 Calculation of Thermophysical Properties

For the calculation of the pressure dependence of the second-order elastic constants, the approach of Sin'ko and Smirnov[39] was followed. The lattice vectors, r_μ, were distorted by the application of a strain tensor, $\varepsilon_{\alpha\beta}$, to obtain strained lattice vectors, $\breve{r}_\mu$, as follows, where the superscripts below denote Cartesian components[86]:

$$\breve{r}_\mu^\alpha = r_\mu^\alpha + \sum_{\beta=1}^{3} \varepsilon_{\alpha\beta} r_\mu^\beta \tag{4.1}$$

By considering the effect of pressure, P, on the expansion of the lattice energy as a function of strain and as detailed in Ref. 39, Table 4-1 shows how the application of specific strains was used to calculate the elastic constants for the cubic lattice, where V_1 is the unstrained lattice volume and E is the total lattice energy. The relations in Table 4-1 are based on the expansion of the total lattice energy change, ΔE, with respect to the applied strain, γ: $\Delta E = A\gamma + D/2\,\gamma^2 + \ldots$, where A and D are coefficients that depend on the pressure, the chosen strains, and the corresponding second-order elastic constants. Quadratic polynomials were used for the energy fit, and six sets of strains were used, although three are sufficient, in order to ensure that the calculated elastic constants are independent of the applied strains. An average value for the elastic moduli along with standard deviation values were calculated using four data sets: two calculated from the six sets of strains and two from higher energy and k-grid cutoff values. Strains were applied in the range of -2% to 2% in increments of 0.5%. The pressure-corrected elastic constants, C_{ij}, and bulk modulus, B, were evaluated as follows:

$$C_{11} = c_{11} - P,\ \ C_{12} = c_{12} + P,\ \ C_{44} = c_{44} - P,\ \ B = \frac{C_{11} + 2C_{12}}{3} \tag{4.2}$$

Table 4-1. Strains used to calculate second-order elastic constants and corresponding energy derivatives.

Strain (unlisted $\varepsilon_{\alpha\beta} = 0$)	$\frac{1}{V_1}\frac{\partial^2 E}{\partial \gamma^2}\Big\vert_{\gamma=0}$
1. $\varepsilon_{11} = \varepsilon_{22} = \gamma$	$2(c_{11} + c_{12} - P)$
2. $\varepsilon_{13} = \varepsilon_{31} = \gamma$	$2(2c_{44} - P)$
3. $\varepsilon_{11} = \gamma$	$c_{11} - P$
4. $\varepsilon_{12} = \varepsilon_{21} = \varepsilon_{13} = \varepsilon_{31} = \varepsilon_{23} = \varepsilon_{32} = \gamma$	$6(2c_{44} - P)$
5. $\varepsilon_{22} = \gamma$	$c_{11} - P$
6. $\varepsilon_{11} = \varepsilon_{22} = \varepsilon_{33} = \gamma$	$3(c_{11} + 2c_{12} - P)$

For the calculation of the other thermophysical properties, standard thermodynamic relations and statistical mechanics fluctuation formulas specific to the canonical NVT ensemble have been used. First, heat capacity at constant volume, C_V, was calculated from the derivative of a quadratic polynomial fitted to the energy vs. temperature data points at constant volume. This result was compared with that obtained from the fluctuation formula. The pertinent equations are as follows:

$$C_V = \left.\frac{\partial E}{\partial T}\right|_V \tag{4.3}$$

$$C_V = \frac{\langle E^2 \rangle - \langle E \rangle^2}{k_B T^2} \tag{4.4}$$

where E is the total system energy, T is temperature, V is volume, and k_B is Boltzmann's constant. Next, standard thermodynamic relations were used to calculate the isothermal compressibility, β_T, isothermal bulk modulus, B_T, volumetric thermal expansion coefficient, α_V, heat capacity at constant pressure, C_P, adiabatic compressibility, β_S, and adiabatic bulk modulus, B_S, as follows:

$$\beta_T = -\frac{1}{V}\left.\frac{\partial V}{\partial P}\right|_T = \frac{1}{B_T} \tag{4.5}$$

$$\alpha_V = \beta_T \left.\frac{\partial P}{\partial T}\right|_V \tag{4.6}$$

$$C_P = C_V + \frac{TV\alpha_V^2}{\beta_T} \tag{4.7}$$

$$\beta_S = \beta_T \frac{C_V}{C_P} = \frac{1}{B_S} \tag{4.8}$$

All derivatives were calculated from second-order polynomial fits of the relevant thermodynamic parameters and evaluated at simulated conditions.

4.5 Thermophysical Properties

4.5.1 Second-order Elastic Constants

The second-order elastic constants, bulk modulus, Cauchy relation, and Zener anisotropy factor were evaluated over a wide pressure range. The results as a function of hydrostatic pressure are shown in Figures 4-2 to 4-4, where positive and negative pressure values refer to compressive and expansive stresses, respectively. Each of the elastic constants has a physical meaning which is relevant when studying the elastic response of crystals upon the application of stresses or strains. C_{11} is the modulus for axial compression, C_{12} is the modulus for dilation on compression, and C_{44} is the shear modulus. C_{44} shows the weakest dependence on pressure, and the bulk modulus shows a linear dependence on pressure up to 1 GPa. This linearity is important when developing equations of state for gas hydrates and is consistent with results from our previous work[112]. Very high pressures were considered and throughout the entire range, the hydrate lattice remained elastically stable when considering the pressure-corrected Born stability criteria[39]:

$$C_{44} > 0, \quad C_{11} > |C_{12}|, \quad C_{11} + 2C_{12} > 0 \tag{4.9}$$

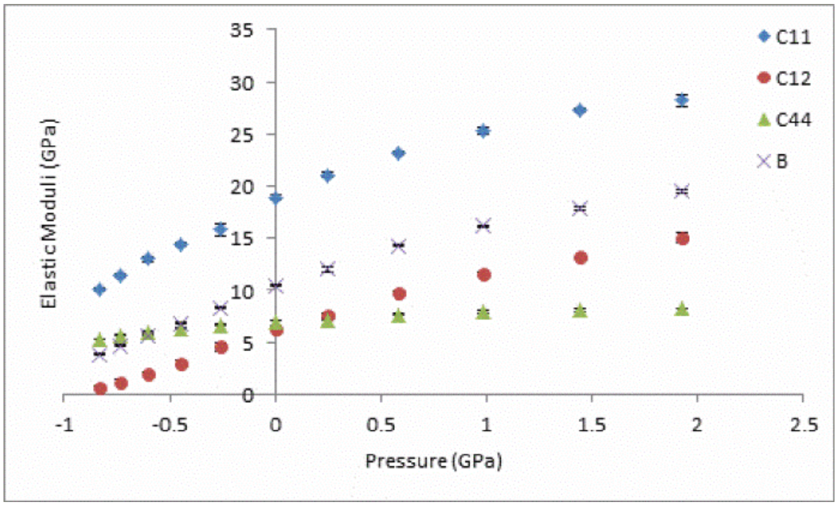

Figure 4-2. Elastic moduli as a function of pressure of methane hydrate.

Moreover, the pressure-corrected Cauchy relation[114,115], $\delta = C_{44} - C_{12} + 2P$, was calculated to evaluate the deviation of interatomic forces from centrality. As Figure 4-3 shows, the Cauchy relation deviates significantly from zero. Even under zero pressure, the deviation is 0.65 GPa; this reveals the importance of many-body interactions when developing or using force fields for gas hydrates. This finding is similar to that of ice I_h in which many-body interactions are known to play a critical role[116] and is expected due to the similarity in the hydrogen bonding network in hydrates and ice[12]. As for the deviation from isotropy, this is quantified using the Zener anisotropy factor[38,114], $A_Z = 2C_{44}/(C_{11} - C_{12})$. As Figure 4-4 shows, the Zener factor is very close to unity which reflects isotropy over a very wide pressure range. This contrasts with the elastic anisotropy of ice I_h which consists of non-planar hexagonal rings stacked over each other unlike gas hydrates which consist of cages in all directions[12]. These conclusions regarding the importance of many-body interactions and the elastically isotropic nature of gas hydrates is consistent with previous experimental work[18] using Brillouin spectroscopy with the same cage occupancy of 100%.

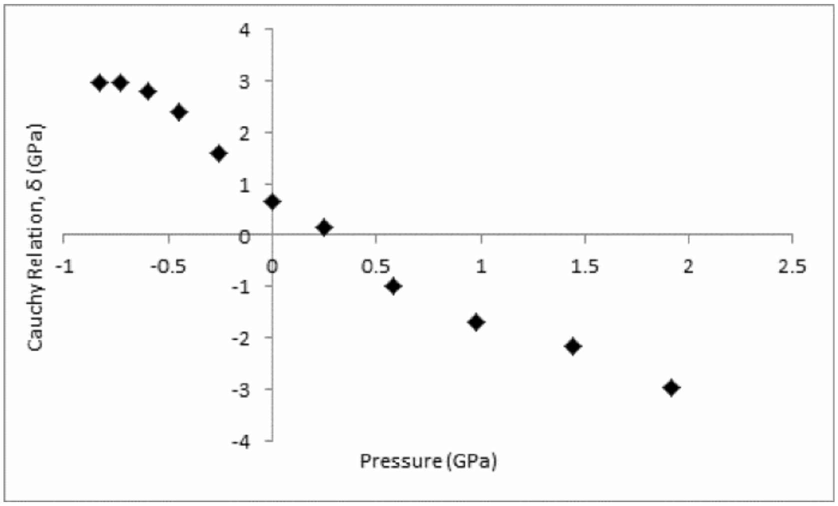

Figure 4-3. Cauchy relation as a function of pressure of methane hydrate.

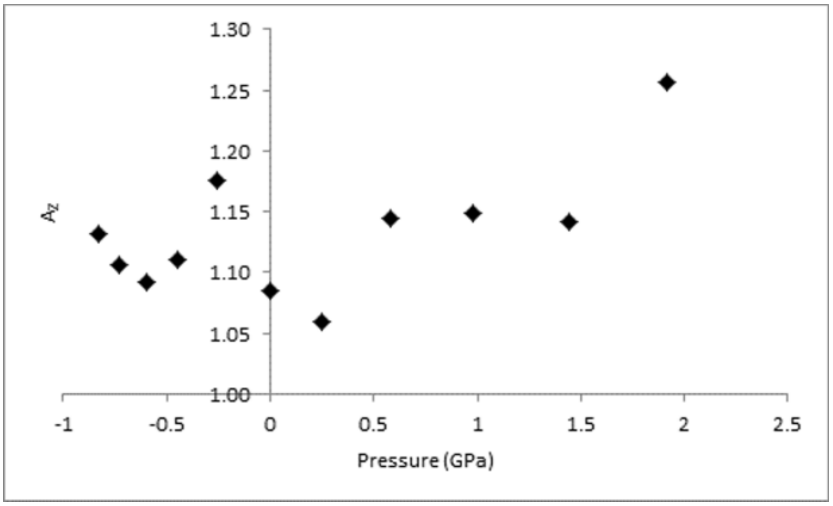

Figure 4-4. Zener anisotropy factor as a function of pressure of methane hydrate.

4.5.2 Heat Capacity at Constant Volume

The heat capacity at constant volume was calculated using the energy derivative, eqn (4.3), and fluctuation formula, eqn (4.4), over a wide temperature and pressure range. The results are shown in Figure 4-5, and a linear fit through the results of eqn (4.3) was used at 273 K. In general, both equations gave similar results for the heat capacity, with variations of maximum 10% for 70% of the cases in which results from both equations are available, despite a few significant variations at very high pressure. In general, it is more challenging to ensure the convergence of the heat capacity using the fluctuation formula since longer simulation times may be required[117,118], but our results show good agreement using both approaches in most cases. Additionally, the heat capacity seems to display weak dependence on temperature and pressure, considering the variation in results obtained using both methods. The linear fit was only done at 273 K since other temperatures show significant scattering from a perfectly linear trend. This scattering is expected for the calculation of heat capacity using molecular dynamics, as reported in other studies[35], and longer simulation times may reduce this scattering. The linear fit along with the coefficient of determination, R^2, was found to be:

$$C_{V,273K} = 0.38P + 2435 \quad \left(-60 \le P \le 370 \text{ MPa}, \mathrm{R}^2 = 0.93\right) \tag{4.10}$$

where the units of C_V and P are $\mathrm{J{\cdot}kg^{-1}{\cdot}K^{-1}}$ and MPa, respectively. According to the above relation, the maximum variation in the heat capacity at constant volume at 273 K over the entire pressure range is only around 6%. Considering this weak dependence on pressure and taking the cases at 250 K and 293 K over the entire pressure range, the average values of heat capacities at these two temperatures vary by only 6% as well.

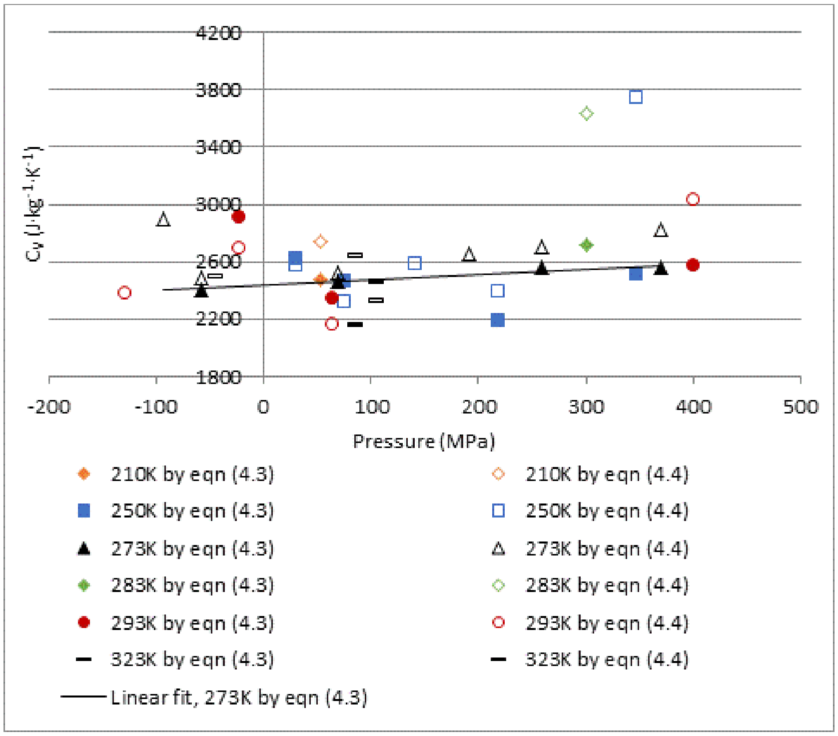

Figure 4-5. Specific heat capacity at constant volume of methane hydrate as a function of temperature and pressure.

4.5.3 Isothermal Compressibility

Isothermal compressibility is an important parameter during phase transitions[121]; therefore, it plays a critical role during production of methane from natural hydrates in a process which typically involves phase change. Isothermal compressibility and bulk modulus were calculated using eqn (4.5), and the results are shown in Figures 4-6 and 4-7. The isothermal compressibility is found to be essentially independent of pressure at 273 and 293 K, but the results at 250 K display a strong dependence. This difference can influence the curvature of the pressure-temperature phase diagram[121]. Physically, this reflects that the hardness of methane hydrate at 250 K varies significantly with pressure going from relatively soft to hard as pressure increases. At low pressures, the inter-atomic forces at 250 K seem to be relatively much weaker than at higher temperatures yielding a much higher compressibility. However, more computational and experimental results are needed to verify the results at 250 K. At 273 K, the results are close to the results of Ning et al.[35], obtained using classical molecular dynamics, but higher by 10%, on average. Up to 200 MPa, the compressibility is higher, as expected, at 293 K compared to 273 K.

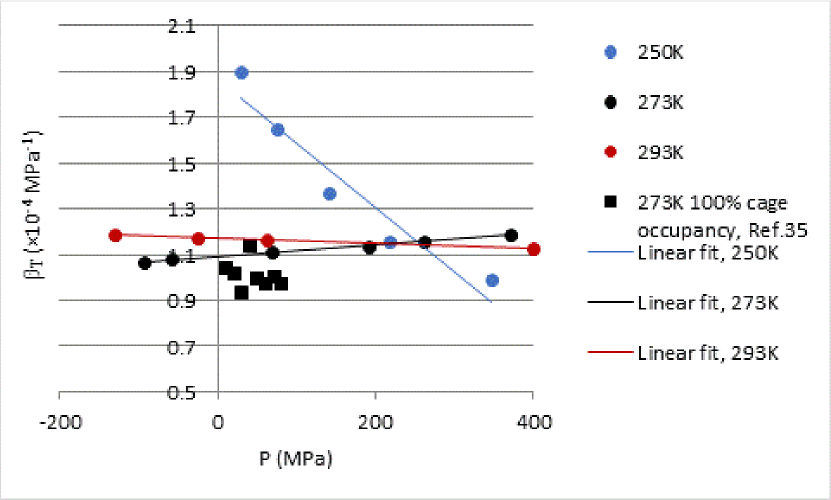

Figure 4-6. Isothermal compressibility of methane hydrate as a function of temperature and pressure.

As for the isothermal bulk modulus shown in Figure 4-7, our results agree with the experimental value of Klapproth et al.[33] within 1%, given that the experimental work involved high cage occupancy of around 98% which is very close to the 100% value considered here. Compared to ice I_h[119,120], methane hydrate has almost the same bulk modulus as ice at low pressures up to 100 MPa. This reflects the dominance of water-water interactions as opposed to water-methane at low pressures, as was found in an earlier work[35], in determining the compressibility. At higher pressures, the guest-host interactions become more influential as shown by the deviation in bulk modulus between methane and ice under high pressure. The linear fits to the isothermal bulk modulus results are as follows:

$$B_{250K} = 0.0154P + 4.98 \quad \left(30 \le P \le 350 \text{ MPa, } \mathrm{R}^2 = 0.99\right)$$
$$B_{273K} = -0.0020P + 9.15 \quad \left(-90 \le P \le 370 \text{ MPa, } \mathrm{R}^2 = 0.99\right)$$
$$B_{293K} = 0.0008P + 8.54 \quad \left(30 \le P \le 350 \text{ MPa, } \mathrm{R}^2 = 0.99\right) \tag{4.11}$$

where the units of B and P are GPa and MPa, respectively.

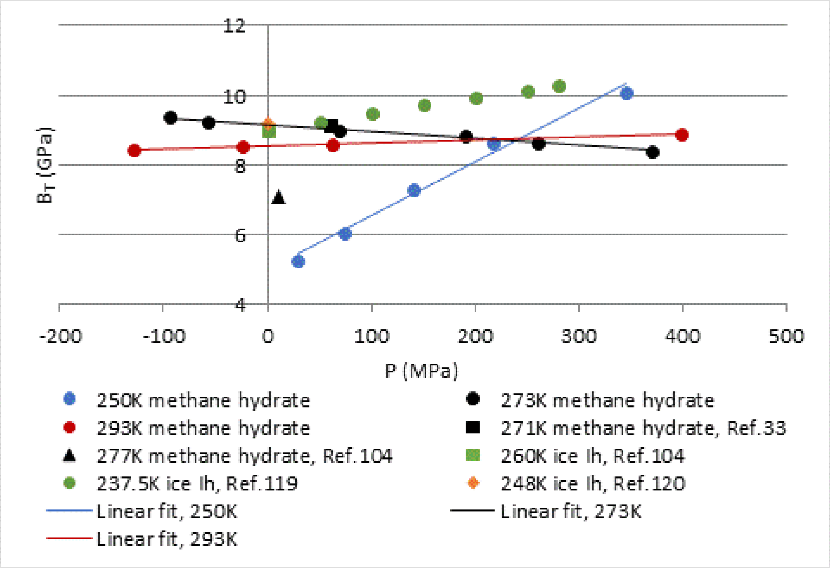

Figure 4-7. Isothermal bulk modulus of methane hydrate and ice I_h.

4.5.4 Thermal Expansion Coefficient

Using the isothermal compressibility, the thermal expansion coefficient was calculated according to eqn (4.6), and the results are shown in Figure 4-8. Compared to the results of Ning et al.[35], our results are almost 40% lower. The dominant factor for this discrepancy is the thermal pressure coefficient, $(\partial P/\partial T)_V$, which is lower than expected at almost all simulated conditions. Additionally, opposite to what is generally believed[12], methane hydrate was found to have a lower thermal expansion coefficient compared to ice I_h[122,123]. However, our previous work[112] has found that methane hydrate has a more rigid internal structure compared to ice in terms of bond angles, and it is known[124] that lower rigidity decreases the thermal expansion coefficient. Other factors can certainly come into play, but this requires further studies over a wide range of conditions to better ascertain differences between hydrates and ice in this regard. This is an important difference between both crystalline structures and should be accounted for in risk assessment studies for natural hydrate production.

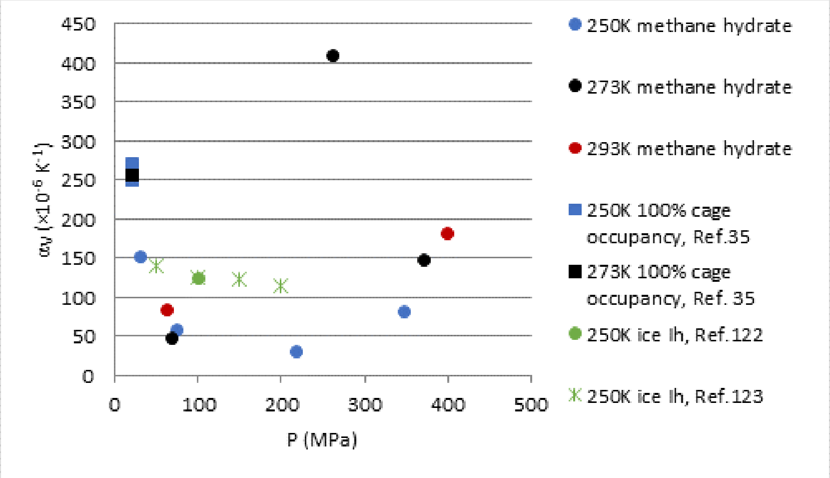

Figure 4-8. Thermal expansion coefficient of methane hydrate and ice I_h as a function of temperature and pressure.

4.5.5 Heat Capacity at Constant Pressure

Heat capacity at constant pressure was calculated using eqn (4.7) with the previously determined properties at three temperatures, and the results are shown in Figure 4-9 along with results from other research groups. The significant disparity in the results reported in the literature for methane hydrate can be clearly observed. Experimental values can vary due to variations in hydrate purity due to residual ice or gas, porosity, and cage occupancy.[35] All of these parameters are difficult to quantify in experiments and can greatly influence the results. Compared to the results of Ning et al.[35] which were obtained using classical molecular dynamics, our heat capacity values are 7% lower, on average. Our results are also closer to the experimental values, especially those of Waite et al.[10] obtained using a needle probe technique and gas hydrates with a high cage occupancy of 97.6%. Compared to ice I_h[123,125], the heat capacity of methane hydrate seems significantly higher. This can be related to the fewer degrees of freedom of motion in ice compared to hydrate as reflected by the mean square displacement as will be discussed in section 4.6. Compared to liquid water, however, the heat capacity of the hydrate is almost 50% lower. This has critical implications on the endothermic hydrate dissociation process and should be accounted for since hydrate-bearing sediments will have much lower heat capacities than water-bearing sediments.[10]

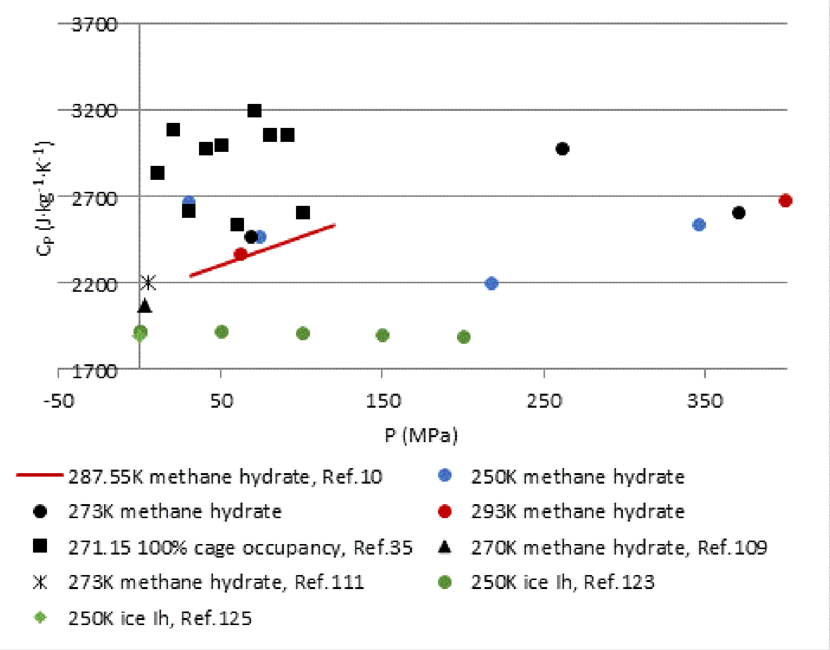

Figure 4-9. Specific heat capacity at constant pressure of methane hydrate and ice I_h as a function of temperature and pressure.

4.5.6 Adiabatic Compressibility

Finally, adiabatic compressibility and bulk modulus were calculated according to eqn (4.8), and the results are shown in Figures 4-10 and 4-11. Adiabatic compressibility is a necessary parameter in the seismic modelling of hydrate-bearing sediments. The general trends and data values are similar to those of isothermal compressibility and bulk modulus as expected[126] for solids, in general. The results at 273 and 293 K agree, generally, with those from other research groups for methane hydrate and are close to the values of ice I_h which again shows the dominance of host-host interactions on compressibility. The results at 250 K are consistently lower than expected with strong pressure dependence. This behaviour requires further confirmation with more simulations and experiments, but constitutes an interesting case for further investigation.

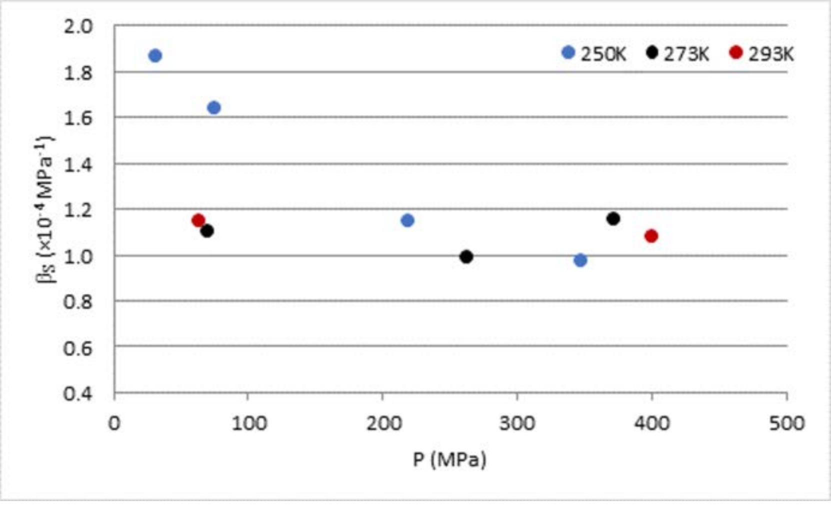

Figure 4-10. Adiabatic compressibility of methane hydrate as a function of temperature and pressure.

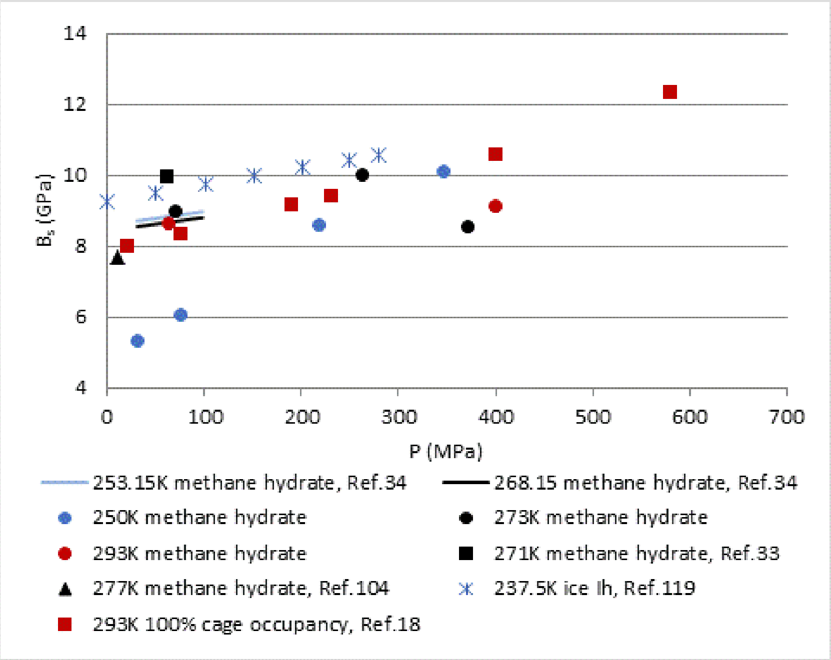

Figure 4-11. Adiabatic bulk modulus of methane hydrate and ice I_h as a function of temperature and pressure.

4.6 Structural Stability

4.6.1 Mean Square Displacement

For simulations over a wide temperature and pressure range as in this work, it is necessary to ensure the lattice is stable through different measures, including the mean square displacement (MSD). In stable solids, the atoms vibrate around lattice sites without displaying diffusive behaviour, and this can be reflected in the MSD, which is defined as:

$$MSD = \frac{1}{N}\sum_{i=1}^{N}\left|\vec{r}_i(t) - \vec{r}_i(0)\right|^2 \tag{4.12}$$

where N is the number of atoms of a particular kind and $\vec{r}_i(t)$ is the position of an atom at time t. The MSD as a function of time should have a plateau with a height that reflects the amplitude of atomic vibrations. To ensure the stability of the water cages in gas hydrates, the MSD of the oxygen atoms was calculated under all considered conditions, and a typical curve is shown in Figure 4-12. The MSD was calculated for the last 10 ps of simulation, and carbon atoms were also considered for comparison. Under all conditions, the water cages were stable as reflected by the plateau exhibited in the MSD of the oxygen atoms. It can also be seen that the methane molecules, which are not part of the complex network of water cages, have greater vibrational freedom as reflected by the larger MSD value which is almost twice that of the oxygen atoms. As for the numeric value of the MSD, the average value obtained for oxygen atoms in the results shown in Figure 4-12 is 0.19 Å^2 which is comparable to the value[127] of 0.34 Å^2 obtained using classical molecular dynamics. Any differences are due to the difference in simulation conditions and theories used in both studies.

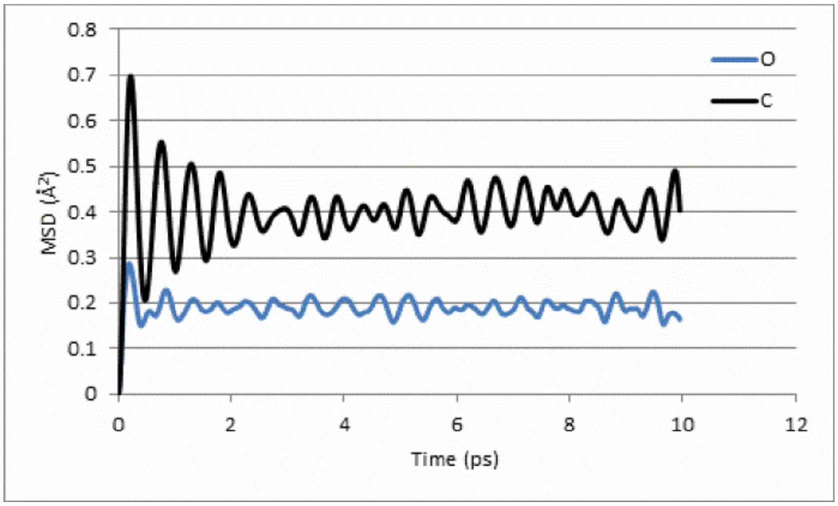

Figure 4-12. Mean square displacement of oxygen and carbon atoms at 293 K and 62 MPa.

Moreover, the MSD can be used to obtain an order-of-magnitude estimate of the elastic modulus of the crystal as follows:[128]

$$G \propto \frac{1}{a} \cdot \frac{k_B T}{MSD} \tag{4.13}$$

where G is an elastic modulus for compression or shear and a is the characteristic dimension of the unit cell. Using a weighted average MSD of 0.22 Å^2 at 293 K and a lattice constant of 12 Å gives an elastic modulus of 1.5 GPa. This is of the same order of magnitude as the elastic moduli of gas hydrates[11] and is very close in value to the shear modulus of 3.2 GPa. This further confirms the MSD values for methane hydrate obtained in this work and links atomic displacements to large-scale continuum elastic properties.

Compared to ice I$_h$, methane hydrate has a much higher MSD value. Specifically, the oxygen atoms in ice exhibit[129,130] an MSD of 0.014-0.044 Å^2 which is almost one order of magnitude lower than that of hydrate. This can partly explain the lower heat capacity of ice compared to hydrate, shown in Figure 4-9. A lower MSD means fewer degrees of freedom to store thermal energy which translates into a lower heat capacity.

4.6.2 Radial Distribution Functions

The radial distribution functions (RDFs) of carbon-oxygen, G_{C-O}, oxygen-oxygen, G_{O-O}, and oxygen-hydrogen of the water molecules, G_{O-H_W}, were evaluated at all conditions averaged over the last 10 ps of simulation, and typical curves are shown in Figure 4-13. The RDF, which reflects the probability of finding an atom at a certain radial distance from another, provides another measure of structural stability. For G_{C-O}, integration up to the minimum of the first peak gives the coordination number of carbon atoms. This was found to be 23 which is also the average number of water molecules forming both the large and small cages in sI hydrate and is consistent with previous results[131]. Therefore at all studied conditions, the water molecules maintained their structure of cages around the methane molecules which reflects stability. Additionally, G_{C-O} shows a void at small distances and a cavity wall at around 4 Å as reflected by the peak which further proves the stability of the cages. As for G_{O-O}, this can be used to infer the arrangement of the water molecules. Integration up to the minimum of the first peak gives a coordination number of 4 which is consistent with the expected tetrahedral arrangement of water molecules. Furthermore, the tetrahedral arrangement is also confirmed by the positions of the first two peaks in G_{O-O}. These were found to be 2.7 and 4.5 Å which is the same as that of water[132] at ambient conditions and agrees with previous work[133] using classical molecular dynamics. Lastly, the first two peaks in G_{O-H_W} depict covalent and hydrogen bonding interactions, respectively. As expected for hydrate, the two peaks occur at around 1.0 and 1.7 Å. Figure 4-13 shows G_{O-H_W} at two different pressures in which the two bond types display opposite behaviour. As pressure decreases, the hydrogen bond strength decreases, as reflected by the lower and broader second peak, to comply with the expansion, and the covalent bond strength increases as reflected by the sharper and higher first peak, to counteract the expansion. This opposite behaviour has been identified earlier[96] for hydrogen-bonded networks, and our previous work[112] on methane hydrate and ice I_h reached the same conclusion.

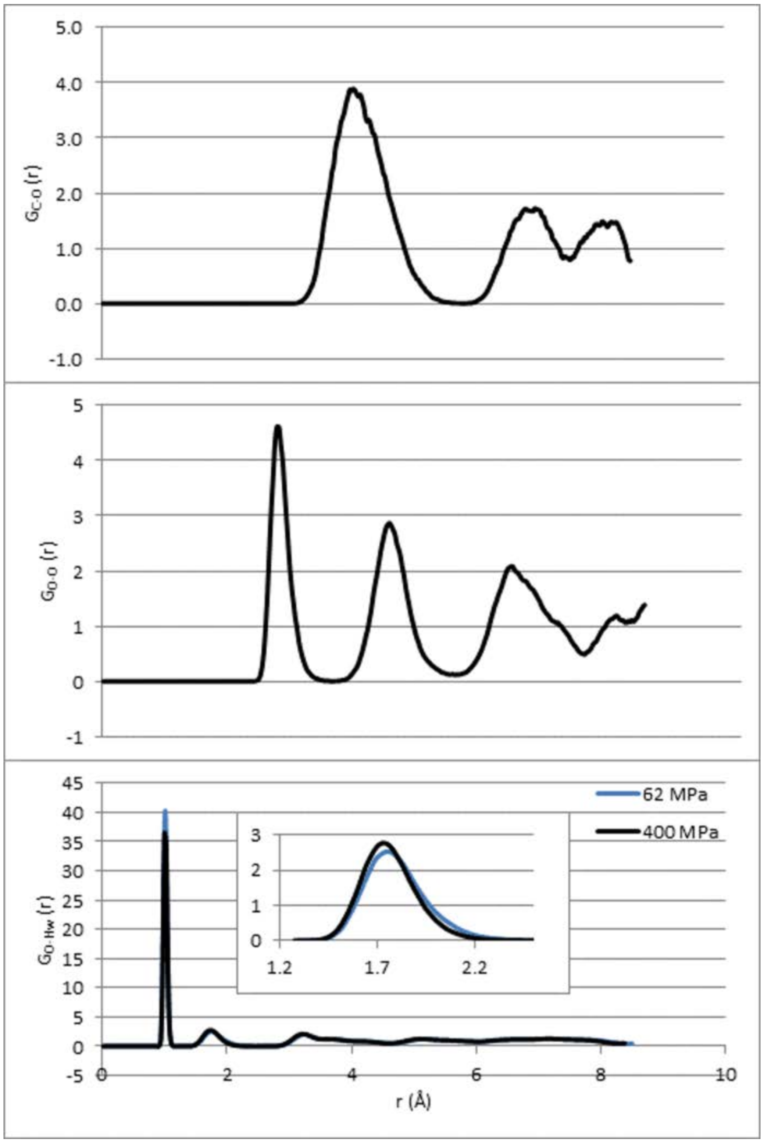

Figure 4-13. Radial Distribution functions of methane hydrate at 293 K.

4.7 Conclusions

A wide range of thermophysical properties have been determined for methane hydrate using *ab initio* simulations. Specifically, second-order elastic constants, heat capacity, compressibility, and thermal expansion coefficients have been calculated over a wide range of conditions. The structures were ensured to be stable using the mean square displacement and radial distribution function measures.

Molecular statics were used to determine the pressure dependence of the second-order elastic constants. The bulk modulus was found to vary linearly with pressure up to 1 GPa, and the hydrate was found to be elastically isotropic. Multi-body interactions were found to play an important role in hydrates and should be accounted for in classical force fields.

Molecular dynamics were used to calculate the other properties. In general, most results agree well with experimental values and other theoretical calculations except for the thermal expansion coefficient. Up to 100 MPa, the water-water interactions were found to dominantly influence compressibility. Also, the thermal expansion coefficient was found significantly lower than literature values and lower than ice I_h values which can be related to the lower rigidity of the hydrate compared to ice, but it still needs further confirmation with more simulations and experimental values. The heat capacity, however, was much higher than that of ice.

Under all conditions the hydrate lattice was stable and exhibited the expected mean square displacement behaviour and radial distribution functions. The mean square displacement was found almost an order of magnitude higher than that of ice which helps explain the higher heat capacity of hydrate compared to ice. Also, the mean square displacement provided a very good rough estimate of the elastic modulus of hydrates. Finally, the radial distribution functions correctly reflected the cage structure of hydrates with the correct radius, coordination numbers, and hydrogen and covalent bonding behaviour.

For future work, it is recommended to compare the results in this work with other *ab initio* results. Specifically, a larger system with different cage occupancies is worth investigation. Such a system may help in understanding the differences in results between simulations and experiments and will provide significant insights.

5 Core Structure and Peierls Stress of Linear Defects in Methane Hydrate

5.1 Preface

In this chapter, the modelling approach is shifted to plastic deformation at the microscale with classical force fields. It builds on the elastic deformation properties studied in the previous chapters. The core structure and Peierls stress, or the shear stress required to move a dislocation one lattice unit at zero temperature, are studied for edge and screw dislocations. This study constitutes the starting point for future studies on individual dislocations in gas hydrates under relevant conditions.

5.2 Summary

Gas hydrates are at the center of current materials research due to their critical importance to the environment and energy supply and further progress requires knowledge of their mechanical properties for mono- and poly-crystalline states. In this chapter we focus on the former, using molecular statics taking into account couplings between crystal symmetry and chemical composition. Specifically, the core structure and Peierls stress of edge and screw dislocations in methane hydrate were determined as a function of composition and pressure using atomic simulations. A coarse-grained potential was used, and the $[100](010)$ slip system was considered. The edge dislocation had a much lower Peierls stress and stronger dependence on methane composition and pressure compared to screw dislocation. Both dislocations, however, exhibited wide spreading and dissociation at different stages of deformation. The Peierls-Nabarro model was found to greatly underestimate the Peierls stress for screw dislocation. The dislocation modelling presented in this work partially fills a gap in the much needed, yet less

researched and understood, field of plastic deformation in gas hydrates for energy recovery applications.

5.3 Introduction

Gas hydrates have recently been the center of much research due to their critical applications. They exist in nature mainly as methane hydrates in permafrost regions and deep ocean sites, and it is estimated that they host an energy content that is twice that of all other fossil fuels combined.[2] Several countries have already started work to harness this resource with Japan expecting to be ready for commercial mass production by 2018.[3] In terms of their material structure, they are polycrystalline compounds that consist of cages of hydrogen-bonded water molecules which entrap guest gas molecules. Gas hydrates can take on different crystal structures with a variety of guest molecules like argon, methane, carbon dioxide, propane, and butane, among others.

While considered a promising alternative energy resource, natural gas hydrates are also important factors in studies of climate change and stability of Earth strata. If not well investigated, disruption of geological formations hosting gas hydrates can lead to potentially disastrous landslides and the seepage of methane gas into the atmosphere, which contributes to global warming.[11] For risk assessment studies concerned with these implications, the mechanical properties of gas hydrates are of paramount importance. The strength and deformation mechanism of hydrate crystals in terms of defects should be thoroughly studied along with their interaction with the earth sedimentary layers. Currently, there are very few studies on the mechanical deformation of pure methane hydrates. Few experimental studies compare the strength of polycrystalline hydrates and ice and lump the effects of different defects in the polycrystalline hydrate into a single dislocation flow model.[9,21] No studies have been done yet on the atomic structure and deformation mechanism of individual dislocations to reveal the mechanism of dislocation motion.

Due to the significant lack of studies on individual dislocations and as a continuation of our previous work[112] on the elastic deformation of methane hydrates, this work aims to study the plastic deformation of methane hydrates and the core structure of individual dislocations using classical molecular statics. Specifically, the Peierls stress, defined as the minimum stress required to make a straight dislocation move at zero temperature[45], is quantified for edge and screw dislocations. While an ideal concept, the Peierls stress is an important parameter in crystal deformation.[134] Specifically, the Peierls stress helps in quantifying the lattice resistance to dislocation motion and can be related to the yield stress at very low temperatures. Additionally, it is the most important property for describing the mechanism of dislocation motion which can be either through thermally assisted kink pairs or viscous drag, depending on whether the applied stress is below or above the Peierls stress.

The organization of this paper is as follows. Section 5.4 presents the computational methodology; section 5.5 presents the simulation results and discussion for edge and screw dislocations; section 5.6 summarizes the key conclusions.

5.4 Computational Methodology

The most common structure of methane hydrate in nature is the cubic sI structure. The primitive lattice unit consists of two 5^{12} cages, of 12 pentagonal faces, and six $5^{12}6^{2}$ cages, of 12 pentagonal and 2 hexagonal faces, with a total of 46 water molecules.[12] The positions of the water molecules that form the cages and the methane molecules inside the cages were based on experimental high-resolution, neutron diffraction data for deuterated methane hydrate.[55] The considered cage occupancies were 0, 80, and 100% with a maximum of one methane molecule per cage. For the 80% cage occupancy, the methane molecules were randomly assigned to the cages.

All simulations were performed using the LAMMPS package[135] with a coarse-grained potential. The considered potential takes on the Stillinger-Weber form[136] , as follows:

$$
\begin{aligned}
E &= \sum_{i}\sum_{j>i}\phi_2\left(r_{ij}\right)+\sum_{i}\sum_{j\neq i}\sum_{k>j}\phi_3\left(r_{ij},r_{ik},\theta_{ijk}\right)\\
\phi_2\left(r_{ij}\right) &= A\varepsilon\left[B\left(\frac{\sigma}{r_{ij}}\right)^4-1\right]\exp\left(\frac{\sigma}{r_{ij}-a\sigma}\right) \qquad (5.1)\\
\phi_3\left(r_{ij},r_{ik},\theta_{ijk}\right) &= \lambda\varepsilon\left[\cos\theta_{ijk}-\cos\theta_o\right]^2\exp\left(\frac{\gamma\sigma}{r_{ij}-a\sigma}\right)\exp\left(\frac{\gamma\sigma}{r_{ik}-a\sigma}\right)
\end{aligned}
$$

where r_{ij} is the distance between particles i and j and θ_{ijk} is the angle between the vectors created by the positions of the pairs of particles $i-j$ and $i-k$; ϕ_2 and ϕ_3 represent the two-body and three-body interaction terms, respectively. Hydrogen bonding is accounted for using the three-body term which penalizes configurations of water molecules that deviate from the perfect tetrahedral configuration of $\theta_o = 109.5^o$, with the tetrahedral interaction strength determined by λ. The other constants scale the potential and are summarized in Table 5-1. The cut-off distance for all interactions inherent in the potential is $a\sigma$. It should be noted that Ref. 136 provides a set of water-methane interaction parameters, and the ones used here provided the best agreement of the lattice parameter with experimental results[33]. The considered coarse-grained potential is highly efficient since it does not account for individual atoms; instead, each water or methane molecule is considered a single particle. It has been successful in predicting many thermodynamic and structural properties of water and hydrates such as melting temperature, enthalpies of phase change, and surface tension, among many others.[136] It has also been used in recent studies of gas hydrate nucleation.[16,137,138] Apart from this, our previous work[139] has revealed the importance of multi-body interactions, like the ones considered in this potential, in modelling gas hydrates. A stress-strain analysis[140] was used initially in this work to test how well the model can predict second-order elastic constants of methane hydrate with 100% cage occupancy under zero pressure. The calculated elastic constants were $C_{11} = 12.54$ GPa, $C_{12} = 4.65$ GPa, and $C_{44} = 4.10$ GPa which compare very well with the experimental values[18] of $C_{11} = 11.9$ GPa, $C_{12} = 6.3$ GPa, and $C_{44} = 3.4$ GPa, considering the larger variations from experimental values in previous results obtained from *ab initio* simulations[36,84].

Table 5-1. Interaction parameters of adopted potential, eqn (5.1), with $A = 7.049556277$, $B = 0.6022245584$, $\gamma = 1.2$, and $a = 1.8$.[136]

	ε (kcal/mol)	σ (Å)	λ
Water	6.189	2.3925	23.15
Methane	0.340	4.08	0
Water-methane	0.3	4.05	0

All simulations involved a single dislocation at the center of the supercell, and a two-dimensional depiction of a typical simulation box is shown in Figure 5-1. The crystal is oriented with the x-axis, y-axis, and z-axis aligned with $[100]$, $[010]$, and $[001]$ lattice directions, respectively. The simulation box is periodic in the x and z directions, and atomic layers at the top and bottom along the y direction are fixed to apply the strain. The initial configuration of screw dislocations also involved fixed atomic planes at the top and bottom to give the effect of an infinite array of a perfect crystal. However, for edge dislocations, this initial boundary condition did not converge well once shear stresses were applied; therefore, the simulation started with two free surfaces along the y direction before applying the strain. This may be due to the more complex stress field[45] of edge dislocations compared to screw and the complex cage network of hydrates which further adds residual strains to the system which can be resolved with free surfaces. Nevertheless, this is not expected to affect the results due to the very large system size and the fact that the core structure before any shear stresses were applied using either boundary condition along the y direction was the same. Our previous work[112] has found that different slip systems in methane hydrate are equivalent; therefore, we consider here only the simple $[100](010)$ slip system with the magnitude of the Burgers vector, b, equal to the lattice constant. For edge dislocations, the supercell has a thickness of $2b$ along the z axis. An edge dislocation is introduced by joining two crystals along their $x-z$ faces with one having one fewer atomic plane in the x direction.[134] The sizes of each of the crystals along the x direction and the atomic positions are adjusted such that both have a length equal to an average of their sizes in that direction before any adjustment. As for screw dislocations, these are introduced into the perfect supercell by displacing the x components of the particles according to the isotropic elastic solution of the displacement field[134]:

$$u_x(y,z)=b\frac{\theta}{2\pi} \tag{5.2}$$

where u_x is the x component of the displacement vector and θ, which ranges from $-\pi$ to π, is the angle between the z axis and the vector connecting the origin to $(0,y,z)$. The supercell thickness along the x axis for screw dislocation is $2b$, and the supercell vector along the z axis is given a component of $b/2$ along the x axis to ensure periodic boundary conditions in that direction[141].

The hydrostatic pressure of the system is set by the specified lattice constants. This is determined using fitting of pressure-volume data points of perfect crystals. Perfect supercells of $2\times2\times2$ unit cells, for 0 and 100% cage occupancy, and $3\times3\times3$ unit cells, for 80% cage occupancy, were allowed to relax at different pressures, P, or lattice constants, a, and the results were fitted according to Murnaghan's equation of state[69]:

$$P(V)=\frac{B_o}{B_o^{'}}\left[\left(\frac{V}{V_o}\right)^{-B_o^{'}}-1\right] \tag{5.3}$$

Where V is the supercell volume, B is the bulk modulus, $B^{'}$ is the derivative of the bulk modulus with respect to pressure, and the subscript denotes zero pressure conditions. The above equation was used to determine the lattice constant at different pressures using the fitting parameters summarized in Table 5-2.

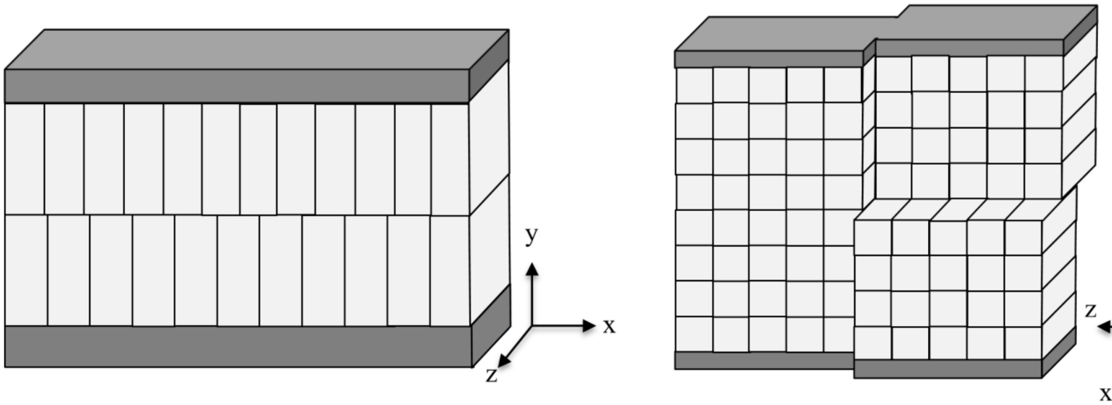

Figure 5-1. Supercell configuration of edge, left, and screw, right, dislocations with the shaded areas being empty signifying periodicity along the x and z axes only.

Table 5-2. Fitting parameters of Murnaghan's equation of state at different cage occupancies, where a_o is the lattice constant under zero pressure determined from V_o.

	B_o (GPa)	$B_o^{'}$	a_o (Å)
100% cage occupancy	7.280	2.630	11.7038
80% cage occupancy	7.274	2.790	11.6877
0% cage occupancy	7.301	2.875	11.6006

Simulations of dislocations involved molecular statics at constant volume. The positions of the molecules were allowed to relax using a conjugate-gradient algorithm in the initial supercell configuration, and then shear stresses were applied incrementally with relaxation after each shear step. The relaxation criterion was 0.005 kcal·mol^{-1}·Å^{-1}, and shear strains were applied in increments of 0.01%. The supercell sizes were $64 \times 64 \times 2$ unit cells with around 400,000 molecules which ensured convergence of results. Shear stresses at each shear configuration were determined from the derivative of the total energy with respect to the shear strain relative to that configuration. For each primitive lattice unit in the supercell, the average position of the water molecules was computed to quantify lattice positions which were in turn used to compute the disregistry function, g, of dislocations along the slip plane. Water molecules were used in order to compare the results of different cage occupancies. The disregistry is a measure of the deviation of atomic positions from their perfect lattice sites, and the derivative of the disregistry reflects the density of the Burgers vector. Both the disregistry and its derivative were used to quantify the Peierls stress, or the stress at which the dislocation moves one lattice unit. The disregistry data points were fitted into a sum of N $\tan^{-1}$ functions for the N partial dislocations[46]:

$$g(x) = \frac{b}{2} + \frac{b}{\pi} \sum_{i=1}^{N} \alpha_i \tan^{-1}\left(\frac{x - x_i}{\zeta_i} \right) \tag{5.4}$$

where x_i and ζ_i are the position of the center and the half-width of the i^{th} partial dislocation, and α_i is a scaling parameter. The derivative of the disregistry function was computed analytically from eqn (5.4).

5.5 Results and Discussion

The core structure of edge and screw dislocations and the pressure dependence of the Peierls stress are discussed below. All structural visualizations in this work have been done using UCSF Chimera[142].

5.5.1 Edge Dislocation

The core structure of edge dislocation in methane hydrate is visualized in Figure 5-2, and its disregistry functions are shown in Figures 5-3 to 5-5, for different cage occupancies. The edge dislocation was found to exhibit wide spreading, and dissociation was expected. Figure 5-2 shows the wide spreading of the dislocation and its planar nature. The results of the relevant fitting parameters of eqn (5.4) are shown in Table 5-3 for different cage occupancies.

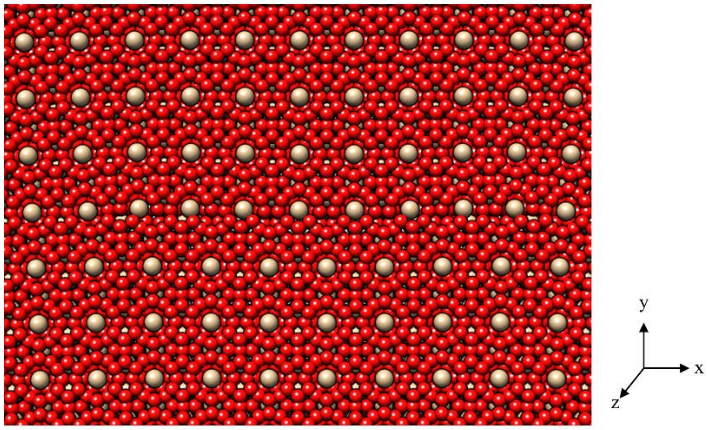

Figure 5-2. Core structure of edge dislocation in methane hydrate with 100% cage occupancy under zero hydrostatic pressure in which red and grey spheres represent water and methane molecules, respectively.

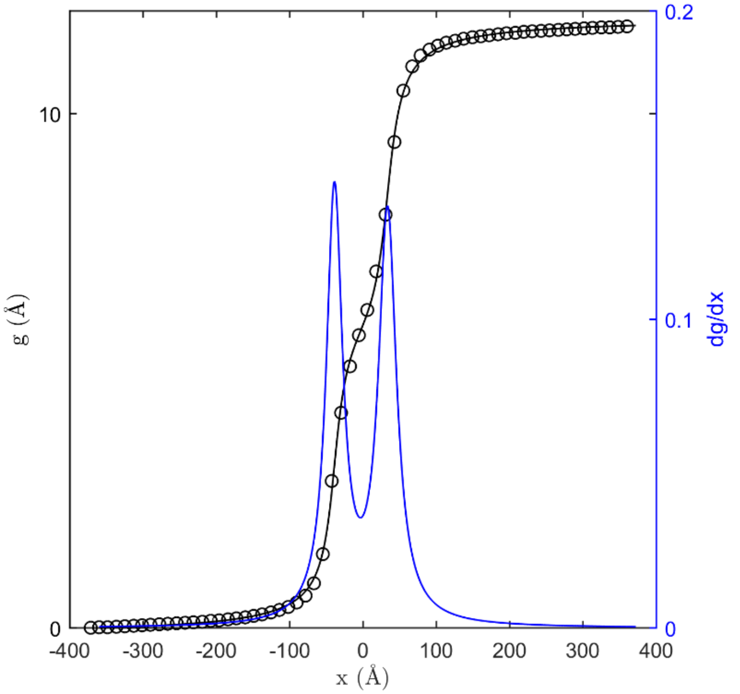

Figure 5-3. Disregistry functions in edge dislocation with 100% cage occupancy under zero hydrostatic pressure (see eqn (5.4)).

Edge dislocations were found to exhibit dissociation into asymmetric partials. The dissociation is expected due to the very wide spreading of the dislocation which is at least 17 times the lattice constant, or the magnitude of the Burgers vector. The spreading increases with a decrease in cage occupancy which coincides with dissociation into more partials. Greater spreading makes the glide of dislocations easier. Therefore, the methane molecules in the cages seem to hinder the motion of dislocations by increasing the friction between lattices due to their repulsive interaction with water molecules.

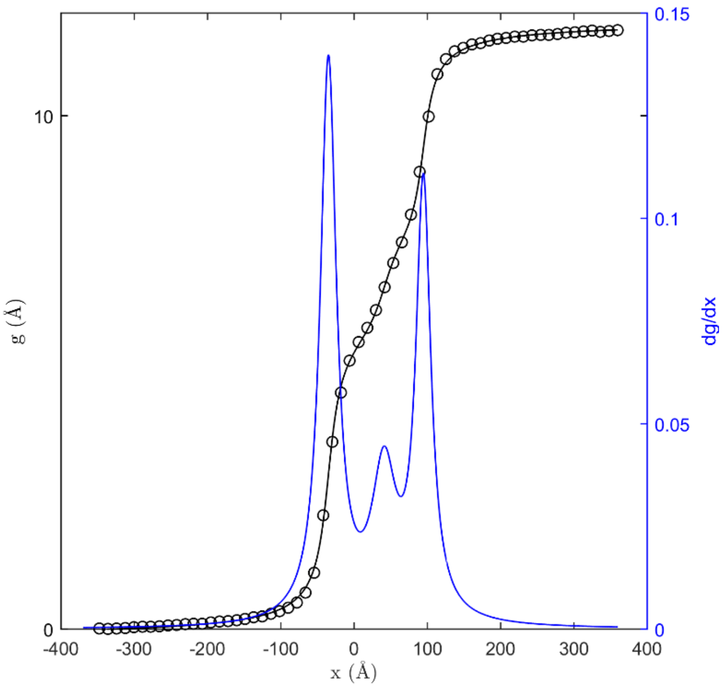

Figure 5-4. Disregistry functions in edge dislocation with 80% cage occupancy under zero hydrostatic pressure.

The easiness of dislocation glide as a function of cage occupancy is further reflected in the magnitude of the Peierls stress, σ_P, summarized in Table 5-3. By decreasing the cage occupancy from 100 to 0%, the Peierls stress decreases by more than 60% making glide of dislocations much easier. The strong dependence of the Peierls stress on composition in edge dislocations may be related to the stresses involved in this case. Edge dislocations introduce tensile, compressive, and shear stresses into the lattice, and our previous work[112] has found that methane hydrate has very different stress-strain behavior under tension and compression with the influence of the methane molecules on stability being more pronounced under compression. Thus, cage occupancy is expected to greatly influence the motion of edge dislocations since part of the crystal is under compressive stresses and the effect of the guest methane molecules is substantial under these conditions. In order to put the Peierls stress into perspective, it is useful to compare it to the ideal shear strength, σ_I, and the shear modulus, G. It is known that real crystals with dislocations can deform at stresses as low as five orders of magnitude lower than their ideal shear strengths.[42] The ideal strength is defined as the stress at the elastic instability of a perfect crystal. Using our previously calculated value[112] of ideal shear strength for 100% cage occupancy, $\sigma_P = 0.0069\sigma_I$. Thus, edge dislocations make the deformation of crystals easier by more than two orders of magnitude. According to the Peierls-Nabarro model, the Peierls stress is directly proportional to the shear modulus and is usually reported as a fraction of it. For 100% cage occupancy and using the experimental value[34] of the shear modulus of methane hydrate yields $\sigma_P = 0.0031G$. In comparison with ice, the Peierls stress for edge dislocations on the basal plane and for prismatic dislocations is $0.11G$ and $0.013G$[143], respectively, given that the shear modulus of ice and hydrate is almost the same. Thus, methane hydrates seem to have a Peierls stress that is one or two orders of magnitude lower than that of ice.

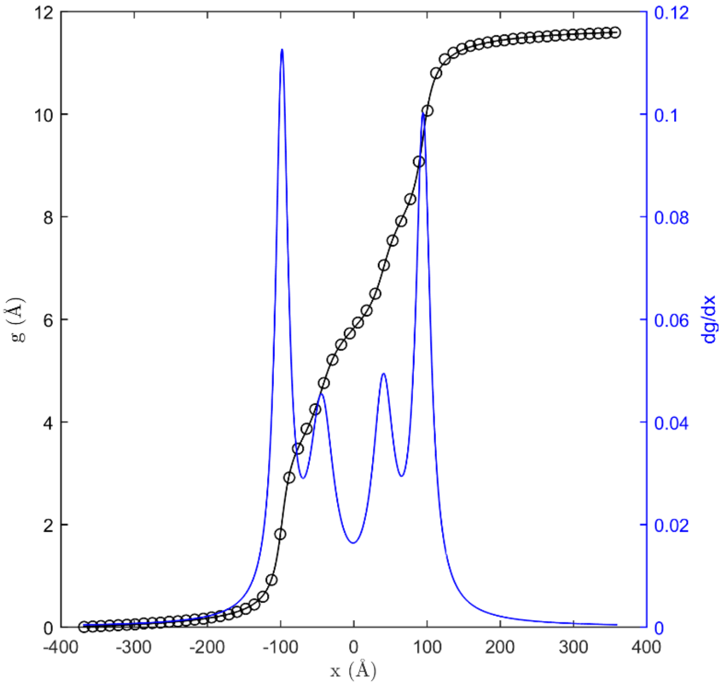

Figure 5-5. Disregistry functions in edge dislocation with 0% cage occupancy under zero hydrostatic pressure.

Table 5-3. Fitting parameters of the disregistry function of edge dislocation under zero hydrostatic pressure, where N is the number of partial dislocations, ζ_i is the half-width of the i^{th} partial dislocation, Δx_i is the distance between adjacent partial dislocations, and σ_P is the Peierls stress.

	N	ζ_i (Å)	Δx_i (Å)	σ_P (MPa)
100% cage occupancy	2	14.9 13.3	72.4	11
80% cage occupancy	3	12.2 20.2 13.3	53.7 75.9	6
0% cage occupancy	4	11.9 17.7 20.3 10.4	54.3 84.1 54.3	4

It is interesting to note how partial edge dislocations move in gas hydrates. For this purpose, the case of 100% cage occupancy is considered, and the derivative of the disregistry function is shown in Figure 5-6 throughout the process. Upon application of a shear stress and as the Peierls stress is approached, the first partial dislocation with a higher density of the Burgers vector, or higher peak in Figure 5-6, moves one lattice constant in the direction of the second partial dislocation, which remains immobile over high stress values. As higher stresses are applied, the separation between the partial dislocations decreases while they maintain an almost constant width. At 159 MPa, which is more than 14 times the Peierls stress, the second partial dislocation moves one lattice constant. This is a significant difference in the motion of the two partials which is due to their asymmetry, and it is worthwhile to explore how the movement of dislocations might change if shear stress in the opposite direction is applied.

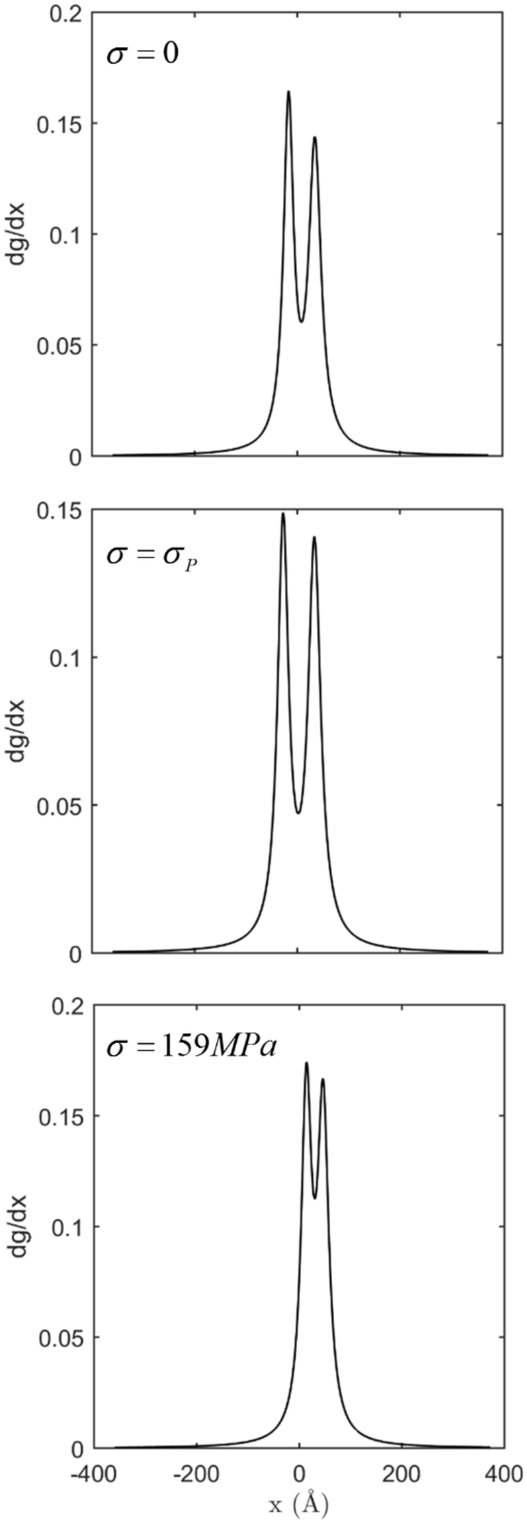

Figure 5-6. Motion of edge dislocation as a function of shear stress with 100% cage occupancy under zero hydrostatic pressure.

5.5.2 Screw Dislocation

The core structure of screw dislocation in methane hydrate is visualized in Figure 5-7, and its disregistry function is shown in Figure 5-8 for the 100% cage occupancy case only since other occupancies exhibited the same general features. Unlike edge dislocations, screw dislocations were found to exhibit a relatively narrow spreading without dissociation initially. Specifically, the dislocation spreads to around 9 times the magnitude of the Burgers vector over a single dislocation; therefore, the disregistry function was fitted into a single $\tan^{-1}$ function according to eqn (5.4), and the relevant results are summarized in Table 5-4. The dislocation displayed planar spreading like edge dislocation. Also, the cage occupancy seems to have a much lower impact on screw dislocations compared to edge dislocations. The spreading and half-width of screw dislocations remains almost the same at 100 and 0% cage occupancies. This reflects that the overall structure of cages hinders the motion of screw dislocations more than the friction caused by methane inside the cages. This may be due to the more three-dimensional nature of screw dislocations, compared to the more two-dimensional edge dislocations, which requires more structural rearrangements of the cages for the dislocations to move. Additionally, unlike edge dislocations with compressive and tensile internal stresses, the screw dislocation introduces only shear stresses which may be less influenced by methane composition.

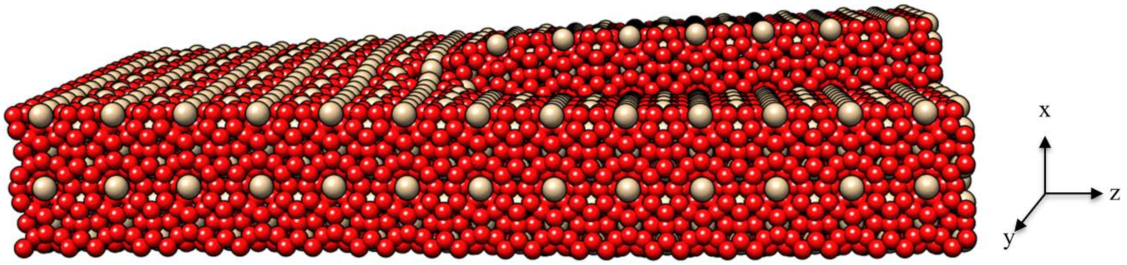

Figure 5-7. Core structure of screw dislocation in methane hydrate with 100% cage occupancy under zero hydrostatic pressure in which red and grey spheres represent water and methane molecules, respectively.

The smaller effect of cage occupancy on the easiness of screw dislocation glide is further reflected in the magnitude of the Peierls stress, σ_P. The Peierls stress varies very slightly with cage occupancy, and drops by only 4 and 40% with a 20 and 100% decrease in cage occupancy, respectively. Compared to the ideal shear strength and shear modulus at 100% cage occupancy, $\sigma_P = 0.28\sigma_I$ and $\sigma_P = 0.13G$. Thus, screw dislocations allow gas hydrates to deform almost 4 times easier than their perfect crystals. Additionally, the Peierls stress of screw dislocations is comparable to that of ice on the basal plane which is $0.32G$ [143]. This further shows the small effect on screw dislocations of methane composition compared to the water structure which forms tetrahedral arrangements in both ice and gas hydrate.

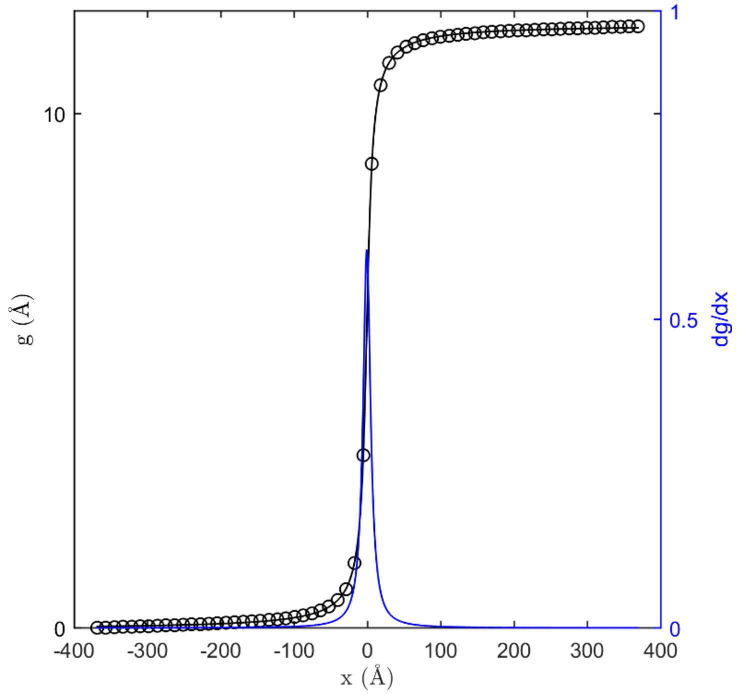

Figure 5-8. Disregistry functions in screw dislocation with 100% cage occupancy under zero hydrostatic pressure.

Table 5-4. Fitting parameters of the disregistry function of screw dislocation under zero hydrostatic pressure, where ζ is the half-width and σ_P is the Peierls stress.

	ζ (Å)	σ_P (MPa)
100% cage occupancy	6.1	449
80% cage occupancy	6.1	431
0% cage occupancy	5.9	276

As for the motion of screw dislocations, this is summarized in Figure 5-9 using the derivative of the disregistry function for the case of 100% cage occupancy but applies for other occupancies. While screw dislocations exhibit no dissociation under zero stress, the dislocation still spreads over a large distance of 9 lattice constants, and dissociation is expected. As shear stress is applied, the dislocation maintains its integrity up to 440 MPa at which it dissociates into two partials. However, the partials are highly asymmetric and not as prominent as the ones in edge dislocation probably due to the much smaller spreading of the screw dislocation. With slightly higher stress or at the Peierls stress, only one of the partial dislocations, the one with the lower peak or Burgers vector density, moves one lattice constant. Again, this case should be compared with one in which shear stress is applied in the opposite direction.

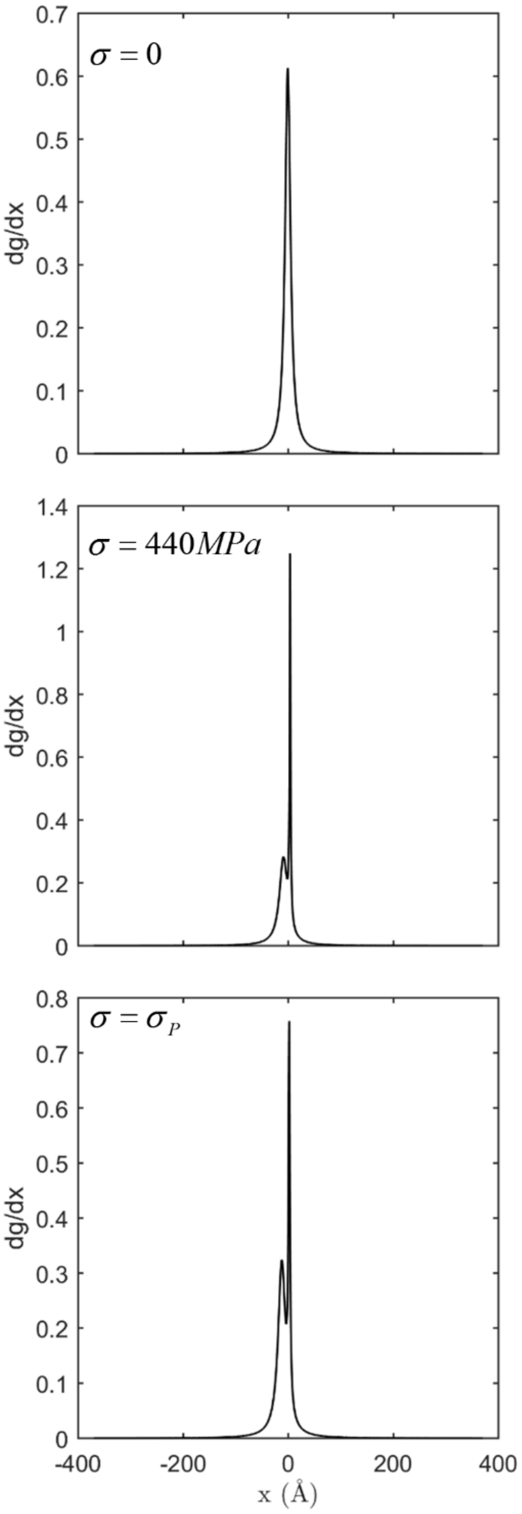

Figure 5-9. Motion of screw dislocation as a function of shear stress with 100% cage occupancy under zero hydrostatic pressure.

Due to their much higher Peierls stress, screw dislocations appear to be the key factors in the motion of linear defects in gas hydrates, and their observed Peierls stress can be compared to that predicted by one of the earliest dislocation models. According to the Peierls-Nabarro model[45], the Peierls stress in a screw dislocation is:

$$\sigma_P = \frac{2G}{1-v}\exp\left(-\frac{4\pi\zeta}{b}\right) \tag{5.5}$$

where v is Poisson ratio. For 100% cage occupancy, the Peierls-Nabarro model greatly underestimates the Peierls stress at 15 MPa, compared to 449 MPa obtained from simulations in this work. This big difference in the value of Peierls stress is expected since the Peierls-Nabarro model involves unrealistic smoothing out of the lattice discreteness near the dislocation core. Also, dissociation of the atomic core of the screw dislocation was observed in the simulations while the Peierls-Nabarro model assumes that the displacement profile undergoes a rigid shift when the dislocation moves without accounting for changes in the displacement profile. Thus, for gas hydrates the discrete nature and changes of the core structure throughout the deformation should be accounted for in any model.

5.5.3 Peierls Stress as a Function of Pressure

Finally, the Peierls stress was computed as a function of pressure for the 100% cage occupancy case in edge and screw dislocations. The results are shown in Figure 5-10. For screw dislocations, the Peierls stress shows weak dependence for the entire pressure range up to 500 MPa. The maximum variation from the initial value under zero pressure is only 20%. For edge dislocations, on the other hand, the Peierls stress shows very strong dependence on pressure probably due to its asymmetric core structure of partial dislocations. Over the entire pressure range, the Peierls stress for screw dislocation remains higher than that for edge dislocation as expected, but the difference decreases, in general, as pressure increases.

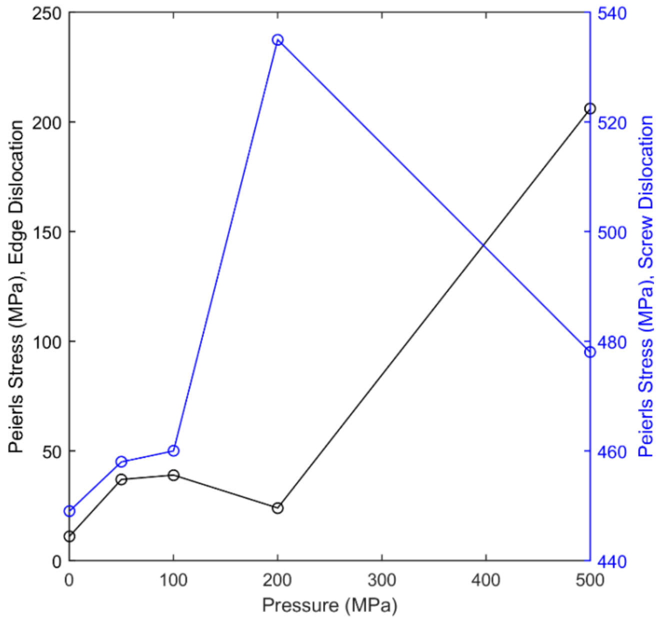

Figure 5-10. Peierls stress as a function of hydrostatic pressure for edge and screw dislocations.

5.6 Conclusions

The core structure and Peierls stress for edge and screw dislocations have been determined as a function of methane composition and pressure for the $[100](010)$ slip system in methane hydrates. Both dislocations exhibited wide spreading and dissociation at different stresses during deformation. While the edge dislocation had much higher mobility compared to the screw dislocation as reflected in its Peierls stress, it also displayed much stronger dependence on methane composition. This may be due to the compressive stresses involved in edge dislocations which allow the effect of cage occupancy to be more evident than in screw dislocations with pure shear stresses. The Peierls-Nabarro model greatly underestimated the Peierls stress for the screw dislocation since it does not properly account for the discrete and evolving nature of the core structure. Also, the edge dislocation had a much stronger dependence on hydrostatic pressure which may be due to the asymmetry of its partial dislocations.

The work presented here provides the starting platform for the future modelling of plastic deformation in gas hydrates. Other force fields than the coarse-grained one should be considered for comparison. While the results here involve molecular statics, there is a need for developing dynamic dislocation flow models for gas hydrates.

6 Conclusions and Contributions to Original Knowledge

6.1 Conclusions

Despite the emerging importance of gas hydrates in many applications, an accurate and detailed characterization of their mechanical and thermal properties remains a much less researched field. Mechanical and thermal properties are critical parameters in the recovery of natural gas hydrates as alternative energy resources, the usage of natural gas hydrates for carbon dioxide sequestration applications, the development of gas hydrates as media for storing and transporting gas, and the analysis of the effects of gas hydrates on climate change and flow assurance. The lack of sufficient studies in this field may be due to the challenging nature of experimental set-ups that measure such properties. Specifically, it is very difficult to synthesize pure gas hydrate samples with no residual water or gas and zero porosity, and no study has yet eliminated the significant effect of micropores. Additionally, even if the initial produced sample achieved high purity, ice may be produced later in the system during the experiment upon partial hydrate decomposition. With the significant improvement of computing power and facilities in the past few years, computational modelling has provided a reliable, complementary approach to gas hydrate characterization, which can sometimes be based solely on first-principles with simulations done at the electron level. This lack of reliable experimental results along with the high potential of computational modelling has been the main motivation of this thesis.

A detailed multiscale characterization of the mechanical, elastic and plastic, and key thermophysical properties of gas hydrates has been done using atomistic simulations. The work relied heavily on *ab initio* simulations at the nanoscale with no experimentally fitted parameters though a coarse-grained potential was also used at the microscale. The following sections highlight the main conclusions of every chapter in this thesis.

6.1.1 *Ab Initio* DFT Study of Structural and Mechanical Properties of Methane and Carbon Dioxide Hydrates

The full second-order elastic parameters for methane hydrate and carbon dioxide hydrate was determined using DFT simulations. Results for different exchange-correlation functionals and different isothermal equations of state were carefully compared and evaluated. Although both hydrates are sI formers and exhibited high elastic isotropy, they were found to differ significantly in their shear moduli which should be further investigated and considered in carbon dioxide sequestration applications. The agreement of the results with previous theoretical and experimental results for methane hydrates is generally good. DFT as implemented in SIESTA was found to be a useful approach within our selected basis set for modelling the elastic properties of hydrates using first-principles if proper functionals and simulation parameters are selected.

6.1.2 Ideal Strength of Methane Hydrate and Ice I_h from First-principles

The ideal strength of methane hydrate was determined using first-principles calculations. Uniaxial, triaxial, and shear deformation modes have been performed. Methane hydrate exhibited elastic isotropy in terms of its uniaxial strength, and it reflected brittle behavior in terms of its much higher strength under uniaxial and triaxial compression compared to tension. Over a wide pressure range, its bulk modulus varied linearly with pressure which is important when developing or using equations of state for these materials. The hydrate also seems to have no dominant slip systems which can be traced back to its radial bond arrangement.

As for ice I_h, its ideal uniaxial strength under tension and compression was determined using first-principles calculations. An early model of ice, the Bernal-Fowler lattice, yielded second-order elastic moduli which agreed very well with experimental data. Unlike the polycrystalline forms of hydrates and ice I_h in which the hydrate is much stronger than ice, perfect ice crystals were found to be more than 1.5 times stronger than perfect hydrate crystals which is important in crack analysis. The ice lattice was able to achieve a higher strength by deviating from the perfect tetrahedral arrangement of water molecules. However, at the ideal uniaxial tensile strength, both the hydrate and ice reached the same critical value of the hydrogen bond length. Finally, the ice was found to maintain its transverse isotropy throughout the uniaxial deformation, but the hydrate lost this isotropy as the ideal compressive strength was approached since its cages deformed non-uniformly.

6.1.3 *Ab Initio* Modelling of Methane Hydrate Thermophysical Properties

A wide range of thermophysical properties have been determined for methane hydrate using *ab initio* simulations. Specifically, second-order elastic constants, heat capacity, compressibility, and thermal expansion coefficients have been calculated over a wide range of conditions. The structures were ensured to be stable using the mean square displacement and radial distribution function measures.

Molecular statics were used to determine the pressure dependence of the second-order elastic constants. The bulk modulus was found to vary linearly with pressure up to 1 GPa, and the hydrate was found to be elastically isotropic. Multi-body interactions were found to play an important role in hydrates and should be accounted for in classical force fields.

Molecular dynamics were used to calculate the other properties. In general, most results agree well with experimental values and other theoretical calculations except for the thermal expansion coefficient. Up to 100 MPa, the water-water interactions were found to dominantly influence compressibility. Also, the thermal expansion coefficient was found significantly lower than literature values and lower than ice I_h values which can be related to the lower rigidity of the hydrate compared to ice, but it still needs further confirmation with more simulations and experimental values. The heat capacity, however, was much higher than that of ice.

Under all conditions the hydrate lattice was stable and exhibited the expected mean square displacement behaviour and radial distribution functions. The mean square displacement was found almost an order of magnitude higher than that of ice which helps explain the higher heat capacity of hydrate compared to ice. Also, the mean square displacement provided a very good rough estimate of the elastic modulus of hydrates. Finally, the radial distribution functions correctly reflected the cage structure of hydrates with the correct radius, coordination numbers, and hydrogen and covalent bonding behavior.

6.1.4 Core Structure and Peierls Stress of Linear Defects in Methane Hydrate

The core structure and Peierls stress for edge and screw dislocations have been determined as a function of methane composition and pressure for the $[100](010)$ slip system in methane hydrate. Both dislocations exhibited wide spreading and dissociation at different stresses during deformation. While the edge dislocation had much higher mobility compared to the screw dislocation as reflected in its Peierls stress, it also displayed much stronger dependence on methane composition. This may be due to the compressive stresses involved in edge dislocations which allow the effect of cage occupancy to be more evident than in screw dislocations with pure shear stresses. The Peierls-Nabarro model greatly underestimated the Peierls stress for the screw dislocation since it does not properly account for the discrete and evolving nature of the core structure. Also, the edge dislocation had a much stronger dependence on hydrostatic pressure which may be due to the asymmetry of its partial dislocations.

6.2 Contributions to Original Knowledge

6.2.1 Material Characterization

- The shear modulus of carbon dioxide hydrate was found to be significantly lower than that of methane hydrate, but both exhibited high elastic isotropy.
- Methane hydrate exhibited brittle behavior as reflected in its ideal hydrostatic strength and was found to have no dominant slip system as reflected in its ideal shear strength.
- Comparison of the ideal strength of perfect ice and methane hydrate crystals displayed an opposite trend compared to the behavior of their polycrystalline forms which highlights the significant influence of defects.
- The perfect ice crystal was found to have a much less rigid internal structure which allowed it to achieve a higher strength compared to methane hydrate, but hydrogen bonding was found to be the primary determinant for stability in both structures at high tensile stresses.
- The guest gas molecules in methane hydrate were found to affect the crystal’s transverse isotropy at high compressive stresses.
- Multi-body interactions were found to be important in gas hydrates.
- Up to 100 MPa, the water-water interactions were found to dominantly influence compressibility.
- Linear defects in gas hydrates were found to exhibit very wide spreading and dissociation.
- Edge dislocations have much higher mobility than screw dislocations but were shown to have a much stronger dependence on gas composition and pressure.

6.2.2 Computational and Modelling Contribution

- DFT was found suitable for modelling many mechanical and thermal properties of gas hydrates which have an extensive hydrogen bonding network.
- DFT has been applied for the first time to study such an extensive array of physical and thermal properties of gas hydrates without using any experimentally-fitted parameters.
- The revPBE functional in DFT was found to give reasonable results for many physical and structural properties of gas hydrates and ice.
- The simple Murnaghan equation of state was found to sufficiently describe gas hydrates.
- The mean square displacement and radial distribution functions provided very good measures of structural stability and the elastic modulus for gas hydrates.
- A coarse-grained potential appears to efficiently describe dislocations for gas hydrates and provides a case for comparison with other potentials.
- The dislocation characterization that was done provides the starting base for future work on dynamic dislocation flow models of gas hydrates which, so far, have not yet been properly developed.

6.3 Recommendations for Future Work

While this thesis models elastic and plastic deformation of individual gas hydrate crystals and characterizes key thermophysical properties at different scales, there is still so much to be done in this field as briefly summarized below.

- At the nanoscale, *ab initio* simulations are needed to quantify the temperature dependence of the second-order elastic constants and thermal conductivity. The only challenge would be the high computational demand and time-consuming nature of such a calculation.
- At the microscale, other kinds of defects, such as point or mixed defects, require modelling, and different force fields should be compared.
- At the macroscale, the interactions at grain boundaries and the effects of micropores need detailed analysis to minimize the gap between experimental and theoretical results.

7 Bibliography

1. C. Giavarini and K. Hester, *Gas Hydrates: Immense Energy Potential and Environmental Challenges*, Springer, London, 2011.
2. K. A. Kvenvolden, *Rev. Geophys.*, 1993, **31**, 173–187.
3. S. -M. Lu, *Renew. Sustainable Energy Rev.*, 2015, **41**, 884–900.
4. J. C. Stevens, J. J. Howard, B. A. Baldwin, G. Ersland, J. Husebo and A. Graue, *Experimental Hydrate Formation and Gas Production Scenarios Based on* CO_2 *Sequestration*, Proceedings of the 6th International Conference on Gas Hydrates, Vancouver, B. C., Canada, 2008.
5. Y. Park, D. -Y. Kim, J. -W. Lee, D. –G. Huh, K. –P. Park, J. Lee and H. Lee, *Proc. Natl. Acad. Sci. U.S.A*, 2006, **103**, 12690–12694.
6. E. D. Sloan, *Nature*, 2003, **426**, 353–359.
7. C. A. Koh, E. D. Sloan and A. K. Sum, in *Fundamentals of Materials for Energy and Environmental Sustainability*, ed. D. S. Gingley and D. Cahen, Cambridge University Press, New York, 2012, 12, 137–146.
8. T. Yuan, G. D. Spence, R. D. Hyndman, T. A. Minshull and S. C. Singh, *J. Geophys. Res.*, 1999, **104**, 1179–1191.
9. W. B. Durham, S. H. Kirby, L. A. Stern and W. Zhang, *J. Geophys. Res.*, 2003, **108**, 2182.
10. W. F. Waite, L. A. Stern, S. H. Kirby, W. J. Winters and D. H. Mason, *Geophys. J. Int.*, 2007, **169**, 767–774.
11. F. Ning, Y. Yu, S. Kjelstrup, T. J. H. Vlugt and K. Glavatskiy, *Energy Environ. Sci.*, 2012, **5**, 6779–6795.

12. E. D. Sloan and C. A. Koh, *Clathrate Hydrates of Natural Gases*, CRC Press, Boca Raton, FL, USA, 2008.

13. G. Schaftenaar and J. H. Noordik, *J. Comput. –Aided Mol. Design*, 2000, **14**, 123–134.

14. W. L. Mao, *Science*, 2002, **297**, 2247–2249.

15. N. H. Fletcher, *The Chemical Physics of Ice*, Cambridge U.P., London, 1970.

16. L. C. Jacobson, W. Hujo and V. Molinero, *J. Am. Chem. Soc.*, 2010, **132**, 11806–11811.

17. J. S. Tse, V. P. Shpakov, V. R. Belosludov, F. Trouw, Y. P. Handa and W. Press, *Europhys. Lett.*, 2001, **54**, 354–360.

18. H. Shimizu, T. Kumazaki, T. Kume and S. Sasaki, *Phys. Rev. B*, 2002, **65**, 212102.

19. J.S. Loveday, R. J. Nelmes, M. Guthrie, S. A. Belmonte, D. R. Allan, D. D. Klug, J. S. Tse and Y. P. Handa, *Nature*, 2001, **410**, 661–663.

20. H. Hirai, T. Kondo, M. Hasegawa, T. Yagi, Y. Yamamoto, T. Komai, K. Nagashima, M. Sakashita, H. Fujihisa and K. Aoki, *J. Phys. B*, 2000, **104**, 1429–1433.

21. W. Durham, L. Stern, S. Kirby and S. Circone, *Rheological Comparisons and Structural Imaging of sI and sII Endmember Gas Hydrates and Hydrate/Sediment Aggregates.* Proceedings of the 5th International Conference on Gas Hydrates, Trondheim, Norway, 2005.

22. W. B. Durham, L. A. Stern and S. H. Kirby, *Can. J. Phys.*, 2003, **81**, 373–380.

23. M. Choukroun, S. W. Kieffer, X. Lu and G. Tobie, in *The Science of Solar System Ices*, ed. M. S. Gudipati and J. C. –Rogez, Springer, New York, 2013, 12, 409–454.

24. M. Montagnat and P. Duval, *C. R. Physique*, 2004, **5**, 699–708.

25. F. Louchet, *C. R. Physique*, 2004, **5**, 687–698.

26. E. Tombari, S. Presto, G. Salvetti and G. P. Johari, *J. Chem. Phys.*, 2006, **124**, 154507.

27. J. S. Tse and W. R. McKinnon, *J. Phys. Chem.*, 1987, **91**, 4188–4193.

28. H. Tanaka, Y. Tamai and K. Koga, *J. Phys. Chem. B*, 1997, **101**, 6560–6565.

29. J. S. Tse, B. M. Powell, V. F. Sears and Y. P. Handa, *Chem. Phys. Lett.*, 1993, **215**, 383–387.

30. V. P. Shpakov, J. S. Tse, C. A. Tulk, B. Kvamme and V. R. Belosludov, *Chem. Phys. Lett.*, 1998, **282**, 107–114.

31. K. C. Hester, Z. Huo, A. L. Ballard, C. A. Koh, K. T. Miller and E. D. Sloan, *J. Phys. Chem. B*, 2007, **111**, 8830–8835.

32. M. Marchi and R. D. Mountain, *J. Chem. Phys.*, 1987, **86**, 6454–6455.

33. A. Klapproth, E. Goreshnik, D. Staykova, H. Klein and W. F. Kuhs, *Can. J. Phys.*, 2003, **81**, 503–518.

34. M. B. Helgerud, W. F. Waite, S. H. Kirby and A. Nur, *J. Geophys. Res.*, 2009, **114**, B02212.

35. F. L. Ning, K. Glavatskiy, Z. Ji, S. Kjelstrup and T. J. H. Vlugt, *Phys. Chem. Chem. Phys.*, 2015, **17**, 2869–2883.

36. H. Huo, Y. Liu, Z. Zheng, J. Zhao, C. Jin and T. Lv, *J. Renew. Sust. Energ.*, 2011, **3**, 063110.

37. C. R. Miranda and T. Matsuoka, *First-principles Study on Mechanical Properties of CH_4 Hydrate*, Proceedings of the 6th International Conference on Gas Hydrates, Vancouver, B. C., Canada, 2008.

38. G. Grimvall, *Thermophysical Properties of Materials*, Elsevier, Amsterdam, Netherlands, 1999.

39. G. V. Sin'ko and N. A. Smirnov, *J. Phys.: Condens. Matter,* 2002, **14**, 6989–7005.

40. M. Born, *J. Chem. Phys.*, 1939, **7**, 591–603.

41. T. E. Fischer, *Materials Science for Engineering Students*, Elsevier/Academic Press, Amsterdam, 2009.

42. J. Weertman, J. R. Weertman, *Elementary Dislocation Theory*, Oxford University Press, New York, 1992.

43. R. Peierls, *Proc. Phys. Soc.*, 1940, **52**, 34–37.

44. F. R. N. Nabarro, *Proc. Phys. Soc.*, 1947, **59**, 256.

45. J. P. Hirth, J. Lothe, *Theory of Dislocations*, Wiley, New York, 1982.

46. G. Schoeck, *Acta Mater.*, 1997, **45**, 2597–2605.

47. G. Schoeck, *Mater. Sci. Eng. A.*, 2005, **400**, 7–17.

48. D. S. Sholl and J. A. Steckel, *Density Functional Theory: A Practical Introduction*, Wiley, Hoboken, NJ, 2009.

49. J. G. Lee, *Computational Materials Science: An Introduction*, Taylor & Francis, Boca Raton, FL, 2011.

50. R. L. Rowley, *Statistical Mechanics for Thermophysical Property Calculations*, Prentice Hall, Englewood Cliffs, NJ, 1994.

51. D. H. J. Marx, *Ab Initio Molecular Dynamics Basic Theory and Advanced Methods*, Cambridge University Press, Leiden, 2009.
52. K. A. Kvenvolden, *Proc. Natl. Acad. Sci.*, 1999, **96**, 3420–3426.
53. E. D. Sloan, *Energ. Fuels*, 1998, **12**, 191–196.
54. H. Jiang and K. D. Jordan, *J. Phys. Chem. C*, 2009, **114**, 5555–5564.
55. C. Gutt, B. Asmussen, W. Press, M. R. Johnson, Y. P. Handa and J. S. Tse, *J. Chem. Phys.*, 2000, **113**, 4713–4721.
56. J. Zhao, J. M. Winey and Y. M. Gupta, *Phys. Rev. B*, 2007, **75**, 094105.
57. T. H. K. Barron and M. L. Klein, *Proc. Phys. Soc.*, 1965, **85**, 523–532.
58. M. J. Mehl, J. E. Osburn, D. A. Papaconstantopoulos and B. M. Klein, *Phys. Rev. B*, 1990, **41**, 10311–10323.
59. S. Q. Wang and H. Q. Ye, *Phys. Status Solidi B*, 2003, **240**, 45–54.
60. J. M. Soler, E. Artacho, J. D. Gale, A. Garcia, J. Junquera, P. Ordejon and D. Sanchez-Portal, *J. Phys. Condens. Matter*, 2002, **14**, 2745–2779.
61. G. Román-Pérez, M. Moaied, J. M. Soler and F. Yndurain, *Phys. Rev. Lett.*, 2010, **105**, 145901.
62. N. J. English and J. S. Tse, *J. Phys. Chem. A*, 2011, **115**, 6226–6232.
63. I. Ortega, A. Määttänen, T. Kurté, H. Vehkamäki, *Comput. Theor. Chem.*, 2011, **965**, 353–358.
64. SIESTA team, GGA Pseudopotential Database. See http://departments.icmab.es/leem/siesta/Databases/index.html.
65. ATOM, a program for DFT calculations in atoms and pseudopotential generation, distributed as part of the SIESTA software package. See http://www.icmab.es/siesta/atom.
66. M. Dion, H. Rydberg, E. Schröder, D. C. Langreth and B. I. Lundqvist, *Phys. Rev. Lett.*, 2004, **92**, 246401.
67. S. Grimme, *WIREs Comput. Mol. Sci.*, 2011, **1**, 211–228.
68. S. Grimme, J. Antony, S. Ehrlich and H. Krieg, *J. Chem. Phys.*, 2010, **132**, 154104.
69. F. D. Stacey, B. J. Brennan and R. D. Irvine, *Geophys. Surv.*, 1981, **4**, 189–232.
70. R. E. Cohen, O. Gülseren and R. J. Hemley, *Am. Mineral.*, 2000, **85**, 338–344.
71. S. Yoo, X. Zeng and S. Xantheas, *J. Chem. Phys.*, 2009, **130**, 221102.

72. J. Kang, E. –C. Lee and K. J. Chang, *Phys. Rev. B*, 2003, **68**, 054106.

73. K. A. Udachin, C. I. Ratcliffe and J. A. Ripmeester, *J. Phys. Chem. B*, 2001, **105**, 4200–4204.

74. A. Kelly, *Strong Solids,* Clarendon Press, Oxford, 1973.

75. D. Roundy and M. L. Cohen, *Phys. Rev. B: Condens. Matter Mater. Phys.*, 2001, **64***,* 212103.

76. U. Umeno, Y. Shiihara and N. Yoshikawa, *J. Phys.: Condens. Matter*, 2011, **23**, 385401.

77. M. Cerny, P. Sandera and J. Pokluda, *Czech. J. Phys.*, 1999, **49***,* 1495–1501.

78. J. D. Bernal and R. H. Fowler, *J. Chem. Phys.*, 1933, **1**, 515–548.

79. J.A. Hayward and J. R. Reimers, *J. Chem. Phys.*, 1997, **106**, 1518–1529.

80. P. G. Owston, *Adv. Phys.*, 1958, **7**, 171–188.

81. V. F. Petrenko and R. W. Whitworth, *Physics of Ice,* Oxford University Press, Oxford, 2002.

82. D. R. Hamann, *Phys. Rev. B: Condens. Matter Mater. Phys.*, 1997, **55***,* R10157.

83. D. Prendergast, J. C. Grossman and G. Galli, *J. Chem. Phys.*, 2005, **123**, 014501.

84. Z. M. Jendi, A. D. Rey and P. Servio, *Mol. Simul.*, 2015, **41**, 572–579.

85. S. R. Bahn and K. W. Jacobsen, *Comput. Sci. Eng.*, 2002, **4**, 56–66.

86. M. Born and K. Huang, *Dynamical Theory of Crystal Lattices,* Clarendon Press, Oxford, 1956.

87. T. S. Yun, J. C. Santamarina and C. Ruppel, *J. Geophys. Res.*, 2007, **112**, B04106.

88. X. Blase, P. Gillet, A. S. Miguel and P. Melinon, *Phys. Rev. Lett.*, 2004, **92**, 215505.

89. L. Fast, J. M. Wills, B. Johansson and O. Eriksson, *Phys. Rev. B: Condens. Matter Mate*r. Phys., 1995, **51**, 17431–17438.

90. R. E. Gagnon, H. Kiefte, M. J. Clouter and E. Whalley, *J. Chem. Phys.*, 1988, **89**, 4522–4528.

91. P. H. Gammon, H. Kiefte and M. J. Clouter, *J. Phys. Chem.*, 1983, **87**, 4025–4029.

92. R. E. Green and L. Mackinnon, *J. Acoust. Soc. Am.* 1956, **28**, 1292.

93. J. S. Tse, *J. Chem. Phys.,* 1992, **96**, 5482–5487.

94. Y. L. Trickett, I. Baker, P. M. S. Pradhan, *J. Glaciol.*, 2000, **46**, 41–44.

95. G. A. Jeffrey, *An Introduction to Hydrogen Bonding,* Oxford University Press, New York, 1997.

96. S. V. Goryainov, *Phys. B.*, 2012, **407**, 4233–4237.

97. K. Robinson, G. V. Gibbs, P. H. Ribbe, *Science*, 1971, **172**, 567–570.

98. C. W. Kammeyer and D. R. Whitman, *J. Chem. Phys.*, 1972, **56**, 4419–4421.

99. J. S. Loveday, R. J. Nelmes, M. Guthrie, D. D. Klug, and J. S. Tse, *Phys. Rev. Lett.*, 2001, **87**, 215501.

100. H. Wang and M. Li, *J. Phys.: Condens. Matter,* 2010, **22**, 295405.

101. J. H. Cha and Y. Seol, *ACS Sustainable Chem. Eng.*, 2013, **1**, 1218–1224.

102. C. A. Koh, E. D. Sloan, A. K. Sum and D. T. Wu, *Annu. Rev. Chem. Biomol. Eng.*, 2011, **2**, 237–257.

103. M. A. White and M. T. MacLean, *J. Phys. Chem.*, 1985, **89**, 1380–1383.

104. W. F. Waite, M. B. Helgerud, A. Nur, J. C. Pinkston, L. A. Stern, S. H. Kirby and W. B. Durham, *Ann. N. Y. Acad. Sci.*, 2000, **912**, 1003–1010.

105. H. Hirai, Y. Uchihara, H. Fujihisa, M. Sakashita, E. Katoh, K. Aoki, K. Nagashima, Y. Yamamoto and T. Yagi, *J. Chem. Phys.*, 2001, **115**, 7066–7070.

106. S. Takeya, T. Uchida, Y. Kamata, J. Nagao, M. Kida, H. Minami, H. Sakagami, A. Hachikubo, N. Takahashi, H. Shoji, O. Khlystov, M. Grachev and V. Soloviev, *Angew. Chem. Int. Ed.*, 2005, **44**, 6928–6931.

107. S. Takeya, M. Kida, H. Minami, H. Sakagami, A. Hachikubo, N. Takahashi, H. Shoji, V. Soloviev, K. Wallmann N. Biebow, A. Obzhirov, A. Salomatn and J. Poort, *Chem. Eng. Sci.*, 2006, **61**, 2670–2674.

108. A. G. Ogienko, A. V. Kurnosov, A. Y. Manakov, E. G. Larionov, A. I. Ancharov, M. A. Sheromov and A. N. Nesterov, *J. Phys. Chem. B*, 2006, **110**, 2840–2846.

109. Y. P. Handa, *J. Chem. Thermodynamics,* 1986, **18**, 915–921.

110. R. M. Rueff, E. D. Sloan and V. F. Yesavage, *AIChE J.*, 1988, **34**, 1468–1476.

111. R. Nakagawa, A. Hachikubo and H. Shoji, *Dissociation and Specific Heats of Gas Hydrates Under Submarine and Sublacustrine Environments*, Proceedings of the 6th International Conference on Gas Hydrates, Vacouver, B. C., Canada, 2008.

112. Z. M. Jendi, P. Servio, A. D. Rey, *Cryst. Growth Des.*, 2015, DOI: 10.1021/acs.cgd.5b00829.

113. S. Nosé, *J. Chem. Phys.*, 1984, **81**, 511–519.

114. M. Grimsditch, P. Loubeyre and A. Polian, *Phys. Rev. B*, 1986, **33**, 7192–7200.

115. V. V. Brazhkin and A. G. Lyapin, *Phys. Rev. Lett.*, 1997, **78**, 2493.

116. R. Bukowski, K. Szalewicz, G. C. Groenenboom and A. Avoird, *Science*, 2007, **315**, 1249–1252.

117. C. Caleman, P. J. V. Maaren, M. Hong, J. S. Hub, L. T. Costa and D. V. D. Spoel, *J. Chem. Theory Comput.*, 2012, **8**, 61–74.

118. M. W. Mahoney and W. L. Jorgensen, *J. Chem. Phys.*, 2000, **112**, 8910–8922.

119. R. Gagnon, H. Kiefte, M. Clouter and E. Whalley, *J. Phys. Colloq.*, 1987, **48**, 23–28.

120. G. H. Shaw, *J. Chem. Phys.*, 1986, **84**, 5862–5868.

121. M. Krafcik and E. S. Velasco, *Am. J. Phys.*, 2014, **82**, 301–305.

122. E. G. Noya, C. Menduina, J. L. Aragones and C. Vega, *J. Phys. Chem. C*, 2007, **111**, 15877–15888.

123. R. Feistel and W. Wagner, *J. Phys. Chem. Ref. Data*, 2006, **35**, 1021–1047.

124. A. K. Tyagi and S. N. Achary, in *Thermodynamic Propeties of Solids: Experiment and Modeling*, ed. S. L. Chaplot, R. Mittal and N. Choudhury, Wiley-VCH, Wenheim, 2010, 6, 197–267.

125. O. Haida, T. Matsuo, H. Suga and S. Seki, *J. Chem. Thermodynamics*, 1974, **6**, 815–825.

126. B. Fegley and R. Osborne, *Practical Chemical Thermodynamics for Geoscientists*, Academic Press, Waltham, MA, 2013.

127. P. M. Rodger, *J. Phys. Chem.*, 1990, **94**, 6080–6089.

128. P. M. Chaikin. C. Lubensky, *Principles of Condensed Matter Physics*, Cambridge University Press, Cambridge, 1995.

129. W. F. Kuha and M. S. Lehmann, *J. Phys. Chem.*, 1983, **87**, 4312–4313.

130. A. Goto, T. Hondoh and S. Mae, *J. Chem. Phys.*, 1990, **93**, 1412–1417.

131. J. S. Tse and M. L. Klein, *J. Phys. Chem.*, 1983, **87**, 4198–4203.

132. A. A. Chialvo, E. Yezdimer, T. Driesner, P. T. Cummings and J. M. Simonson, *Chem. Phys.*, 2000, **258**, 109–120.

133. A. A. Chialvo, M. Houssa and P. T. Cummings, *J. Phys. Chem. B*, 2002, **106**, 442–451.

134. V. V. Bulatov and W. Cai, *Computer Simulations of Dislocations*, Oxford University Press, Oxford, 2006.

135. S. Plimpton, *J. Comp. Phys.*, 1995, **117**, 1–19, http://lammps.sandia.gov.

136. L. C. Jacobson and V. Molinero, *J. Phys. Chem. B*, 2010, **114**, 7302–7311.

137. L. Jacobson, W. Hujo and V. Molinero, *J. Phys. Chem. B*, 2010, **114**, 13796–13807.

138. B. C. Knott, V. Molinero, M. F. Doherty and B. Peters, *J. Am. Chem. Soc.*, 2012, **134**, 19544–19547.

139. Z. M. Jendi, P. Servio and A. D. Rey, *Phys. Chem. Chem. Phys.*, 2016, DOI: 10.1039/C5CP06530E.

140. Y. L. Page and P. Saxe, *Phys. Rev. B*, 2002, **65**, 104104.

141. P. Hirel, A. Kraych, P. Carrez and P. Cordier, *Acta Mater.,* 2014, **79**, 117–125.

142. E. F. Petterson, T. D. Goddard, C. C. Huang, G. S. Couch, D. M. Greenblatt, E. C. Meng and T. E. Ferrin, *J. Comput. Chemi.*, 2004, **25**, 1605–1612.

143. T. Hondoh, H. Iwamatsu and S. Mae, *Philo. Mag. A*, 1990, **62**, 89–102.